

University of Nevada, Reno

SOIL HETEROGENEITY IN ARID SHRUBLANDS: BIOTIC AND ABIOTIC PROCESSES

A dissertation submitted in partial fulfillment of the
requirements for the degree of Doctor of Philosophy in
Hydrogeology

By

Todd G. Caldwell

Dr. Michael H. Young/Dissertation Advisor

December 2011



THE GRADUATE SCHOOL

We recommend that the dissertation
prepared under our supervision by

TODD G. CALDWELL

entitled

**Soil Heterogeneity in Arid Shrublands:
Biotic and Abiotic Processes**

be accepted in partial fulfillment of the
requirements for the degree of

DOCTOR OF PHILOSOPHY

Michael H. Young, Advisor

Markus Berli, Committee Member

Eric V. McDonald, Committee Member

Rina A. Schumer, Committee Member

Brian J. Andraski, Graduate School Representative

Marsha H. Read, Ph. D., Dean, Graduate School

December, 2011

© by Todd G. Caldwell 2011

All Rights Reserved

ABSTRACT

This dissertation investigates the evolution of soil heterogeneity on arid alluvial fans. Soil formation begins when depositional or erosional processes cease and a geomorphic surface becomes stable. The transformation of sediment to soil (pedogenesis) affects a multitude of hydrologic processes operating across a range of spatial and temporal scales. At the pore scale (μm – mm), soil development results in the formation of structure and secondary porosity. At the field scale, vegetation patches and open soil (or interspace) affect infiltration, partitioning of evapotranspiration, and ultimately vegetation performance and community structure. This feedback between vegetation and soil development is not well-defined in either time or space, and thus predicting their connection to ecosystem production or change is difficult. Ultimately, understanding how small-scale variability impacts larger scale processes is critical to examining whole ecosystem processes. The biotic and abiotic processes that shape arid landscapes operate at different spatial and temporal scales but ultimately control soil moisture variability and ecosystem patterns and processes. This dissertation attempts to expand the canopy interspace binary model of alluvial fans by (1) determining the spatial structure of hydraulic properties from canopy to interspace microsites, (2) quantifying, scaling and defining its spatial extent, (3) investigating the bio-abiotic factors that control the spatiotemporal heterogeneity of arid alluvial soils, and (4) implementing inverse modeling and field characterization to parameterize the vadose properties of these arid soil systems. We use high-spatial resolution measurements of unsaturated hydraulic conductivity, non-dimensional spatial correlation, numerical modeling and multiobjective

parameter optimization to address the role of bio-abiotic processes affecting both the spatial and temporal variability of soil moisture in arid shrublands.

Our results support the biotic feedback between soil and hydrologic processes. On young, weakly structured soils with high overall conductivity, this biofeedback may act to retain moisture and not simply increase saturated conductivity underneath vegetation. Spatially, we found a gradient in hydraulic and physical soil properties that extended 1.4 times the canopy radius. Through the use of a chronosequence, much of the soil heterogeneity could be explained spatially but its origin was a coupling of biotic and abiotic processes. Hydraulic properties were weakly correlated in space but 75% of the variance could be attributed to sand content, soil structure grade, mean-particle diameter, and organic matter. Lastly, multiobjective parameter optimization using the AMALGAM algorithm found the effective parameters of the near-surface vadose zone to be highly sensitive to factors often ignored in more mesic applications. In particular, parameters associated with the dry-end of the retention curve were well-defined while saturated conductivity and air-entry lost physical meaning or certainty. The coupled use of water content and potential data as minimization criteria through inverse modeling yielded more realistic parameters than either set alone with no single set of parameters being capable to minimizing both data sets.

Dedication

To my mother, who supported all of my academic pursuits – the good and the bad

To my wife and father, whose love and devotion encouraged me

To my daughter, who is and will always be my motivation

Acknowledgments

I am grateful to my co-advisor Eric McDonald, who not only brought me back to Reno, but also inspired my interest in desert soils. His support and encouragement were critical to my accomplishments. I later met my advisor Michael Young in Eric's favorite field area, the Providence Mountains. At that point, I was a technician hoping to someday be a brewer. After a few field excursions, I was a researcher. Mike's guidance, knowledge, and friendship throughout the years instigated this dissertation. I would also like to thank my committee, Markus Berli, Rina Schumer, and Brian Andraski, for their patience, motivation, and time. Additionally, I would like to recognize Glendon Gee, Scott Tyler, Dale Johnson, and Wally Miller for introducing me to vadose zone hydrology and soils; Doug Boyle, Jirka Simunek, Eddy Wohling, and Jasper Vrugt for teaching me MATLAB, HYDRUS and various other numerical methods; my DRI colleagues Steve Bacon, Todd Mihevc, Tom Bullard, Sophie Baker, Roger Kreidberg, and Mark Sweeney for their friendship and picking up my slack around the office; and my hydro-friends Josh Romeis, Mike Mann, Ramon Naranjo, Rich Niswonger, Justin Huntington, and Darren Meadows for all the great discussions and grumblings.

Financial support for Chapter 2 came from the National Science Foundation (EPSCoR RING-TRUE III grant number EPS-447416). Chapter 3 was supported by the Army Research Office under Desert Terrain Forecasting (DAAD19-03-1-0159). The field work related to Chapter 4 was supported by Army's Integrated Training Area Management program, Ruth Sparks in particular, at Ft. Irwin. I would like to thank Russ Harmon at the Army Research Office for his additional support for the numerical work under Global Military Operating Environments (W911NF-08-1-0453).

Table of Contents

1	<i>GLOBAL INTRODUCTION</i>	1
2	<i>SPATIAL STRUCTURE OF HYDRAULIC PROPERTIES FROM CANOPY TO INTERSPACE IN THE MOJAVE DESERT</i>	3
2.1	Introduction	5
2.2	Materials and Methods	6
2.3	Results	9
2.3.1	Binary Results: Canopy verse Interspace Microsites	9
2.3.2	Spatial Gradient from Canopy to Interspace Microsites	10
2.3.3	Spatial Extent of the Measured Gradient	12
2.4	Discussion and Conclusions	12
2.5	Acknowledgments	14
2.6	References	15
2.7	Tables	18
2.8	Figures	20
3	<i>BIOTIC AND ABIOTIC CONTROLS ON SOIL HETEROGENEITY IN ARID SHRUBLANDS</i>	22
3.1	Introduction	25
3.2	Materials and Methods	28
3.3	Results	32
3.3.1	Canopy and Interspace Microsites	33
3.3.2	Spatial Dependency of Soil and Hydraulic Properties	35
3.3.3	Spatial Extent of the Measured Gradients	37
3.3.4	Biotic and Abiotic Factors Controlling the Evolution of K_s	37

3.4	Discussion and Conclusions.....	39
3.5	Tables	44
3.6	Figures.....	48
3.7	Acknowledgments.....	51
3.8	References	52
4	<i>INVERSE MODELING OF NEAR-SURFACE VADOSE ZONE PROPERTIES IN DESERT SOILS USING MULTIOBJECTIVE PARAMETER OPTIMIZATION</i>	56
4.1	Introduction	58
4.2	Materials and Methods.....	61
	4.2.1 Site Description and Field Characterization.....	61
	4.2.2 Observational Data from Microclimate Stations.....	62
	4.2.3 Meteorological Data and Potential Evapotranspiration	63
	4.2.4 Direct Measurements of Hydraulic Properties	64
	4.2.5 Indirect Estimates of Hydraulic Properties	65
4.3	Inverse Modeling and Multiobjective Parameter Optimization.....	66
	4.3.1 Regional Sensitivity Analysis	66
	4.3.2 Multiobjective Framework and Performance Criteria	67
	4.3.3 Parameter Optimization Algorithm.....	68
4.4	Results – Field Characterization	70
	4.4.1 Soil Characterization.....	70
	4.4.2 Direct Measurements of Hydraulic Properties	71
4.5	Results – Numerical Modeling.....	72
	4.5.1 Parameter Sensitivities in the Near-surface, Arid Vadose Zone.....	72

4.5.2	Multiobjective Parameter Optimization	73
4.5.3	Direct and Indirect Methods of Parameterization	77
4.6	Discussion and Conclusions.....	78
4.7	Tables	82
4.8	Figures	86
4.9	Acknowledgments	96
4.10	References	96
5	<i>GLOBAL CONCLUSIONS AND RECOMMENDATIONS</i>	101

List of Tables

Table 2-1. Means (\pm standard deviation) of binary (canopy vs. interspace) soil physical properties for both measured vegetation types: <i>L. tridentata</i> and <i>L. pallidum</i>	18
Table 2-2 Means (\pm standard deviation) of binary (canopy vs. interspace) hydraulic properties for both measured vegetation types: <i>L. tridentata</i> and <i>L. pallidum</i>	18
Table 2-3. Correlation coefficients between R_{norm} and measured parameters for <i>L. tridentata</i> and <i>L. pallidum</i> , combined and individually.....	19
Table 3-1. Mean (\pm one standard deviation) soil physical properties and 2-factor ANOVA results for microsite (BIN), geomorphic surface and combined.....	44
Table 3-2. Mean (\pm one standard deviation) hydraulic properties including the continuous and piece-wise $K(\psi)$ functions and 2-factor ANOVA results for microsite (BIN), geomorphic surface and combined	45
Table 3-3. Pearson correlation coefficients between soil physical characteristics to the normalized radial distance (R_{norm}) for all locations, distal ($R_{norm} > 1.5$) and proximal ($R_{norm} < 1.5$) locations for all surfaces and on each surface.....	46
Table 3-4. Spatial extent in normalized canopy radius of proximal ($R_{norm} < 1.5$) correlations with $p < 0.01$	46
Table 3-5. Pearson correlation coefficients between K_s and soil physical characteristics for all locations, distal ($R_{norm} > 1.5$) and proximal ($R_{norm} < 1.5$) locations for all surfaces and on each surface.....	47
Table 4-1. Summary of direct, indirect, and inverse methods used to obtain effective hydraulic parameters	82

Table 4-2. Parameter uncertainty bounds for hydraulic parameters in equations [2] and [3] used in both the regional sensitivity analysis and the global optimization algorithm	82
Table 4-3. Mean soil texture characterization for each horizon averaged from 4-5 soil trenches.	83
Table 4-4. Mean hydraulic properties from tension infiltrometer tests and their respective confidence intervals (<i>CI</i>) at 95%. These intervals also represent the <i>a priori</i> constrained parameter space for θ_s and K_s	83
Table 4-5. Root mean square error (<i>RMSE</i>) and mean bias error (<i>MBE</i>) between simulated and observed values of θ , ψ , and soil temperature (T) for the Pareto-extreme solutions for θ (ParEx $_{\theta}$), for ψ (ParEx $_{\psi}$) and the compromise solution for three degrees of increasing vertical heterogeneity (L_{1-3}). The AMALGAM code optimized $RMSE_{\theta}$ and $\log(RMSE_{\psi})$ and the minimal values are present in bold. 84	84
Table 4-6. Root mean square error (<i>RMSE</i>) and mean bias error (<i>MBE</i>) between simulated and observed values of θ , and ψ for the Pareto compromise solution using constrained parameter space and the two-layer (L_{2c}) scenario	85
Table 4-7. Root mean square error (<i>RMSE</i>) and mean bias error (<i>MBE</i>) between direct and indirect parameterization of simulated and observed values of θ and ψ	85

List of Figures

- Figure 2-1. Spatial correlation of soil physical properties from canopy to interspace for (a) organic matter, (b) bulk density, and (c) gravel ($>2000 \mu\text{m}$) 20
- Figure 2-2. Spatial correlation of hydraulic parameters from canopy to interspace for α_{exp} (a and b); K_s or $K(\psi)$ at 0 cm H₂O (c and d), and piece-wise functions of $K(\psi)$ at -1.5 cm (e and f); and $K(\psi) = -4.5$ cm (g and h) for *L. tridentata* and *L. pallidum*, respectively. 21
- Figure 3-1. Geomorphic soil map of the Providence Mountain study area, in southeastern California, located on the mixed plutonic (PM) sequence. Watershed boundaries are indicated by the dashed lines. Three other lithologies including limestone (LS), mixed volcanics (VX) and quartz monzonite (QM) are also identified. Adapted from McDonald et al. (2003)..... 48
- Figure 3-2. Box plots of [a] saturated hydraulic conductivity (K_s) and [b] the reciprocal of macroscopic capillary length (α) binned by interspace or mound microsite for all measurements and for each geomorphic surface from oldest (Qf3) to youngest (Qf7). The letters indicate significant ($p < 0.05$) groups from the post hoc (Sidak-Holms) t-tests. 49
- Figure 3-3. Hydraulic conductivity functions for soil water pressures from saturation (0 cm) to -10cm on [a] the oldest surface, Qf3, [b] the intermediate geomorphic surface, Qf5, and [c] the youngest surface, Qf7. Solid lines are the mean values and the corresponding dotted lines represent the 95% confidence intervals. 49
- Figure 3-4. Hydraulic conductivity at canopy ($R_{norm} < 1$) and interspace (IS) microsites on the old Qf3 [a-c], the intermediate Qf5 [d-f] and young surface Qf7 [g-i] at saturation ($\psi = 0$ cm) and under tension of -1.5 and -4.5 cm. The lines indicate spatial trends and are only weakly significant ($p < 0.1$) at IS microsites on the Qf3 [a] and Qf5 [b]. 50

- Figure 3-5. Predicted saturated conductivity (K_s) for all measurement locations using multiple linear regression and the independent variables soil structure grade, mean particle diameter, percent sand and organic matter. 51
- Figure 4-1. Observed water retention data from the 3-, 10, and 25-cm *in situ* soil sensors at [a] *LIZ*, [b] *JWH*, and [c] *BLK* field sites. The corresponding solid lines represent the data fitted to Eq. [3]. The near-saturated water content was constrained using field-measured $\theta(\psi = 0.005\text{m})$ following each tension infiltrometer (TI) test. 86
- Figure 4-2. The cumulative distribution function (CDF) of ranked parameters for a single-layer (0-100cm) regional sensitivity analysis at *JWH*. Each line represents 10% of the population grading from the ‘best’ (thick black line) to ‘worst’ (light gray) model performance for each criterion. Each column represents the criterion performance RMSE_θ (left) and RMSD_ψ (right) for each hydraulic parameter. ... 87
- Figure 4-3. Non-dominated, Pareto-optimal solutions (dark circles) and previous dominated solutions (gray circles) for the global optimization runs with [a] one-layer, L_1 ; [b] two-layer, L_2 , and [c] three-layer, L_3 soil profile. The Pareto extremes are denoted by blue squares and the compromise solution with a white cross. The normalized Pareto objective space represents the tradeoff between $g(\text{RMSE}_\theta)$ and $g(\text{RMSE}_\psi)$ 88
- Figure 4-4. Observed (circles) and simulated absolute heads (ψ) at [a] 0.03, [b] 0.10, [c] 0.25 and [d] 0.45 m depths for the AMALGAM single-layer, L_1 , optimization at *BLK*. Gray lines are all Pareto-optimal values, the hashed lines are Pareto-extremes, and the compromise solution is in blue. 89
- Figure 4-5. Observed (circles) and simulated water contents (θ) at [a] 0.03, [b] 0.10, [c] 0.25 and [d] 0.45 m depths for the AMALGAM single-layer, L_1 , optimization at *BLK*. Gray lines are all Pareto-optimal values, the hashed lines are Pareto-extremes, and the compromise solution is in blue. 90

- Figure 4-6. Observed (circles) and simulated water contents (θ) at [a] 0.03, [b] 0.10, [c] 0.25 and [d] 0.45 m depths for the AMALGAM double-layer, L_2 , optimization at *BLK*. Gray lines are all Pareto-optimal values, the hashed lines are Pareto-extremes, and the compromise solution is in blue. 91
- Figure 4-7. Cumulative distribution functions (CDF) of Pareto-optimal solutions for layers 1-3 from the L_3 scenario at *JWH*. 92
- Figure 4-8. Normalized Pareto optimal parameters for the [a] global and [b] constrained two-layer, L_2 scenario at *BLK*. Each gray line represents one Pareto-optimal solution. The black lines are Pareto-extremes and compromise solution is the solid blue line. The superscripts indicate the respective soil layer. 93
- Figure 4-9. Time series plot of soil moisture (θ) at *JWH* parameterized using direct measurements from tension infiltrometers (D_1), *in situ* water retention combined with infiltrometer $K(h)$ data in RETC (D_2), and three PTF results as outlined in Table 4-1. 94
- Figure 4-10. Time series plot of potential (ψ) at *JWH* parameterized using direct measurements from tension infiltrometers (D_1), *in situ* water retention combined with infiltrometer $K(h)$ data in RETC (D_2), and three PTF results outline in Table 4-1. 95

1 GLOBAL INTRODUCTION

The ecohydrology of arid environments is strongly coupled to available water (Noy-Meir, 1974; Eagleson, 1978; Rodriguez-Iturbe et al., 1999). Soils serve as the buffer between the atmosphere and vegetation, regulating water, energy and nutrient transfer that ultimately control primary production. Soil development in arid regions and the resulting morphology are functions of climate, biologic activity and, most importantly, time. Soil texture and structure are temporally variable, evolving in time and space and ultimately affecting soil hydrologic functioning (McDonald et al., 1996; Young et al., 2004; Scanlon et al., 2005; Meadows et al., 2008).

Recent investigations (Hammerlynk et al., 2002; Caldwell et al., 2006; Shafer et al., 2007; Stevenson et al., 2009) have further identified linkages between biotic and abiotic processes that affect arid ecosystem functions. However, the spatiotemporal variability between these ecologic, hydrologic and pedologic processes is not known affecting our ability to upscale or downscale the observed processes to other scales of interest: the bajada (large), the plot (medium), the patch (fine–medium), the point (fine) and the pore-scale (Seyfried and Wilcox, 1995). At the microsite (or patch) scale characterized by vegetation canopy or bare soil interspace, field investigations can yield patch- and point-scale information such as a water retention function for a specific sublocation. However, using these data in numerical simulations seldom returns reasonable fits to field scale observations of soil moisture (Wohling et al., 2008; Gribb et

al., 2009). The spatial variability of hydraulic properties at the field scale is extreme (Nielsen et al., 1973) and the scale of measurement often affects its outcome (Mallants et al., 1996), particularly in patchy landscapes (Wilcox et al., 2003). Ultimately, understanding effects of fine-scale (cm) variability effects on larger-scale (m–km) processes is the motivation of this dissertation.

We hypothesize that we can use this variability to explain the following. From an ecohydrological perspective, how do heterogeneous soil properties influence the soil-water balance of arid regions? From an experimental ecologist view, how vital is the spatial variability of hydraulic properties to ecosystem function? And how important is hydraulic property variability at the plot scale where the soil-water balance can ultimately be determined? These questions will be answered in a series of three papers, which will respectively focus on answering:

- (1) Does variability exist at the microsite level?
- (2) What bio-abiotic process control heterogeneity at the bajada scale?
- (3) How can we best model arid soil processes in the near-surface environment?

2 SPATIAL STRUCTURE OF HYDRAULIC PROPERTIES FROM CANOPY TO INTERSPACE IN THE MOJAVE DESERT

Todd G. Caldwell¹, Michael H. Young², Jianting Zhu², Eric V. McDonald¹

¹Division of Earth and Ecosystem Sciences, Desert Research Institute, 2215 Raggio
Parkway, Reno, NV 89512

²Division of Hydrologic Sciences, Desert Research Institute, 755 East Flamingo Road,
Las Vegas, NV 89119

Geophysical Research Letters, 35, L19406, doi:10.1029/2008GL035095, 2008

Abstract

Desert piedmonts are a mosaic of interspersed vegetation and bare soil, previously considered to be a binary system of canopy and interspace microsites. The spatial structure of soils and hydraulic properties in these microsites affects our ability to upscale or downscale observed processes. We determined variability and spatial correlation of hydraulic properties using high-resolution measurements of unsaturated hydraulic conductivity [$K(\psi)$] along linear transects radiating from canopies of perennial shrubs common to the Mojave Desert into bare soil interspaces. Hydraulic conductivity from $-6 < \psi < 0$ cm soil water pressures was lower under canopy. Spatial correlations to organic matter, particle-size, and $K(\psi)$ were observed to approximately 1.4 times canopy diameter, beyond which random processes dominated. Results illustrate that a predictable spatial structure in $K(\psi)$ exists between canopy and interspace microsites, and suggest that scaling from the plant to field plot could exploit this relationship.

Index Terms

Soils/pedology [1865], Eco-hydrology [1813], hydrologic scaling [1839], plant ecology [1851], soil moisture [1866]

2.1 Introduction

Ecohydrology of arid environments is strongly coupled to available water [Rodriguez-Iturbe, 2000]. Surface soil structure and texture affect the depth of water penetration [Scanlon *et al.*, 2005], and hence root distributions of perennial plants [Gile *et al.*, 1998], and the diversity and vigor of native vegetation [Hamerlynck *et al.*, 2002]. Recent investigations [Ravi *et al.*, 2007; Shafer *et al.*, 2007; Bedford and Small, 2008] have identified linkages among biotic and abiotic processes that may act at different scales. Uncertainty in spatial heterogeneity of these linkages, however, affects our ability to upscale or downscale observed processes to other scales of interest: the bajada (large), plot (medium), and point scale (fine).

At the microsite scale (canopy or interspace), field investigations can yield point-scale information on particle size distribution and soil hydraulic properties, but relatively few have shown spatial patterns at the meter scale. In one case, hydraulic conductivity increased 3–5 times under the canopy of an Australian *Maireana* [Dunkerley, 2000]. Titus *et al.* [2002] measured point-scale properties below and adjacent to shrubs. Sparse measurements were taken, however, and the data set does not directly lend itself to upscaling to Mojave Desert bajadas where perennial vegetation covers approximately 5 to 40% [Romney *et al.*, 1973] of the land area. Ultimately, understanding how small-scale variability (few cm) affects larger scale processes (decimeters to meters) is important to examining whole ecosystem processes at the field or basin scale.

To address this variability, we seek to answer the following questions: (1) does spatial structure exist from canopy to interspace microsites? And (2) is the structure predictable, quantifiable, and scalable?

2.2 Materials and Methods

Our study was conducted at the Mojave Global Change Facility (MGCF), located approximately 90 km northwest of Las Vegas, Nevada on the Nevada Test Site (36°49'N, 115°55'W). The MGCF is located on an alluvial fan complex derived from recent calcareous alluvium consisting primarily of soils (Entisols) with limited soil development and horizonation [Marion *et al.*, 2008].

Vegetation at the site is representative of both Mojave and Great Basin Deserts [Hansen *et al.*, 1999] consisting primarily of *Larrea tridentata* (creosotebush), *Lycium pallidum* (desert thorn), *Ambrosia dumosa* (white bursage), and *Ephedra nevadensis* (Mormon tea). For this study, we focused measurements on the dominant vegetation by percent cover: *L. tridentata* (LATR) and *L. pallidum* (LYPA). A total of six shrubs (three LATR and three LYPA) were chosen along the east-central boundary of the MGFC. Vegetation size was varied to cover a range of canopy diameters for LATR (45, 100, and 190 cm) and LYPA (40, 80, 120 cm).

We determined hydraulic properties using discrete measurements of unsaturated hydraulic conductivity [$K(\psi)$] along four transect radiating outward from each shrub to the interspace. Transects were 1.5–1.75 m long with measurements taken every 25 cm to avoid overlapping wetting fronts. Each transect originated as close as possible to the shrub center, generally within 10–20 cm. Measurements of $K(\psi)$ were simultaneously

conducted using a linear array of seven, independently-operated, modified mini-disk (4.5 cm diameter) tension infiltrometers ([MDTI] (Model S; Decagon Devices; Pullman, WA)—allowing precise control of the water supply head or potential (ψ) via a Mariotte column from near saturation (-0.1 cm) to -6 cm H₂O. MDTI modifications increased each reservoir capacity to 2000 mL and added differential pressure transducers to monitor cumulative outflow at five second intervals. Infiltration was conducted at three incremental soil water tensions ($\psi = -6, -3$ and -0.1 cm) until steady state (constant outflow per time) was reached, generally 30–45 minutes per tension step.

Following each MDTI test, a soil core (6.4 cm ID, 2.5 cm tall) was taken underneath each water-entry point. We measured cores for bulk density, organic matter by loss-on-ignition at 400°C [*Ben-Dor and Banin, 1989*], and particle size distribution by first mechanically sieving to 2, 1, and 0.5 mm fractions. The <0.5 mm fraction was analyzed by laser light diffraction (Micromeritics Saturn DigiSizer 5200; Norcross, GA; [*Gee and Or, 2002*]). Geometric mean particle diameter (*MPD*) and log standard deviation (σ) were calculated [*Shiozawa and Campbell, 1991*] from reassembled data.

We analyzed outflow data from each MDTI for steady-state unconfined infiltration from a circular source given by [*Wooding, 1968*]:

$$q(\psi) = \pi r^2 K(\psi) \left[1 + \frac{4\lambda_c}{\pi r} \right] \quad \text{[Equation 1]}$$

where $q(\psi)$ is the steady state infiltration (cm³ s⁻¹), r is the infiltrometer radius (cm), $K(\psi)$ is hydraulic conductivity at the applied tension (ψ), and λ_c is the macroscopic capillary length (cm). The relationship assumes an initially dry, homogeneous, anisotropic and

uniformly unsaturated soil. Wooding's analysis is based upon the unsaturated conductivity function, $K(\psi)$, defined by [Gardner, 1958]:

$$K(\psi) = K_s \exp(\alpha\psi) \quad \psi < 0 \quad \text{[Equation 2]}$$

where K_s has units of cm s^{-1} , and α has units of cm^{-1} . The scaling parameter, α , is the logarithmic derivative of the hydraulic conductivity function with respect to capillary forces and equal to $1/\lambda_c$. Using a tension infiltrometer through a range of pressures, solutions can be obtained using (1) nonlinear least-squares regression by minimizing the sum of squares residuals between observed and calculated $q(\psi)$ through iterative solutions [Logsdon and Jaynes, 1993], resulting in a continuous, exponential function containing K_s and α_{exp} ; and (2) as a piece-wise continuous function of $K(\psi)$ and $\alpha(\psi)$ for the midpoint between each supply head [Ankeny *et al.*, 1991]. In our case, a ψ of -6, -3, and -0.1 cm H₂O result in $K_{-4.5}$ and $K_{-1.5}$ and corresponding α values $\alpha_{-4.5}$ and $\alpha_{-1.5}$, respectively.

We spatially normalized all point measurements to a single radial distance (R_{norm}) relative to their respective vertical projection of the canopy radius by

$$R_{\text{norm}} = \frac{Z}{Z_{\text{canopy}}} \quad \text{[Equation 3]}$$

where measurements from canopy center to edge, Z_{canopy} (cm), are divided by position (Z) along the length of each transect. A point within the canopy will thus have an $R_{\text{norm}} < 1$ and a point beyond the canopy will have an $R_{\text{norm}} > 1$.

We performed statistical tests assuming both a binary population (canopy or interspace microsite) and a spatial R_{norm} linear regression approach. For the binary approach, a two-factor analysis of variance (ANOVA) was carried out between

vegetation and microsite. We also conducted a single factor ANOVA between transect direction around each plant. Finally, Spearman correlations were used to determine significant ($P < 0.05$) spatial correlation to R_{norm} . All statistical analyses were done in SigmaStat (v. 3.5; Systat Software, Inc.).

2.3 Results

2.3.1 Binary Results: Canopy versus Interspace Microsites

Binary soil properties binned according to canopies versus interspaces indicate a significant difference (ANOVA, $P < 0.05$) between microsites, with clay ($< 2 \mu\text{m}$) content the only noted exception (Table 2-1). Organic matter, sand (2000–50 μm), and silt (50–2 μm) were greater under canopies; gravel ($> 2000 \mu\text{m}$) and bulk density were greater at interspace microsites. Significant differences existed only for sand (2000–50 μm) between the canopy sites for the two different shrub types, which was slightly greater under LYPA than LATR. We found no significant differences between either shrub type or its respective interspace. These results confirmed that canopy and interspace microsites were statistically different and independent of vegetation type.

Binary hydraulic properties also indicate a significant difference (ANOVA, $P < 0.05$) between both microsites—independent of vegetation type (Table 2-2). We calculated hydraulic properties for both the continuous exponential $K(\psi)$ function resulting in K_s and α_{exp} , and a piece-wise linear $K(\psi)$ for each pair of applied ψ resulting in $K_{-1.5}$ and $\alpha_{-1.5}$, and $K_{-4.5}$ and $\alpha_{-4.5}$. All $K(\psi)$ values failed normality tests and were log-transformed prior to statistical testing. Both methods indicate that canopy $K(\psi)$ was significantly lower than interspace $K(\psi)$ by approximately two-fold. The α value [slope of

$K(\psi)$] was significantly greater under canopies; thus, differences between $K(\psi)$ under canopy and interspace microsities becomes amplified as ψ decreases (i.e. soils become drier).

Soils at the MGCF had relatively high conductivities at all locations. The geometric mean of K_s was 20.2 cm h^{-1} , with a minimum of 1.9 cm h^{-1} and a maximum of 68.8 cm h^{-1} . Thus, it is unlikely that saturated conditions will persist even under high intensity precipitation events. These results further emphasizing the significance of $K(\psi)$ over measurements of K_s .

2.3.2 Spatial Gradient from Canopy to Interspace Microsities

First, a single factor ANOVA found no significant difference between any soil or hydraulic properties and the cardinal direction emanating from the canopy. In some instances, eolian material was shown to preferentially deposit on the lee side of the shrub [Ravi *et al.*, 2007]; however, in our case, the sum of silt and clay was higher along the northern transect at $16.3 \pm 3.8\%$ and lower along the western ($14.4 \pm 2.5\%$) and southern ($14.4 \pm 2.4\%$) transects, but neither was significant at $P < 0.05$. Predominant wind directions are from the south-southwest, and a source area is located toward the south as well, which may explain the slight increase in fine material on the north side of the canopy. Second, when data were restricted to $R_{norm} < 1.5$, the silt component ($50\text{--}2 \mu\text{m}$) was significantly higher (14.0%) along north transects than south (12.0%) transects for both LATR and LYPA. However, hydraulic properties did not show any significant directional component. Thus, each point was transposed to a single radial component and normalized by its respective canopy radius [R_{norm} in Eq. 3]

The R_{norm} radial position allows data from any transect to be pooled and the effect of varying canopy size to be removed. We plotted measured soil physical properties including organic matter (Figure 2-1a), bulk density (Figure 2-1b), and gravel content (Figure 2-1c) against spatially scaled R_{norm} . For example, organic matter decreased from the inner canopy to the canopy edge ($0.2 < R_{norm} < 1$), beyond which ($R_{norm} > 1$) correlation was lower (Figure 2-1a). Limiting the correlation data set to locations where $R_{norm} < 1.5$, the maximum correlation coefficient was found ($r = -0.68$, $P < 0.001$; Table 2-3). Similarly, bulk density and gravel content increased linearly ($P < 0.001$) with distance to $R_{norm} < 1.5$, where maximum Spearman coefficients were found ($r = 0.73$ and 0.72 , respectively).

The measured hydraulic properties related to the exponential [Eq. (2)] and piecewise fits to cumulative outflow also exhibited a spatial gradient from canopy to interspace microsites (Table 2-3). The exponential α_{exp} declined ($P < 0.001$) for both *L. tridentata* (Figure 2-2a) and *L. pallidum* (Figure 2-2b) to a $R_{norm} = 1.5$, beyond which no correlation ($P < 0.05$) was found. Measured $K(\psi)$ was uncorrelated to $R_{norm} < 1.5$ (Table 2-3) either near saturation ($\psi = -0.1$ cm; Figures 2-2c and 2-2d) or at $\psi = -1.5$ cm (Figures 2-2e and 2-2f). Correlations were significant ($P < 0.01$), however, at $\psi = -4.5$ cm for LATR (Figure 2-2g) but not LYPA (Figure 2-2h). For $K_{-4.5}$, the correlation to R_{norm} increased to 0.34 ($P < 0.01$) for the combined LATR and LYPA data and increased further to 0.50 ($P < 0.01$) for data related only to LATR (Table 2-3). With the exception of K_s and $K_{-1.5}$, most hydraulic properties were found to have significant spatial correlations.

2.3.3 Spatial Extent of the Measured Gradient

Considering canopies and interspaces as binary sites, K_s was greater and α_{exp} was lower for interspace microsites. We observed higher spatial correlation for $K(\psi)$ with decreasing ψ ; correlation increased away from saturation. Maximum correlations for all parameters were obtained for $R_{norm} < 1.5$ (Table 2-3). The extent of this gradient with respect to R_{norm} could be useful for scaling soil properties based upon canopy projection from either aerial photography or even remote sensing.

We calculated spatial extent of the influence from vegetation by intersecting the means of the binary interspace ($R_{norm} > 1.5$) parameters (Tables 2-1 and 2-2) with values (respective slopes and intercepts) obtained from significant ($P < 0.001$) correlations between under canopy properties and $R_{norm} < 1.5$. For the combined data (both LATR and LYPA), we used nine parameters to calculate the extent of R_{norm} resulting in a mean (\pm standard deviation) distance of 1.41 ± 0.15 . Considering the parameters for each shrub separately, the radial extent was very similar to the combined result, or $R_{norm} = 1.34 \pm 0.17$ and 1.39 ± 0.14 for LATR and LYPA, respectively. Thus, the spatial structure radiating from the canopy exists to approximately 1.4 times canopy radius.

2.4 Discussion and Conclusions

Results of this study indicate that spatial structure exists at the meter scale and is highly correlated and scalable to shrub size. Although binary values between canopy and interspace microsites were significantly different, a predictable spatial structure exists between them. Results further show that under-canopy K_s in these weakly structured, young alluvial soils was less than in the interspace; as noted prior this soil lacks a desert

pavement. These results are contrary to others [Lyford and Qashu, 1969; Dunkerley, 2000; Bedford and Small, 2008] who found higher conductivity under-canopy K_s using ponded (positive soil water pressures) infiltration tests. The development of the hydraulically restrictive vesicular A horizon is paramount in the formation of a divergence between interspace and canopy soils.

Our results support the effect of biotic processes on—and from—soil and hydrologic processes. These biotic processes are not well defined in time or space in most locations, and thus predicting their connection to ecosystem production or change is difficult. Gradients in physical and hydraulic properties require establishment of the canopy and underlying mound, but the relative age of the shrub and associated soil can vary greatly. For example, grasslands of the Chihuahuan desert “rapidly” (i.e., in decades) converted to heterogeneous shrubland dominated by *L. tridentata* [Grover and Musick, 1990]; while biotic processes under canopies (i.e., faunal burrowing, bioturbation, root turnover) likely operated concurrently. Higher K_s and lower α in interspaces shown here would result in deeper flux which perhaps corresponds to greater root densities found in interspaces particularly at the MGCF [Wilcox *et al.*, 2004]. Roots of desert perennials, however, are more often concentrated under canopies [Jackson *et al.*, 1996], where infiltration depth is enhanced by vegetation.

By comparison, abiotic processes (e.g., dust accumulation, pedogenesis, desert pavement formation) vary over 10 to 100 *ka* timescales [McFadden *et al.*, 1986]. At other field sites, interspace K_s has been negatively correlated to geologic age of the alluvial deposit with younger, coarse-textured soils having higher K_s than significantly older, fine-grained desert pavements [Young *et al.*, 2004]. This pedologic evolution of desert

soils resulting primarily from dust accumulation and redistribution [Reheis *et al.*, 1995], further has been shown to affect vegetation structure by decreasing infiltration capacity resulting in smaller shrubs, decreased vegetation density, and negative impacts to shrubs [Hamerlynck *et al.*, 2002; McAuliffe *et al.*, 2007]. In these cases, abiotic processes exerted significant influence on ecosystem evolution.

Desert soils, whether young or old, have a geomorphic context which must be considered [Caldwell *et al.*, 2006]. Without this geomorphic context of the interspace soil, inferences of binary results on alluvial fans are difficult to interpret. Numerous studies have measured higher K_s underneath canopies, particularly under positive head or ponded conditions [Lyford and Qashu, 1969; Dunkerley, 2000; McAuliffe *et al.*, 2007; Bedford and Small, 2008; Nimmo *et al.*, 2009], following natural rainfall [Bhark and Small, 2003], and even with tension infiltrometers [Caldwell *et al.*, 2006; Shafer *et al.*, 2007]. For younger alluvial soils, however, $K(\psi)$ may be similar between microsites [Caldwell *et al.*, 2006] or even lower for under canopy sites on young eolian deposits where interspace soils were dominated by sandy soils [Ravi *et al.*, 2007]. Considering that desert landforms consist of heterogeneous alluvial deposits of interspersed soils of varying ages, the dichotomy between canopy and interspace K_s is primarily a result of the abiotic processes that influence interspace pedogenesis.

2.5 Acknowledgments

This work was supported by the National Science Foundation under NSF EPSCoR RING-TRUE III grant number EPS-447416. We thank Lynn Fenstermaker and

Ernesto Moran for assistance, and are grateful for the editorial skills of Roger Kreidberg and anonymous reviewers.

2.6 References

- Ankeny, M. D., M. Ahmed, T. C. Kaspar, and R. Horton (1991), Simple field method for determining unsaturated hydraulic conductivity, *Soil Sci. Soc. Am. J.*, *55*, 467-470.
- Bedford, D. R., and E. E. Small (2008), Spatial patterns of ecohydrologic properties on a hillslope-alluvial fan transect, central New Mexico, *Catena*, *73*, 34-48.
- Ben-Dor, E., and A. Banin (1989), Determination of organic-matter content in arid-zone soils using a simple "loss-on-ignition" method, *Commun. Soil Sci. Plant Anal.*, *20*, 1675-1695.
- Bhark, E. W., and E. E. Small (2003), Association between plant canopies and the spatial patterns of infiltration in shrubland and grassland of the Chihuahuan Desert, New Mexico, *Ecosystems*, *6*, 185-196.
- Caldwell, T. G., E. V. McDonald, and M. H. Young (2006), Soil disturbance and hydrologic response at the National Training Center, Ft. Irwin, California, *J. Arid Environ.*, *67*, 456-472.
- Dunkerley, D. L. (2000), Hydrologic effects of dryland shrubs: defining the spatial extent of modified soil water uptake rates at an Australian desert site, *J. Arid Environ.*, *45*, 159-172.
- Gardner, W. R. (1958), Some steady-state solutions of the unsaturated moisture flow equation with application to evaporation from a water table, *Soil Sci.*, *85*, 228-232.
- Gee, G. W., and D. Or (2002), Particle-size analysis, in *Methods of Soil Analysis, Part 4. Physical Methods*, edited by J. H. Dane and G. C. Topp, pp. 255-293, Soil Science Society of America Book Series, Madison.
- Gile, L. H., R. P. Gibbens, and J. M. Lenz (1998), Soil-induced variability in root systems of creosotebush (*Larrea tridentata*) and tarbush (*Flourensia cernua*), *J. Arid Environ.*, *39*, 57-78.
- Grover, H. D., and H. B. Musick (1990), Shrubland encroachment in southern New Mexico, USA - an analysis of desertification processes in the American southwest, *Climatic Change*, *17*, 305-330.
- Hamerlynck, E. P., J. R. McAuliffe, E. V. McDonald, and S. D. Smith (2002), Ecological responses of two Mojave Desert shrubs to soil horizon development and soil water dynamics, *Ecology*, *83*, 768-779.
- Hansen, D. J., J. D. Oster, and D. B. Hall (1999), The transition from Mojave Desert to Great Basin Desert on the Nevada Test Site, in *Proceedings of Shrubland Ecotones*, edited by E. D. McArthur, W. K. Ostler and C. L. Wambolt, p. 299, USDA Forest Service, Rocky Mountain Research Station Ft. Collins, CO.

- Jackson, R. B., J. Canadell, J. R. Ehleringer, H. A. Mooney, O. E. Sala, and E. D. Schulze (1996), A global analysis of root distributions for terrestrial biomes, *Oecologia*, *108*, 389-411.
- Logsdon, S. D., and D. B. Jaynes (1993), Methodology for determining hydraulic conductivity with tension infiltrometers, *Soil Sci. Soc. Am. J.*, *57*, 1426-1431.
- Lyford, F. P., and H. K. Qashu (1969), Infiltration rates as affected by desert vegetation, *Water Resour. Res.*, *5*, 1373-1376.
- Marion, G. M., P. S. J. Verburg, E. V. McDonald, and J. A. Arnone (2008), Modeling salt movement through a Mojave Desert soil, *J. Arid Environ.*, *72*, 1012-1033.
- McAuliffe, J. R., E. P. Hamerlynck, and M. C. Eppes (2007), Landscape dynamics fostering the development and persistence of long-lived creosotebush (*Larrea tridentata*) clones in the Mojave Desert, *J. Arid Environ.*, *69*, 96-126.
- McFadden, L. D., S. G. Wells, and J. C. Dohrenwend (1986), Influences of quaternary climatic changes on processes of soil development on desert loess deposits of the Cima volcanic field, California, *Catena*, *13*, 361-389.
- Nimmo, J. R., K. S. Perkins, K. M. Schmidt, D. M. Miller, J. D. Stock, and K. Singha (2009), Hydrologic characterization of desert soils with varying degrees of pedogenesis: 1. Field experiments evaluating plant-relevant soil water behavior, *Vadose Zone J.*, *8*, 480-495, 10.2136/vzj2008.0052.
- Ravi, S., P. D'Odorico, and G. S. Okin (2007), Hydrologic and aeolian controls on vegetation patterns in arid landscapes, *Geophys. Res. Lett.*, *34*, L24S23, doi:10.1029/2007GL031023.
- Reheis, M. C., J. C. Goodmacher, J. W. Harden, L. D. McFadden, T. K. Rockwell, R. R. Shroba, J. M. Sowers, and E. M. Taylor (1995), Quaternary soils and dust deposition in southern Nevada and California, *Geol. Soc. Am. Bull.*, *107*, 1003-1022.
- Rodriguez-Iturbe, I. (2000), Ecohydrology: A hydrologic perspective of climate-soil-vegetation dynamics, *Water Resour. Res.*, *36*, 3-9.
- Romeny, E.M., V.Q. Hale, A. Wallace, O.R. Lunt, J.D. Childress, H. Kaaz, G.V. Alexander, J.E. Kinnear and T.L. Ackerman (1973), Some characteristics of soil and perennial vegetation in the northern Mojave Desert areas of the Nevada Test Site., Atomic Energy Commission Rep. AT (04-1). U.S. Gov. Print. Office, Washington, DC.
- Scanlon, B. R., D. G. Levitt, R. C. Reedy, K. E. Keese, and M. J. Sully (2005), Ecological controls on water-cycle response to climate variability in deserts, *Proc. Natl. Acad. Sci. USA*, *102*, 6033-6038.
- Shafer, D. S., M. H. Young, S. F. Zitzer, T. G. Caldwell, and E. V. McDonald (2007), Impacts of interrelated biotic and abiotic processes during the past 125 000 years of landscape evolution in the Northern Mojave Desert, Nevada, USA, *J. Arid Environ.*, *69*, 633-657.
- Shiozawa, S., and G. S. Campbell (1991), On the calculation of mean particle diameter and standard-deviation from sand, silt, and clay fractions, *Soil Sci.*, *152*, 427-431.
- Wilcox, C. S., J. W. Ferguson, G. C. J. Fernandez, and R. S. Nowak (2004), Fine root growth dynamics of four Mojave Desert shrubs as related to soil moisture and microsite, *J. Arid Environ.*, *56*, 129-148.

Wooding, R. A. (1968), Steady infiltration from a large shallow circular pond, *Water Resour. Res.*, 4, 1259-1273.

Young, M. H., E. V. McDonald, T. G. Caldwell, S. G. Benner, and D. G. Meadows (2004), Hydraulic properties of a desert soil chronosequence in the Mojave Desert, USA, *Vadose Zone J.*, 3, 956-963.

2.7 Tables

Table 2-1. Means (\pm standard deviation) of binary (canopy vs. interspace) soil physical properties for both measured vegetation types: *L. tridentata* and *L. pallidum*.

Microsite	<i>n</i>	Organic Matter - % -	Bulk Density - g cm ⁻³ -	>2000 μ m - % -	2000 - 50 μ m - % -	50 - 2 μ m - % -	< 2 μ m - % -
<i>Larrea tridentata</i>							
Canopy	22	2.18 ^a (0.39)	1.23 ^a (0.14)	9.4 ^a (6.3)	74.7 ^a (6.0)	13.2 ^a (1.8)	2.7 ^a (0.4)
Interspace	59	1.61 ^b (0.21)	1.43 ^b (0.10)	18.9 ^b (6.8)	65.8 ^b (5.0)	12.0 ^b (2.7)	3.1 ^a (0.9)
<i>Lycium pallidum</i>							
Canopy	22	2.03 ^a (0.48)	1.22 ^a (0.14)	4.6 ^a (3.7)	79.4 ^c (3.4)	13.1 ^a (2.0)	2.6 ^a (0.6)
Interspace	58	1.51 ^b (0.25)	1.43 ^b (0.11)	19.4 ^b (6.8)	66.3 ^b (6.1)	11.3 ^b (1.8)	3.1 ^a (0.7)

^{a,b}distinct population based on ANOVA ($P < 0.05$)

Table 2-2 Means (\pm standard deviation) of binary (canopy vs. interspace) hydraulic properties for both measured vegetation types: *L. tridentata* and *L. pallidum*.

Microsite	K_s - cm h ⁻¹ -	α_{exp} - cm ⁻¹ -	$K_{-1.5}$ - cm h ⁻¹ -	$\alpha_{-1.5}$ - cm ⁻¹ -	$K_{-4.5}$ - cm h ⁻¹ -	$\alpha_{-4.5}$ - cm ⁻¹ -
<i>Larrea tridentata</i>						
Canopy	15.0 ^a (9.3)	0.234 ^a (0.08)	10.2 ^a (6.4)	0.249 ^a (0.10)	4.6 ^a (2.9)	0.210 ^a (0.08)
Interspace	27.7 ^b (16.5)	0.144 ^b (0.05)	20.8 ^b (11.7)	0.146 ^b (0.05)	14.0 ^b (8.7)	0.149 ^b (0.06)
<i>Lycium pallidum</i>						
Canopy	20.5 ^b (12.1)	0.206 ^a (0.08)	15.0 ^a (9.3)	0.221 ^a (0.10)	8.4 ^a (6.5)	0.177 ^a (0.07)
Interspace	26.5 ^b (15.4)	0.135 ^b (0.04)	20.6 ^b (10.4)	0.141 ^b (0.04)	12.9 ^b (7.2)	0.139 ^b (0.07)

^{a,b}distinct population based on ANOVA ($P < 0.05$)

Table 2-3. Correlation coefficients between R_{norm} and measured parameters for *L. tridentata* and *L. pallidum*, combined and individually.

	Combined data	<i>Larrea tridentata</i>	<i>Lycium pallidum</i>
<i>Physical Properties</i>			
Organic Matter	-0.65**	-0.73**	-0.63**
Bulk Density	0.71**	0.75**	0.69**
MPD	0.65**	0.47*	0.80**
σ	0.70**	0.60**	0.82**
>2000 μm	0.71**	0.58**	0.82**
2000 - 50 μm	-0.64**	-0.56**	-0.75**
50 - 2 μm	-0.38*	-0.17	-0.63**
<i>Hydraulic Properties</i>			
K_s	0.08	0.05	0.08
α_{exp}	-0.60**	-0.64**	-0.64**
$K_{-1.5}$	0.20	0.24	0.17
$\alpha_{-1.5}$	-0.54**	-0.59**	-0.50*
$K_{-4.5}$	0.32**	0.50**	0.26
$\alpha_{-4.5}$	-0.53**	-0.61**	-0.57**
n	67	35	34

MPD, mean particle diameter; σ , standard deviation for MPD

$P < 0.001$ (**), $P < 0.01$ (*)

2.8 Figures

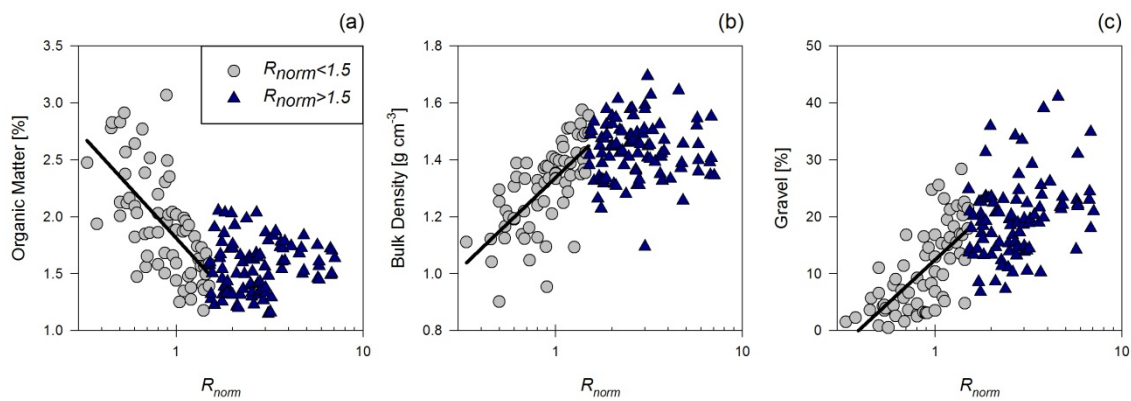


Figure 2-1. Spatial correlation of soil physical properties from canopy to interspace for (a) organic matter, (b) bulk density, and (c) gravel ($>2000 \mu\text{m}$)

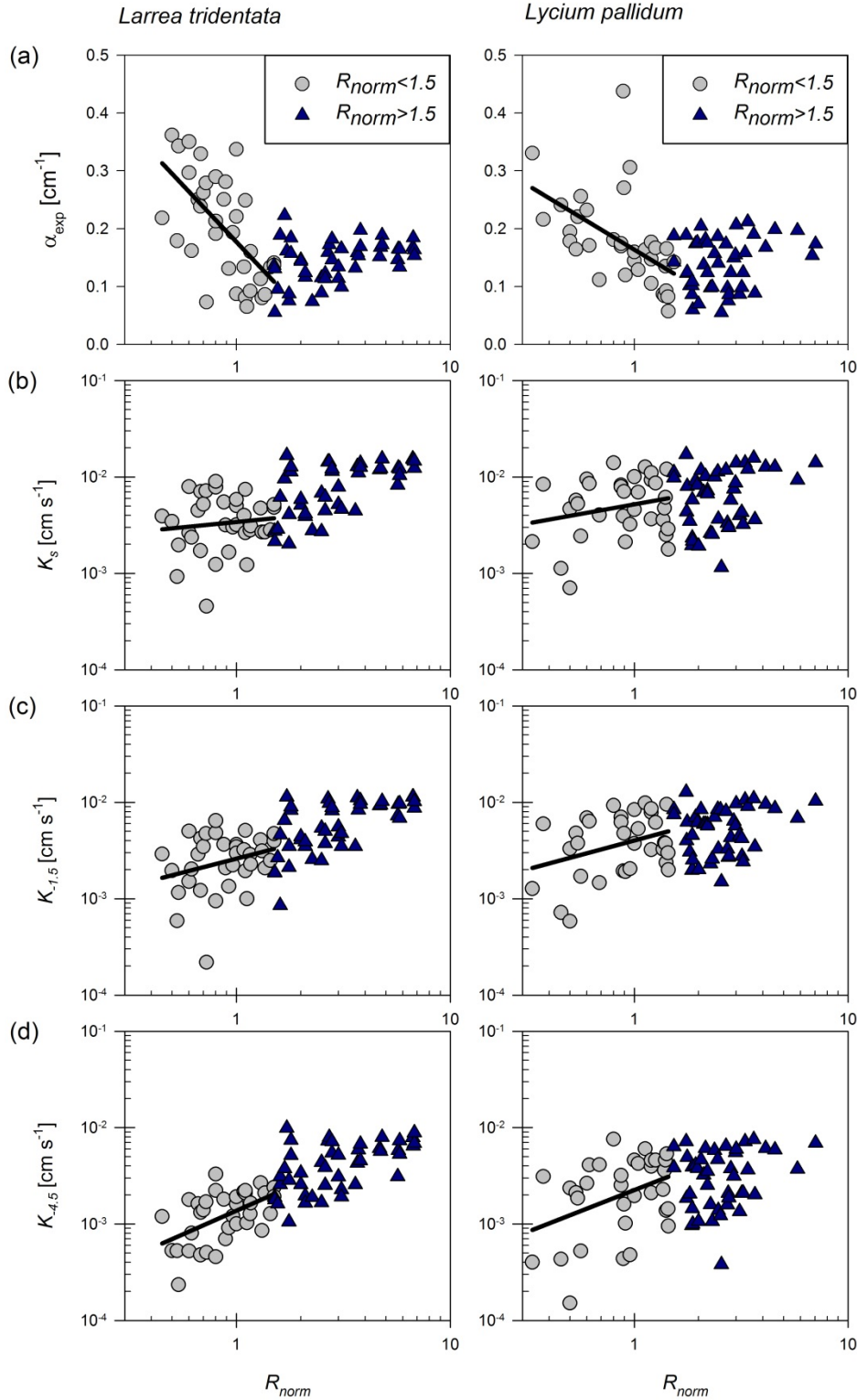


Figure 2-2. Spatial correlation of hydraulic parameters from canopy to interspace for α_{exp} (a and b); K_s or $K(\psi)$ at 0 cm H_2O (c and d), and piece-wise functions of $K(\psi)$ at -1.5 cm (e and f); and $K(\psi) = -4.5$ cm (g and h) for *L. tridentata* and *L. pallidum*, respectively.

3 BIOTIC AND ABIOTIC CONTROLS ON SOIL HETEROGENEITY IN ARID SHRUBLANDS

Todd G. Caldwell¹, Michael H. Young², Eric V. McDonald¹, Jianting Zhu³

¹Division of Earth and Ecosystem Sciences, Desert Research Institute, 2215 Raggio
Parkway, Reno, NV 89512

²Bureau of Economic Geology, Jackson School of Geosciences, University of Texas at
Austin, Austin, TX 78713

³Division of Hydrologic Sciences, Desert Research Institute, Nevada System of Higher
Education, Las Vegas, NV 89119

For submission to Water Resources Research

December 2011

* Corresponding author, E-mail: todd.caldwell@dri.edu; Tel.: +1 (775) 673-7368

Abstract

Geological and ecological processes play a critical role in the evolution of heterogeneous desert piedmonts. Arid alluvial fans consist of interspersed vegetation and bare soil often considered to be a binary system of canopy and interspace microsites. The feedbacks between biotic processes and soil development are not well-defined in either time or space. Thus, predicting their connection to ecosystem production or change is difficult. For this research, we will address these processes using high spatial-resolution infiltrometer measurements along transects radiating from canopies of perennial shrubs taken on a soil chronosequence in the Providence Mountains in the Mojave Desert. We used dimensionless spatial correlations to address role of bio-abiotic processes and the variability of soil physical properties in arid shrublands. Results found higher saturated conductivity under all vegetation regardless of surface age; however, this divergence was only retained on the older, developed soils and dissipated with unsaturated conditions. At proximal locations to the shrub, bulk density, soil structure grade, silt, and clay significantly increase away from the canopy; while sand and organic matter decrease. Distal locations had no significant correlation. The extent of this biotic influence was 1.34 ± 0.32 times the canopy radius. Hydraulic properties were weakly correlated in space but 75% of the variance could be attributed to sand, soil structure grade, mean-particle diameter, and organic matter – none of which are exclusively biotic or abiotic. Within the geomorphic age context presented here, the positive biotic feedback of higher conductivity underneath vegetation is most pronounced on interspace surfaces where the conductivity is lower. We propose that the current positive biotic feedback hypothesis is

not simply higher infiltration capacity underneath shrubs, but more directly related to the degree of soil development.

Index terms: Soils/pedology [1865], Eco-hydrology [1813], hydrologic scaling [1839], plant ecology [1851], soil moisture [1866]

3.1 Introduction

The ecohydrology of arid environments is strongly coupled to available water [Noy-Meir, 1973; Eagleson, 1978; Rodriguez-Iturbe *et al.*, 1999]. Soils serve as the buffer between the atmosphere and vegetation, regulating water, energy, and nutrient transfer, which ultimately controls primary production. Soil development in arid regions and the resulting morphology are functions of climate, biologic activity, and time. Soil texture and structure are temporally variable, evolving in time and space and ultimately affecting soil hydrologic functioning [McDonald *et al.*, 1996; Young *et al.*, 2004; Scanlon *et al.*, 2005; Meadows *et al.*, 2008].

Soil formation begins when depositional or erosional processes cease and the geomorphic surface becomes stable. The transformation of surficial sediment to soil (i.e., pedogenesis) affects a multitude of hydrologic processes operating across a range of spatial and temporal scales [McDonald *et al.*, 1996; Nimmo, 1997; Young *et al.*, 2004]. At the pore scale (μm – mm), soil development results in the formation of structure and secondary porosity [Meadows *et al.*, 2008]. At the field scale, vegetation patches and open soil (or interspace) affect infiltration [Dunkerley, 2002; Bedford and Small, 2008; Caldwell *et al.*, 2008], partitioning of evapotranspiration [Young *et al.*, 2009], and ultimately vegetation performance and community structure [Seyfried and Wilcox, 1995; Hamerlynck *et al.*, 2000; Hamerlynck *et al.*, 2002]. The feedback between vegetation and soil development is not well-defined in either time or space, and thus predicting their connection to ecosystem production or change is difficult. Ultimately, understanding how

small-scale variability impacts larger-scale processes is critical to examining whole ecosystem processes.

Soil development is investigated through the use of a chronosequence — a genetically related suite of soils evolving under similar vegetation, climate and topography with only time varying [Harden, 1982]. Chronosequence studies on arid alluvial fans generally assume that soil development is a quasi-linear transition from a geomorphically young soil to a mature soil, developing progressively under the influence of major soil-forming factors including climate, topography, biology, parent material, and time [Jenny, 1941]. For example, soil surfaces on arid alluvial fan complexes evolve from (younger) coarse-textured, bar and swale deposits into (older) smooth, desert pavements [McDonald *et al.*, 2003]. The primary driver for this pedogenic transformation is the influx and incorporation of dust [Reheis and Kihl, 1995], enriching alluvial deposits in silt, clay, and soluble salts. Low mean annual precipitation and high evaporative demand result in arid soils being net sinks for both dust and solutes.

With the onset of dust accumulation, soil development begins just below the surface with the formation of a vesicular horizon (Av), a silt-rich horizon ubiquitous to deserts. Infiltration capacity reduces with time [Young *et al.*, 2004] from this abiotic process of dust sequestration [Yaalon and Ganor, 1973; McFadden *et al.*, 1987]. As the Av horizon develops further, infiltration mechanisms shift from predominantly bulk matrix flow, due to the coarse texture and open pore-system, to a macropore-dominated system with flow constricted to faces of prismatic, highly structured pedes [Meadows *et al.*, 2008]. The hydraulic conductivity function [$K(\psi)$] is affected during this progression, thereby limiting infiltration and deeper percolation [McDonald *et al.*, 1996; Young *et al.*,

2004], and increasing near-surface water holding capacity and evaporative losses [Young *et al.*, 2009]. Ultimately, plant available moisture is reduced due to this attenuation of precipitation [Hamerlynck *et al.*, 2002].

The temporal scales for bio-abiotic processes vary considerably. Biotic processes operate at shorter time scales (10s to 100s of years), and abiotic processes operate over longer time scales (up to about 2.5 Ma). Spatially, biotic processes are confined to the shrub (i.e., meter) scale, while abiotic processes operate at the basin scale. The heterogeneous arid shrubland evolves through these coupled processes that operate at dramatically different spatial and temporal scales [Shafer *et al.*, 2007].

Our previous study found a dimensionless, spatial gradient in hydraulic properties from canopy to interspace microsites, more prevalent at negative soil-water potentials [Caldwell *et al.*, 2008]. Gradients in physical and hydraulic properties require establishment of the canopy and underlying mound, but the relative age of the shrub and associated soil can vary greatly. Saturated hydraulic conductivity of interspace soils ranges from $>100 \text{ cm h}^{-1}$ on young surfaces to $<1 \text{ cm h}^{-1}$ on soils with well-developed Av horizons [Young *et al.*, 2004; Caldwell *et al.*, 2006; Nimmo *et al.*, 2009b; Stevenson *et al.*, 2009] but no significant reduction with geologic time has been observed under canopy [Shafer *et al.*, 2007]. This pedologic co-evolution of desert soils leads to smaller *L. tridentata*, higher *A. dumosa* mortality, and generally negative impacts to overall plant performance [Hamerlynck *et al.*, 2002]. For this research, the unsaturated hydraulic conductivity measured underneath canopies is hypothesized in to be independent of surface age, because the pedogenic clock is essentially reset by bioturbation underneath vegetation. The chronosequence is used to examine shrub-scale processes on geomorphic

surfaces of different ages, thus providing the means to explain differences in soil structure and texture and hydraulic properties. Specifically, we seek to answer the questions:

1. Within a geomorphic context, is the infiltration greater under canopy?
2. Do biotic or abiotic factors affect hydraulic properties and surface heterogeneity?
3. Do similar spatial gradients exist between microsites (Caldwell et al., 2008)?

3.2 Materials and Methods

This study was conducted using an intensely studied geomorphic chronosequence in the Providence Mountains located in the eastern Mojave Desert, USA [McDonald et al., 1996; Hamerlynck et al., 2002; McDonald et al., 2003; Young et al., 2004; Meadows et al., 2005; 2006; Meadows et al., 2008; Nimmo et al., 2009b; Nimmo et al., 2009a]. Three soils of the mixed plutonic (PM) alluvium sequence (primarily syenite, syenogranite, and monzodiorite) were studied, including a young, late-Holocene (Qf7, ~0.5 ka); an intermediate, mid-Holocene (Qf5, ~4 ka); and an older, Pleistocene (Qf3, ~75 ka) geomorphic surface (Figure 3-1). These surfaces were chosen because they (1) represented a significant proportion of the watershed; (2) appeared to be intact, with little evidence of past surface erosion [Meadows et al., 2008]; (3) differed significantly in their interspace hydraulic properties [Young et al., 2004]; and (4) differed significantly in vegetation volume and plant numbers [Hamerlynck et al., 2002]. The mapped geomorphic units within the watershed boundary of the PM sequence cover 24.2 km², of which 10% is Qf7, 17% is Qf5, and 23% is Qf3. The older soils (Qf2 and Qf1) in this

sequence were likely eroded and do not necessarily resemble the sequence of pedogenic development [Meadows *et al.*, 2008].

Vegetation at the site consists primarily of the evergreen *Larrea tridentata* (creosotebush) and drought-deciduous *Ambrosia dumosa* (white bursage) [Hamerlynck *et al.*, 2002]. The largest basal diameters and canopy volumes for individual *L. tridentata* shrubs were found on the youngest, Qf7 unit, both decreasing with surface age. Total plant numbers (per area) were found to increase with surface age, yet total canopy cover reduced with surface age [Hamerlynck *et al.*, 2002].

Soil and hydraulic properties were determined using discrete sampling and measurements of unsaturated hydraulic conductivity [$K(\psi)$] along transects radiating outward from the near-center of each shrub into the interspace. Six shrubs were randomly chosen within each of the three 20 by 30m experimental plots [e.g., Yin, 2008]. Measurements of $K(\psi)$ were simultaneously conducted using an array of seven, independently operated, modified mini-disk (4.5 cm diameter) tension infiltrometers ([MDTI] (Model S; Decagon Devices; Pullman, WA), allowing precise control of the water supply head or potential (ψ) via a Marriotte column from near saturation (0 kPa) to -0.6 kPa. Measurement locations were spaced at 25 cm within the canopy projection and 50 cm beyond.

Outflow data from each MDTI was analyzed for steady-state unconfined infiltration from a circular source given by [Wooding, 1968]:

$$q(\psi) = K_s \exp(\alpha\psi) \left[1 + \frac{4\lambda_c}{\pi r} \right]$$

(1)

where $q(\psi)$ is the steady state flux ($L^3 t^{-1}$), K_s is the saturated conductivity ($L t^{-1}$), r is the infiltrometer radius (L), and λ_c is the macroscopic capillary length (L). The relationship assumes an initially dry, homogeneous, anisotropic and uniformly unsaturated soil.

Wooding's analysis is based upon the unsaturated conductivity function, $K(\psi)$, defined by [Gardner, 1958]:

$$K(\psi) = K_s \exp(\alpha\psi) \quad \psi < 0 \quad (2)$$

where scaling parameter, α , is the derivative of the hydraulic conductivity function with respect to capillary forces and equal to $1/\lambda_c$.

Using the MDTI through a range of pressures, two analytical solutions were obtained: (1) as a continuous exponential function [Logsdon and Jaynes, 1993] and (2) as a piece-wise continuous function of $K(\psi)$ and $\alpha(\psi)$ for the midpoint between each supply head [Ankeny *et al.*, 1991]. The shuffled complex evolution algorithm [Duan *et al.*, 1992] was used to minimize the sum of squares residuals between observed and calculated q resulting in a continuous, exponential function containing K_s and α . The piece-wise solutions result in a ψ of -6, -3, and -0.1 cm H₂O results in $K_{4.5}$ and $K_{1.5}$ and corresponding α values $\alpha_{4.5}$ and $\alpha_{1.5}$, respectively.

All K measurements were normalized to 20°C using the correction factor (C) derived from known changes of water viscosity and density [Lide, 2001] as function of the monitored water temperature by:

$$C = 0.2513 + 1.150 \exp\left(-\frac{T}{28.83}\right) \quad (3)$$

where T is median water temperature during each infiltration test which was monitored during each run.

Following each MDTI test, a soil core (270 cm³) was taken underneath each infiltration point to determine dry bulk density. A semi-quantitative measure of soil structure grade (*Sg*) [Schoeneberger *et al.*, 2002] was determined from the aggregate quality and consistence evident in a hand sample. A ranking between 0 and 3 was determined by as: 0 = structureless — lacking any cohesion or strength; 1 = weak— aggregates barely visible in place and but present in hand sample with minimal strength; 2 = moderate — well-formed and evident structure in place and moderately cohesive in hand sample; and 3 = strong — obvious in place aggregates with prismatic structure and strong cohesion in hand sample. Soil from each core was analyzed for organic matter by loss-on-ignition [Ben-Dor and Banin, 1989] and particle size distribution using a combination of mechanical sieving and laser light diffraction (Micromeritics Saturn DigiSizer 5200, Norcross, GA). Oven dry soils were mechanically sieved to 2, 1, and 0.5 mm. The <0.5mm fraction was analyzed by laser light diffraction [Loizeau *et al.*, 1994; Gee and Or, 2002]. The data were reassembled to calculate the geometric mean particle diameter (*MPD*) and its log standard deviation (σ) from [Shiozawa and Campbell, 1991]:

$$MPD = \sum m_i \ln d_i \quad (4)$$

$$\sigma = \sqrt{\sum m_i (\ln d_i)^2 - MPD^2} \quad (5)$$

where m_i is the mass fraction (or equivalent volume fraction produced from laser light scattering) in each separate size bin i of diameter d . Laser data were reduced to 20 logarithmically decreasing size bins and combined with sieved data.

All point measurements were spatially normalized to a single radial distance (R_{norm}) relative to their respective vertical projection of the canopy by:

$$R_{norm} = \frac{Z}{Z_{canopy}} \quad (6)$$

where measurements from canopy center to edge, Z_{canopy} (cm), are divided by position (Z) along the length of each transect. A point within the canopy will thus have an $R_{norm} < 1$ and a point beyond the canopy will have an $R_{norm} > 1$.

Lastly, statistical tests were performed for both a binary population (canopy or interspace microsite) and a spatial R_{norm} linear regression approach. For the binary approach, a two-factor analysis of variance (ANOVA) was used to determine the effects between geomorphic surface and microsite (BIN) using an unbalanced, general linear model. For significant combined effects (Surface x BIN), post hoc tests between groups were determined by step-down, pair-wise differences by Sidak-Holms t-test at alpha < 0.05 . All parameters were tested for normality (Shapiro-Wilk) and equal variance prior; K_s and α failing normality tests were log-transformed prior to statistical tests. Spearman correlations were used to determine significant spatial correlation to R_{norm} and K_s , and a backward, step-wise multiple linear regression was used to determine the most significant dependent variables for predicting K_s . All statistical tests were performed using SigmaPlot (Systat Software, version 11).

3.3 Results

A total of 125 infiltrometer measurements were conducted radially away from 17 randomly chosen shrubs (14 *L. tridentata*, and 3 *A. dumosa*) on the three geomorphic surfaces (young [Qf7], intermediate [Qf5] and old [Qf3]) as discussed above. The radius of measured shrubs ranged from 0.3 to 1.2 m with a mean of 0.73 m. Shrub height ranged

from 0.3 to 1.3 m and the estimated canopy volume using an inverted cone [Hamerlynck *et al.*, 2002] at measurement locations range from 0.028 to 1.26 m³.

3.3.1 Canopy and Interspace Microsites

The 2-factor ANOVA for microsite (BIN), geomorphic surface, and their interactions showed that all measured physical properties in BIN were significant, except *MPD*; for geomorphic surface, all measured properties except gravel content were significant; and their interactions were significant for every property except density and silt content (Table 3-1). Post hoc tests for these factors indicate significantly ($p < 0.001$) lower values of bulk density at all canopy microsites and the lowest values for all microsites on the Qf3 ($p < 0.001$). Soil structure grade (*Sg*) was significantly ($p < 0.001$) lower underneath canopies, including the interaction across all geomorphic surfaces ($p < 0.001$). Additionally, soil *SG* increased with surface age ($p < 0.001$). Particle size distribution parameters indicated an increasing fine-fraction, both with increasing surface age and across interspace microsites, and greater sand content underneath canopies. A distinct separation in textures between microsites occurred on both the Qf3 and Qf5, but not on the Qf7. Lastly, organic matter had significant factors and interactions with higher values underneath canopies and increasing with surface age (Table 3-1). Generally, values were low and typical of an arid, patchy ecosystem. The Qf7 unit has particularly low values ($0.78 \pm 0.15\%$) at interspaces, but increases underneath canopies ($1.13 \pm 0.27\%$).

Two-factor ANOVA results for measured (log-transformed) hydraulic properties also indicated significant relationships for both BIN and surface (Table 3-2). However,

only K_s and $K(-4.5\text{cm})$ had significant combined factors. Saturated hydraulic conductivities were significantly ($p < 0.001$) greater underneath canopies with arithmetic mean (\pm one standard deviation) K_s of $252 \pm 128 \text{ cm d}^{-1}$ versus $199 \pm 193 \text{ cm d}^{-1}$ found in interspaces (Figure 3-2a). The parameter α was higher underneath canopies ($0.275 \pm 0.08 \text{ cm}^{-1}$) versus interspaces ($0.179 \pm 0.08 \text{ cm}^{-1}$) (Figure 3-2b), indicating that the hydraulic conductivity will decrease at a faster rate with decreasing matric potential beneath shrub canopies than in the interspaces.

Hydraulically, the K_s values decreased significantly (log-transformed, $p < 0.001$) with surface age and were dissimilar between microsites on older Qf5 and Qf3 units (Figure 3-2). Values at the interspace microsites were lowest on the Qf3 ($84.2 \pm 63 \text{ cm d}^{-1}$), intermediate on the Qf5 ($122 \pm 87 \text{ cm d}^{-1}$), and highest on the Qf7 ($372 \pm 221 \text{ cm d}^{-1}$). Values underneath canopies, however, were similar ($p > 0.05$) across the Qf3, Qf5, and Qf7 with mean values of 141 ± 75 , 245 ± 65 and $342 \pm 140 \text{ cm d}^{-1}$, respectively. Similar to the BIN results between microsite, α was significantly ($p < 0.05$) greater underneath all canopies (Figure 3-2). The separation of hydraulic conductivity between canopy and interspace microsites diminished as the soil became unsaturated (Figure 3-3). This convergence occurred at $\psi = -4 \text{ cm}$ on the Qf3 unit (Figure 3-3a) and $\psi = -8 \text{ cm}$ on the Qf5 unit (Figure 3-3b). However, on the youngest, Qf7 surface, with similar K_s values on both microsites but with a lower α at the interspace, hydraulic conductivity values diverge at $\psi < -4 \text{ cm}$ resulting in a higher interspace K (Figure 3-3c).

3.3.2 Spatial Dependency of Soil and Hydraulic Properties

The biotic influence can be further examined by reducing the data set and assessing these gradients between proximal (near-shrub) and distal (interspace) location. In this section, we use dimensionless spatial correlation between R_{norm} and measured soil properties (1) for all locations and between proximal ($R_{norm} < 1.5$) and distal ($R_{norm} > 1.5$) locations from shrubs, (2) across all surfaces, and (3) for each surface. First, no significant gradients were observed at any distal locations, further indicating the significance of biotic processes operating at the shrub level (Table 3-3). At proximal locations on all geomorphic surfaces, density ($p < 0.01$), σ ($p < 0.001$), gravel ($p < 0.001$), and clay ($p < 0.05$) increase away from the shrub center, while sand ($p < 0.001$), organic matter ($p < 0.01$) and α ($p < 0.05$) decrease. These results indicate a significant gradient radiating from the shrubs with a biologic origin and suggest that nutrient cycling has enriched canopy soils with organics, and bioturbation has reducing density through mixing and sorting of the soil underneath the shrubs. In addition, eolian-derived sand was preferentially retained under shrubs while silt and clay were sequestered at interspaces.

Reducing the data set further to geomorphic surface (i.e., abiotic time) again resulted in no significant correlations at distal locations; however, many of the prior relationships were retained (Table 3-3). Spatial correlations were no longer significant on the oldest surface (Qf3) for gravel; on the intermediate surface (Qf5) for density, organic matter, or α ; and on the youngest surface (Qf7) for σ , gravel, sand, or α . Thus, correlations for physical soil properties appear to increase with time since the Qf3 and Qf5 retained many of these significant relationships while the Qf7 retained few.

No significant spatial correlations to K_s were observed, but α was found to have a strong ($p < 0.001$) negative correlation to R_{norm} (Table 3-3). The hydraulic conductivity at saturation, $\psi_{-1.5}$, and $\psi_{-4.5}$ (piece-wise analytic solutions) illustrates, spatially, how these two parameters interact on contrasting geomorphic units (Figure 3-4). For example, the oldest (Qf3) surface with the lowest overall conductivity ($p < 0.001$) across all locations was found to have higher K_s underneath canopies (Figure 3-4a). The $K_{-1.5}$ in this microsite quickly declined as a result of the higher α (Figure 3-4b). As a result, $K_{-4.5}$ in the interspace microsite was somewhat greater ($40.0 \pm 20 \text{ cm d}^{-1}$) than underneath the canopy ($32.8 \pm 14 \text{ cm d}^{-1}$) (Figure 3-4c). A similar trend was observed for the Qf5 surface, where higher K_s and α underneath canopies were recorded, yet as the soils dry (tension $\psi_{-4.5}$), the interspace hydraulic conductivity was found to be similar ($66.5 \pm 120 \text{ cm d}^{-1}$) to that recorded underneath canopies ($62.5 \pm 25 \text{ cm d}^{-1}$) (Figures 3-4f). We also noted that the variability decreased underneath canopies but remained relatively higher in the interspace microsites. Finally, for the young (Qf7) surface, where similar K_s values were recorded at both microsites, a greater α underneath canopies indicates that hydraulic conductivity will change at different rates with increasing tension, diverging at $\psi_{-1.5}$ (Figure 3-4h). Results showed that hydraulic conductivity in the interspace microsite maintained a higher value ($121 \pm 55 \text{ cm d}^{-1}$) and variability at $\psi_{-4.5}$ than the under-canopy microsite ($70.2 \pm 29 \text{ cm d}^{-1}$) (Figure 3-4i).

3.3.3 Spatial Extent of the Measured Gradients

We calculated the spatial extent of the biotic influence by intersecting the means of the distal parameters (Table 3-1) with values (respective slopes and intercepts) obtained from significant ($p < 0.01$) correlations of proximal properties and $R_{norm} < 1.5$ from Table 3-3. The extent of this gradient with respect to R_{norm} could be useful for scaling soil properties based on canopy projections from remote sensing for either binary or gradients between microsites.

Five significant gradients were measured at proximal R_{norm} values; these correlations intersected mean distal values of R_{norm} distance ranging from 0.81 to 1.61 with a mean of 1.34 ± 0.32 (Table 3-4). Similar ranges were found using the significant correlations on each geomorphic surface. The increasing gravel content showed the lowest extent ($R_{norm} \sim 0.9$) while density and σ had larger extents ($R_{norm} \sim 1.6$). In our previous study [Caldwell *et al.*, 2008], we found that the spatial influence of the canopy microsite to be 1.4 times the shrub radius and independent of direction. Considering that the desert scrub vegetation is similar, but the site is located 100s of kilometers away, it is notable that a similar extent of 1.34 times the canopy radius was measured.

3.3.4 Biotic and Abiotic Factors Controlling the Evolution of K_s

The previous sections reported on spatial correlations found in these heterogeneous arid shrublands, of which K_s was generally weak. In this section, we consider the factors contributing to the variability of K_s across (1) all locations, (2) proximal and distal locations, then for (3) each geomorphic unit. Many strong ($p < 0.001$) relationships exist for K_s across all locations including positive correlations to *MPD*, sand

content, and α ; and negative correlations to soil S_g , σ , silt and clay contents (Table 3-5). Thus, weakly-structured, coarser, well-graded soils have justifiably higher K_s . Parsing the data set into proximal and distal R_{norm} retained many of these prior correlations to $p < 0.001$ for K_s for both locations; the exceptions being proximal soil S_g and MPD . These two factors have more significant influence on distal properties across all geomorphic units, indicating a more abiotic process. With the exception of α , no significant proximal correlations were found on the Qf7 and only three weak ($p < 0.05$) proximal correlations were found on the Qf5. Thus, the shrub influence tends to overprint the general abiotic factors controlling K_s . Surprisingly; we found little correlation to organic matter underneath shrub canopies. The only significant correlation underneath canopies is related to decreasing σ and increasing α .

A backward stepwise multiple linear regression (bMLR) was used to determine the physical soil factors controlling our ability to predict K_s as a dependent variable. The method allows us to begin with all available measurements and sequentially remove the least significant relationships until the minimum set of variables remain, maximizing adjusted R^2 . One factor in the bMLR must be kept constant; we chose to use the physical property sand (the strongest linear relationship) as this factor. The resultant, empirical equation was:

$$\begin{aligned} \text{Log}(K_s) = & 1.46 - 0.117(\text{Soil } S_g) + 0.0172(\text{sand}) \\ & - 6.32 \times 10^{-4}(\text{MPD}) - 0.108(\text{organic matter}) \end{aligned} \quad (7)$$

which contained only 4 significant factors: soil S_g ($p < 0.001$), sand ($p < 0.001$), MPD ($p = 0.002$), and organic matter ($p = 0.065$). The final empirical relationship yielded a $R^2 =$

0.748, a standard error of 0.192, and a slope very close to unity of 0.993 (Figure 3-5). These four factors control nearly 75% of the variability in K_s .

3.4 Discussion and Conclusions

Soil structure in arid soils and ultimately its hydrologic function is influenced by a combination of biotic and abiotic processes. Biological processes disrupt structure through bioturbation but also form cohesion by the added organic matter. The latter results in weak, blocky soil peds that would rank lower on our semi-quantitative scheme. Soil S_g was also positively correlated to R_{norm} (structure increases toward interspaces), where abiotic processes tend to dominate through the sequestering of eolian material and the formation of desert pavement. This observation is further verified by the lower sand content and higher σ in interspace microsites. In a previous study by *McAuliffe and McDonald* [2006], they reported that higher sand content underneath canopies was likely caused by selective displacement of sand to the surface by foraging and burrowing macro- and micro-fauna, leading to a lower bulk density strongly correlated to R_{norm} underneath canopies.

Organic matter ultimately increased with time at all microsites. The production is clearly a biotic process; however, its sequestration in the interspace soil has an abiotic component as well. Biogeochemical reactions that would oxidize and remove this material from interspace microsites are likely controlled by hydrologic response and aridity, both of which limit available soil moisture. Thus, the results point to a soil system evolving over millennium and a plant system working to maintain a hydrologically

favorable habitat over its lifespan. For the case of *L. tridentata*, this time period may be an equally long time [McAuliffe *et al.*, 2007]. Given that the divergence in microsites was not observed on the youngest (~500 year old) surface and the gradient became more significant on the ~80-100 ka Qf3, longer geologic time frames are required to form and maintain both the 'island of fertility' and the surrounding interspace soils. Thus, it is likely that these shrub islands are occupied by vegetation over quaternary time scales.

Quade [2001] suggested a lack of desert pavement surfaces above 400 m during the last glacial maximum (~15 ka) in Death Valley and the surrounding areas due to extensive downward shifts in ecotones. The distal alluvial fans of the Providence Mountains are at >1000 m [McDonald *et al.*, 2003], suggesting that our Qf3 and Qf5 study sites were devoid of desert pavements. Given the significant divergence of soil physical properties between sites with well-developed (Qf3) and moderately-developed (Qf5) pavements and vesicular Av horizons around active plant mounds, the pavements must 'heal' very quickly during the retreat of vegetation; or they remained intact during the Last Glacial Maximum [McFadden *et al.*, 1998]. The latter seems more plausible although our results do not fully address the question of whether desert shrubs occupy mound microsites permanently or ephemerally.

Within the geomorphic context presented here, the positive biotic feedback is most pronounced on interspace surfaces where the hydraulic conductivity is lower and the soil more developed. We propose that the current hypothesis of positive biotic feedback on higher infiltration capacity underneath shrubs [Lyford and Qashu, 1969; Eckert *et al.*, 1979; Dunkerley, 2000; Bedford and Small, 2008] be stated more generally

that conditions are hydrologically favorable: *Greater infiltration capacity is only favorable when surrounded by low conductivity soil.* Without any geomorphic context, we suggest that this hypothesis cannot be supported. Indeed, it is likely that a lower infiltration capacity and higher water holding capacity exists underneath canopies. This situation has been found on vegetated sand dunes in the Chihuahuan Desert [Ravi *et al.*, 2007] and on young alluvial surfaces in the northern Mojave [Caldwell *et al.*, 2008]. Recent studies using continuous monitoring systems have further illustrated that moisture conditions underneath canopies are not necessarily more favorable for shrub growth and vitality [Lebron *et al.*, 2007; Duniway *et al.*, 2010; Moran *et al.*, 2010]. The study described herein found similar K_s values between microsites on the youngest (Qf7) geomorphic surface. Similar results were found at a site in the northern Mojave Desert on a 500-year old surface [Shafer *et al.*, 2007]. The spatial extent influenced by vegetation was not as evident in this work as reported in previous studies [Dunkerley, 2000; Caldwell *et al.*, 2008; Madsen *et al.*, 2008] ranging from 1.4 to 3 times the canopy projection. Nevertheless, the interspace microsites clearly evolve at a different spatial and temporal scale than soils found beneath canopies.

The results show that soil physical properties support the hypothesis that arid system pedogenesis enriches each unit with fine particles, most likely through the sequestration of dust, resulting in increased soil development with geologic age [McFadden *et al.*, 1998]. In arid alluvial fan systems, this process is primarily associated with the development of a desert pavement and vesicular horizon that are extensive across the desert southwest [Turk and Graham, 2011] and have been shown to reduce interspace conductivity. Caldwell *et al.* [2006], Shafer *et al.* [2007] and Nimmo *et al.*

[2009b] found a five-fold decline, and Young et al. [2004] found a 100-fold decline in interspace K_s with the development of a vesicular horizon. Our results show a significant but modest 2.4-fold decrease between the Qf3 and Qf7 interspaces.

In general, the literature is heavily skewed with studies that measure soil hydraulic properties using ponded head conditions. Our results illustrate that alluvial fan soil hydrology is a more complicated function of the unsaturated hydraulic conductivity and the surface flux (i.e., precipitation \pm surface water). Ponded head measurements cannot capture these nuances and thus are not the preferred method for characterizing soils as a means to understand soil recharge. For example, mean wintertime and summertime precipitation intensity in the Mojave is 2 and 5 cm d⁻¹, respectively [Redmond, 2009]. The 100-year, 1 hour rainfall total is 91-122 cm d⁻¹ (1.5-2.0 inches h⁻¹) in the Mojave Desert region [U.S. Department of Commerce, 1961]. More recent analyses using point precipitation frequency estimates from the Daggett Airport meteorological station in the central Mojave Desert estimates the 100-year, 5-min precipitation intensity to be approximately 1.42 cm h⁻¹ (equivalent to 410 cm d⁻¹) [Bonnin et al., 2004]. Therefore, the potential to generate ponded conditions is unlikely for all but the most infrequent and high intensity storms. Likewise, saturated conditions are unlikely to occur on the younger alluvial surfaces (Qf7), which tend to have larger, more interspersed shrubs [Hamerlynck et al., 2002]. Without sustained, saturated conditions and the flux to maintain them, macropores (root channels, borrows, worms holes, etc.) are not participating in downward flow – they remain unsaturated.

Nutrient cycling underneath canopies leads to a net increase in organic material compared to corresponding interspaces [Schlesinger et al., 1996]. Time also leads to

higher organic matter content, as was shown here. The lower soil S_g and sandier texture underneath canopies further support the hypothesis that bioturbation minimizes the development of soil structure. Burrowing rodents mechanically sort the substrate preferentially beneath shrub canopies [McAuliffe and McDonald, 2006]. The higher α and lower σ found in under-canopy microsites suggest a sandy, more uniform pore-size distribution that quickly drains under tension, not necessarily a system of large macropores and root channels. The water holding capacity is also lower for sandy soil, corresponding to a higher α , versus, a more silt-rich vesicular horizon [Young *et al.*, 2004]. This lower water holding capacity underneath canopies reduces the percentage of soil water lost to evaporation [Kurc and Small, 2004; Young *et al.*, 2009], hence increasing the ecohydrological benefit to the plant.

3.5 Tables

Table 3-1. Mean (\pm one standard deviation) soil physical properties and 2-factor ANOVA results for microsite (BIN), geomorphic surface and combined

Surface	BIN	<i>n</i>	DENSITY [g cm ⁻³]	Structure -	MPD [μ m]	σ [μ m]	Gravel [%]	Sand [%]	Silt [%]	Clay [%]	Organics [%]									
	All	125	1.43 (0.16)	1.2 (0.8)	173 (113)	10.4 (3.4)	18.1 (9.93)	51.6 (13)	24.0 (7.7)	6.2 (5.0)	1.14 (0.35)									
All	IS	82	1.50 (0.11)	1.3 (0.9)	171 (127)	11.3 (3.7)	19.6 (9.93)	47.8 (13)	25.3 (8.7)	7.3 (5.8)	1.05 (0.31)									
	Canopy	43	1.31 (0.15)	0.9 (0.5)	176 (79.0)	8.6 (1.8)	15.3 (9.41)	59.0 (9.1)	21.7 (4.4)	4.0 (1.6)	1.31 (0.36)									
Qf3	IS	23	1.43 (0.10)	2.0 (0.8)	114 (104)	12.8 (2.8)	18.9 (13.4)	39.2 (9.5)	30.8 (9.1)	11.0 (6.4)	1.31 (0.28)									
(old)	Canopy	12	1.18 (0.12)	0.8 (0.3)	160 (95.8)	10.6 (1.9)	20.6 (14.2)	48.5 (9.6)	25.4 (4.4)	5.5 (1.3)	1.69 (0.33)									
Qf5	IS	30	1.55 (0.12)	1.6 (0.8)	146 (112)	13.2 (3.9)	21.0 (10.2)	43.0 (11)	26.9 (7.7)	9.0 (5.3)	1.12 (0.26)									
(inter.)	Canopy	15	1.38 (0.16)	1.0 (0.6)	137 (46.0)	8.4 (1.0)	10.9 (4.86)	62.2 (4.6)	22.5 (3.0)	4.6 (1.0)	1.19 (0.25)									
Qf7	IS	29	1.49 (0.09)	0.5 (0.6)	243 (129)	8.0 (1.0)	18.6 (5.62)	59.5 (4.8)	19.1 (5.2)	2.7 (1.0)	0.78 (0.15)									
(young)	Canopy	16	1.33 (0.11)	0.8 (0.5)	224 (67.3)	7.4 (0.7)	15.4 (6.07)	63.9 (4.8)	18.3 (2.8)	2.4 (0.6)	1.13 (0.27)									
2-factor ANOVA			<i>F</i>	<i>p</i>	<i>F</i>	<i>p</i>	<i>F</i>	<i>p</i>	<i>F</i>	<i>p</i>	<i>F</i>	<i>p</i>	<i>F</i>	<i>p</i>	<i>F</i>	<i>p</i>	<i>F</i>	<i>p</i>		
BIN			74.7	<0.001	13.2	<0.001	0.10	0.753	30.5	<0.001	4.55	0.04	48.8	<0.001	8.81	0.004	22.0	<0.001	31.9	<0.001
Surface			15.9	<0.001	13.1	<0.001	11.0	<0.001	28.7	<0.001	1.39	0.25	42.1	<0.001	20.9	<0.001	22.4	<0.001	41.8	<0.001
BIN x Surface			1.55	0.217	11.4	<0.001	1.00	0.371	8.15	<0.001	3.44	0.04	8.38	<0.001	1.34	0.27	4.66	0.01	4.40	0.01

IS, interspace microsite; *Sg*, structure grade; *MPD*, mean particle diameter; σ , MPD standard deviation

Table 3-2. Mean (\pm one standard deviation) hydraulic properties including the continuous and piece-wise $K(\psi)$ functions and 2-factor ANOVA results for microsite (BIN), geomorphic surface and combined

Surface	Bin	n	K_s [cm d ⁻¹]	α [cm ⁻¹]	$K(-1.5\text{cm})$ [cm d ⁻¹]	$\alpha(-1.5\text{cm})$ [cm ⁻¹]	$K(-4.5\text{cm})$ [cm d ⁻¹]	$\alpha(-4.5\text{cm})$ [cm ⁻¹]						
	ALL	125	218 (175)	0.212 (0.09)	155 (114)	0.231 (0.12)	71.1 (69.5)	0.170 (0.08)						
ALL	IS	82	199 (193)	0.179 (0.08)	152 (134)	0.191 (0.09)	78.4 (82.6)	0.151 (0.07)						
	Canopy	43	252 (128)	0.275 (0.08)	159 (64)	0.306 (0.12)	57.2 (28.2)	0.205 (0.10)						
Qf3 (old)	IS	23	84.2 (63.0)	0.141 (0.05)	64.4 (43)	0.142 (0.06)	40.1 (22.3)	0.137 (0.05)						
	Canopy	12	141 (75.0)	0.255 (0.09)	93.9 (43)	0.282 (0.10)	32.8 (13.7)	0.174 (0.07)						
Qf5 (inter.)	IS	30	122 (86.8)	0.171 (0.08)	120 (126)	0.188 (0.10)	66.5 (112)	0.130 (0.06)						
	Canopy	15	245 (65.4)	0.255 (0.04)	170 (42)	0.284 (0.05)	62.7 (24.6)	0.178 (0.05)						
Qf7 (young)	IS	29	376 (221)	0.219 (0.08)	256 (123)	0.233 (0.09)	121 (55.1)	0.185 (0.07)						
	Canopy	16	342 (139)	0.309 (0.09)	197.2 (59)	0.343 (0.17)	70.2 (29.0)	0.253 (0.13)						
2-Way ANOVA			F	p	F	p	F	p	F	p	F	p		
BIN			18.7	<0.001	49.6	<0.001	8.13	0.005	14.04	<0.001	0.89	0.347	14.04	<0.001
Surface			42.4	<0.001	8.08	<0.001	36.7	<0.001	9.10	<0.001	25.6	<0.001	9.10	<0.001
BIN x Surface			6.53	0.002	1.02	0.365	6.38	0.002	0.27	0.77	5.26	0.006	0.27	0.765

IS, interspace microsite; K_s , saturated conductivity; α , derivative of the hydraulic conductivity function

Table 3-3. Pearson correlation coefficients between soil physical characteristics to the normalized radial distance (R_{norm}) for all locations, distal ($R_{norm} > 1.5$) and proximal ($R_{norm} < 1.5$) locations for all surfaces and on each surface

Surface	<i>All</i>		<i>Qf3</i>		<i>Qf5</i>		<i>Qf7</i>		
	<i>All</i>	<i>Distal</i>	<i>Proximal</i>	<i>Distal</i>	<i>Proximal</i>	<i>Distal</i>	<i>Proximal</i>	<i>Distal</i>	<i>Proximal</i>
<i>n</i>	125	65	60	18	17	24	21	23	22
Density	0.50 ^{***}	0.15	0.41 ^{**}	0.22	0.60 [*]	-0.03	0.39	0.42	0.62 ^{**}
Soil <i>Sg</i>	0.23 ^{**}	0.05	0.19	0.26	0.40	0.24	0.06	-0.06	0.12
<i>MPD</i>	-0.14	-0.13	0.19	-0.25	0.18	-0.27	0.31	-0.16	0.19
σ	0.30 ^{***}	-0.07	0.42 ^{***}	-0.09	0.57 [*]	-0.01	0.56 ^{**}	0.16	0.28
Gravel	0.05	-0.23	0.43 ^{***}	-0.29	0.37	-0.38	0.66 ^{**}	0.01	0.35
Sand	-0.35 ^{***}	0.05	-0.50 ^{***}	0.18	-0.63 ^{**}	0.02	-0.77 ^{***}	-0.26	-0.36
Silt	0.28 ^{**}	0.10	0.05	0.10	0.02	0.23	0.05	0.21	-0.08
Clay	0.34 ^{***}	0.10	0.26 [*]	0.16	0.39	0.33	0.32	0.07	0.13
Organic material	-0.29 ^{**}	-0.01	-0.38 ^{**}	-0.22	-0.71 ^{**}	0.19	-0.15	0.18	-0.76 ^{***}
K_s	-0.13	-0.01	-0.15	-0.20	-0.31	-0.15	-0.29	-0.09	0.01
α	-0.48 ^{***}	0.00	-0.27 [*]	0.15	-0.48 [*]	0.11	-0.13	-0.20	-0.18

* $p < 0.05$, ** $p < 0.01$, *** $p < 0.001$

Table 3-4. Spatial extent in normalized canopy radius of proximal ($R_{norm} < 1.5$) correlations with $p < 0.01$

Variable	<i>All</i>	<i>Qf3</i>	<i>Qf5</i>	<i>Qf7</i>
Density	1.61 ^{**}			1.66 ^{**}
σ	1.57 ^{***}		1.72 ^{**}	
Gravel	0.81 ^{***}		0.89 ^{**}	
Sand	1.38 ^{***}	1.68 ^{**}	1.39 ^{***}	
Organic material	1.32 ^{**}	1.29 ^{**}		1.36 ^{***}
Mean	1.34	1.49	1.33	1.51
STD	0.32	-	0.42	-
<i>n</i>	5	2	3	2

** $p < 0.01$, *** $p < 0.001$ reported in Table 3-3

Table 3-5. Pearson correlation coefficients between K_s and soil physical characteristics for all locations, distal ($R_{norm} > 1.5$) and proximal ($R_{norm} < 1.5$) locations for all surfaces and on each surface

Surface	<i>All</i>		<i>Qf3</i>		<i>Qf5</i>		<i>Qf7</i>		
	<i>All</i>	<i>Distal</i>	<i>Proximal</i>	<i>Distal</i>	<i>Proximal</i>	<i>Distal</i>	<i>Proximal</i>	<i>Distal</i>	<i>Proximal</i>
<i>n</i>	125	65	60	18	17	24	21	23	22
R_{norm}	-0.13	-0.01	-0.15	-0.20	-0.31	-0.15	-0.29	-0.09	0.01
Density	-0.05	-0.02	0.03	0.48	-0.24	0.15	-0.20	-0.38	-0.14
Soil <i>Sg</i>	-0.57 ^{***}	-0.68 ^{***}	-0.19	-0.69 ^{**}	-0.25	-0.60 ^{**}	-0.21	-0.46 [*]	-0.03
<i>MPD</i>	0.53 ^{***}	0.77 ^{***}	0.12	0.81 [*]	-0.48 [*]	0.62 ^{**}	0.14	0.75 ^{**}	-0.04
σ	-0.64 ^{***}	-0.67 ^{***}	-0.60 ^{***}	-0.37	-0.57 [*]	-0.76 ^{***}	-0.54 [*]	-0.69 ^{***}	-0.38
Gravel	-0.05	0.13	-0.31 [*]	0.73 ^{***}	-0.63 ^{**}	-0.05	-0.16	0.52 [*]	-0.07
Sand	0.63 ^{***}	0.67 ^{***}	0.60 ^{***}	0.43	0.69 ^{**}	0.79 ^{***}	0.44 [*]	0.42 [*]	0.10
Silt	-0.60 ^{***}	-0.69 ^{***}	-0.36 ^{**}	-0.77 ^{***}	0.34	-0.76 ^{***}	-0.33	-0.74 ^{***}	0.00
Clay	-0.58 ^{***}	-0.61 ^{***}	-0.48 ^{***}	-0.80 ^{***}	-0.06	-0.68 ^{***}	-0.45	-0.59 ^{**}	-0.26
Organic material	-0.40	-0.62 ^{***}	-0.24	-0.50 [*]	0.32	-0.76 ^{***}	-0.12	-0.28	0.30
α	0.67 ^{***}	0.76 ^{***}	0.74 ^{***}	0.76 ^{***}	0.73 ^{***}	0.79 ^{***}	0.44 [*]	0.79 ^{***}	0.86 ^{***}

* $p < 0.05$, ** $p < 0.01$, *** $p < 0.001$

3.6 Figures

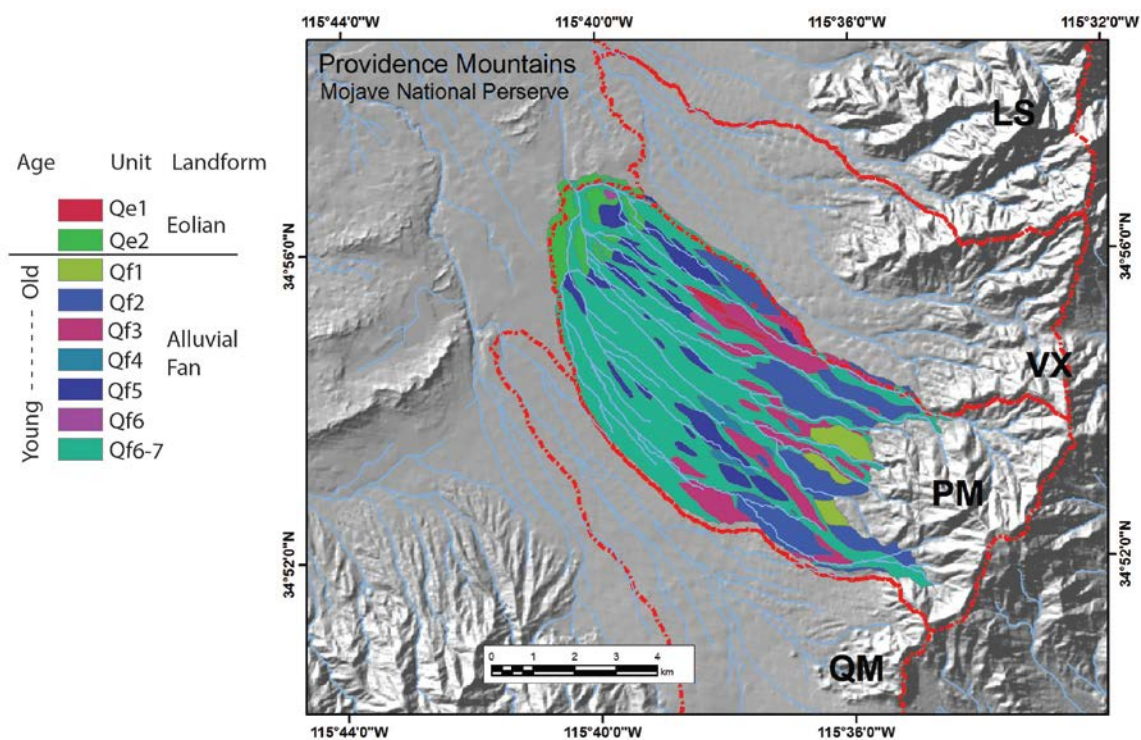


Figure 3-1. Geomorphic soil map of the Providence Mountain study area, in southeastern California, located on the mixed plutonic (PM) sequence. Watershed boundaries are indicated by the dashed lines. Three other lithologies including limestone (LS), mixed volcanics (VX) and quartz monzonite (QM) are also identified. Adapted from McDonald et al. (2003).

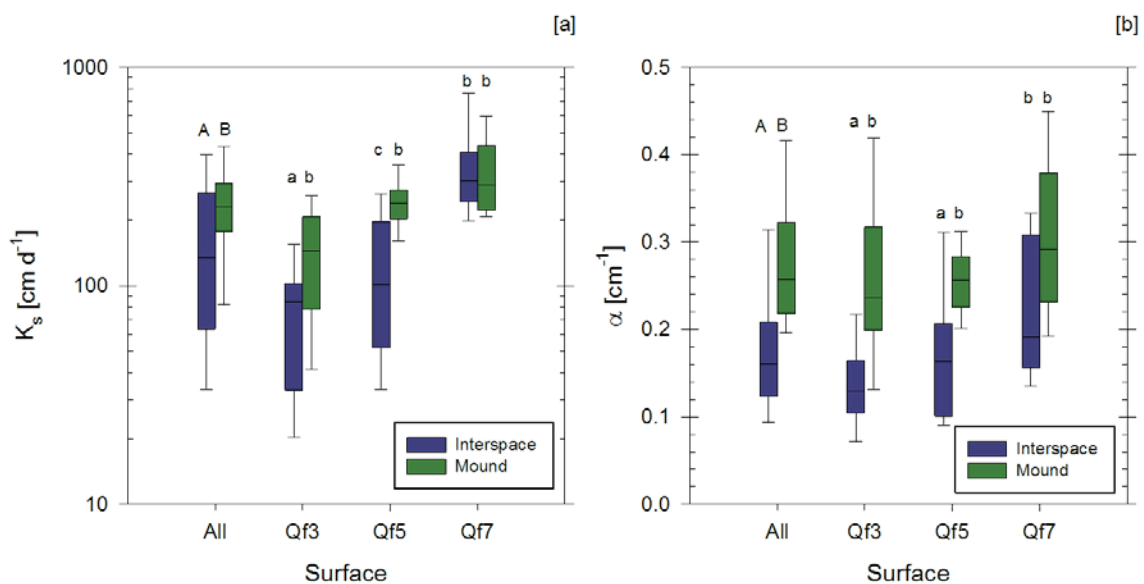


Figure 3-2. Box plots of [a] saturated hydraulic conductivity (K_s) and [b] the reciprocal of macroscopic capillary length (α) binned by interspace or mound microsite for all measurements and for each geomorphic surface from oldest (Qf3) to youngest (Qf7). The letters indicate significant ($p < 0.05$) groups from the post hoc (Sidak-Holms) t-tests.

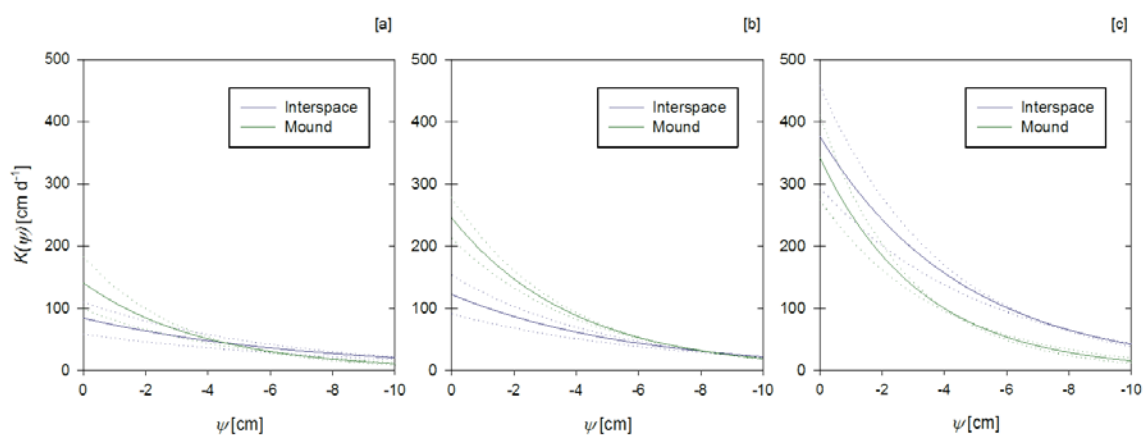


Figure 3-3. Hydraulic conductivity functions for soil water pressures from saturation (0 cm) to -10cm on [a] the oldest surface, Qf3, [b] the intermediate geomorphic surface, Qf5, and [c] the youngest surface, Qf7. Solid lines are the mean values and the corresponding dotted lines represent the 95% confidence intervals.

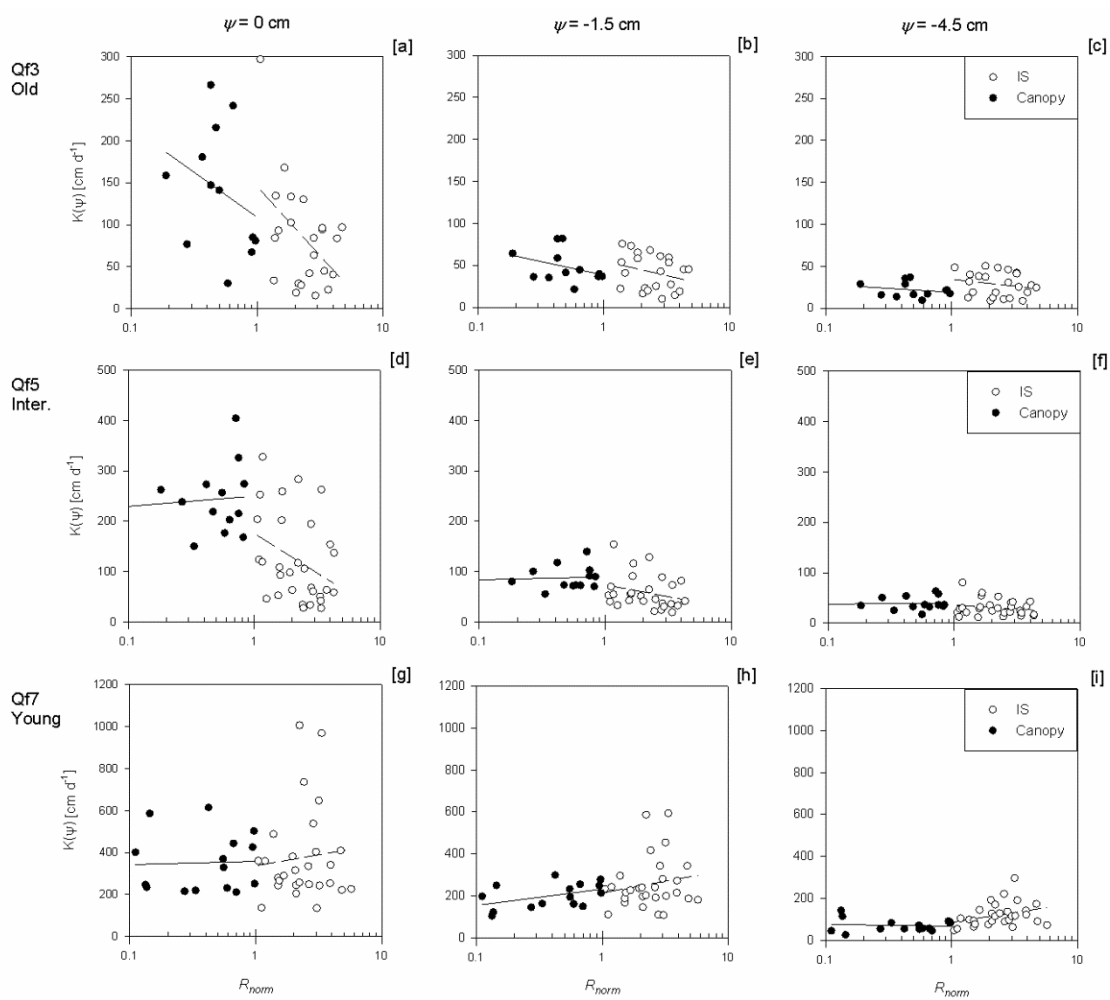


Figure 3-4. Hydraulic conductivity at canopy ($R_{norm} < 1$) and interspace (IS) microsites on the old Qf3 [a-c], the intermediate Qf5 [d-f] and young surface Qf7 [g-i] at saturation ($\psi = 0$ cm) and under tension of -1.5 and -4.5 cm. The lines indicate spatial trends and are only weakly significant ($p < 0.1$) at IS microsites on the Qf3 [a] and Qf5 [b].

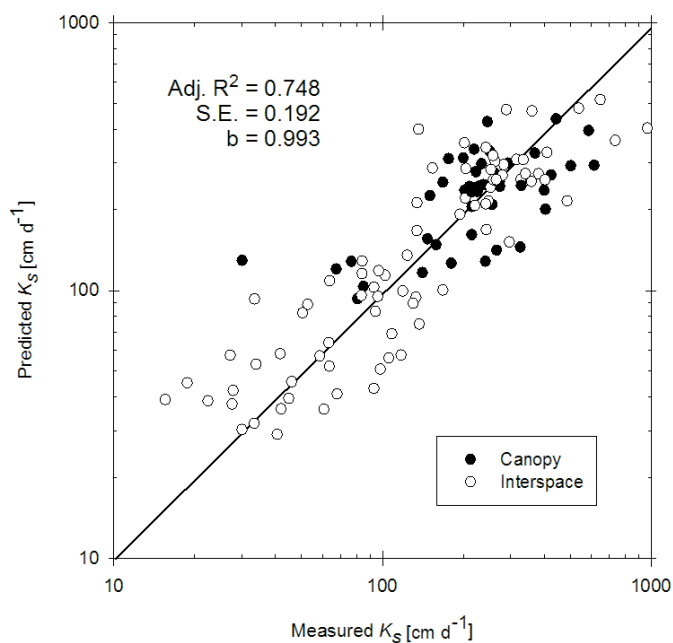


Figure 3-5. Predicted saturated conductivity (K_S) for all measurement locations using multiple linear regression and the independent variables soil structure grade, mean particle diameter, percent sand and organic matter.

3.7 Acknowledgments

We gratefully acknowledge support from the Army Research Office (W911NF-08-1-0453) and the National Science Foundation under NSF EPSCoR RING-TRUE III grant number EPS-447416.

3.8 References

- Ankeny, M. D., M. Ahmed, T. C. Kaspar, and R. Horton (1991), Simple field method for determining unsaturated hydraulic conductivity, *Soil Sci. Soc. Am. J.*, *55*, 467-470.
- Bedford, D. R., and E. E. Small (2008), Spatial patterns of ecohydrologic properties on a hillslope-alluvial fan transect, central New Mexico, *Catena*, *73*, 34-48.
- Ben-Dor, E., and A. Banin (1989), Determination of organic-matter content in arid-zone soils using a simple "loss-on-ignition" method, *Commun. Soil Sci. Plant Anal.*, *20*, 1675-1695.
- U.S. Department of Commerce (2004), Precipitation-frequency Atlas of the United States, Volume 1 version 4.0: Semiarid Southwest (Arizona, Southeast California, Nevada, New Mexico and Utah). *NOAA Atlas 14*, National Oceanic and Atmospheric Administration, Silver Spring, MD.
- Caldwell, T. G., E. V. McDonald, and M. H. Young (2006), Soil disturbance and hydrologic response at the National Training Center, Ft. Irwin, California, *J. Arid Environ.*, *67*, 456-472.
- Caldwell, T. G., M. H. Young, J. Zhu, and E. V. McDonald (2008), Spatial structure of hydraulic properties from canopy to interspace in the Mojave Desert, *Geophys. Res. Lett.*, *35*, L19406, doi, 10.1029/2008GL035095.
- Duan, Q. Y., S. Sorooshian, and V. Gupta (1992), Effective and efficient global optimization for conceptual rainfall-runoff models, *Water Resour. Res.*, *28*, 1015-1031.
- Duniway, M. C., K. A. Snyder, and J. E. Herrick (2010), Spatial and temporal patterns of water availability in a grass-shrub ecotone and implications for grassland recovery in arid environments, *Ecohydrology*, *3*, 55-67, 10.1002/eco.94.
- Dunkerley, D. L. (2000), Hydrologic effects of dryland shrubs: defining the spatial extent of modified soil water uptake rates at an Australian desert site, *J. Arid Environ.*, *45*, 159-172.
- Dunkerley, D. L. (2002), Infiltration rates and soil moisture in a groved mulga community near Alice Springs, arid central Australia: evidence for complex internal rainwater redistribution in a runoff-runon landscape, *J. Arid Environ.*, *51*, 199-219.
- Eagleson, P. S. (1978), Climate, soil, and vegetation, 1, Introduction to water balance dynamics, *Water Resour. Res.*, *14*, 705-712.
- Eckert, R. E., M. K. Wood, W. H. Blackburn, and F. F. Peterson (1979), Impacts of off-road vehicles on infiltration and sediment production of two desert soils, *J. Range Manage.*, *32*, 394-397.
- Gardner, W. R. (1958), Some steady-state solutions of the unsaturated moisture flow equation with application to evaporation from a water table, *Soil Sci.*, *85*, 228-232.
- Gee, G. W., and D. Or (2002), Particle-size analysis, in *Methods of Soil Analysis, Part 4. Physical Methods*, edited by J. H. Dane and G. C. Topp, pp. 255-293, Soil Science Society of America Book Series, Madison.

- Hamerlynck, E. P., J. R. McAuliffe, and S. D. Smith (2000), Effects of surface and sub-surface soil horizons on the seasonal performance of *Larrea tridentata* (creosotebush), *Functional Ecology*, *14*, 596-606.
- Hamerlynck, E. P., J. R. McAuliffe, E. V. McDonald, and S. D. Smith (2002), Ecological responses of two Mojave Desert shrubs to soil horizon development and soil water dynamics, *Ecology*, *83*, 768-779.
- Harden, J. W. (1982), A quantitative index of soil development from field descriptions: examples from a chronosequence in central California, *Geoderma*, *28*, 1-28.
- Jenny, H. (1941), *Factors of Soil Formation: a system of quantitative pedology*, 191 pp., McGraw-Hill, New York.
- Kurc, S. A., and E. E. Small (2004), Dynamics of evapotranspiration in semiarid grassland and shrubland ecosystems during the summer monsoon season, central New Mexico, *Water Resour. Res.*, *40*, W09305, doi:10.1029/2004WR003068.
- Lebron, I., M. D. Madsen, D. G. Chandler, D. A. Robinson, O. Wendroth, and J. Belnap (2007), Ecohydrological controls on soil moisture and hydraulic conductivity within a pinyon-juniper woodland, *Water Resour. Res.*, *43*, W08422, doi:10.1029/2006WR005398.
- Lide, D. R. (2001), *Handbook of chemistry and physics*, 82 ed., CRC Press, Boca Raton, FL.
- Logsdon, S. D., and D. B. Jaynes (1993), Methodology for determining hydraulic conductivity with tension infiltrometers, *Soil Sci. Soc. Am. J.*, *57*, 1426-1431.
- Loizeau, J. L., D. Arbouille, S. Santiago, and J. P. Vernet (1994), Evaluation of a wide-range laser diffraction grain-size analyzer for use with sediments, *Sedimentology*, *41*, 353-361.
- Lyford, F. P., and H. K. Qashu (1969), Infiltration rates as affected by desert vegetation, *Water Resour. Res.*, *5*, 1373-1376.
- Madsen, M. D., D. G. Chandler, and J. Belnap (2008), Spatial gradients in ecohydrologic properties within a pinyon-juniper ecosystem, *Ecohydrology*, *1*, 349-360, 10.1002/eco.29.
- McAuliffe, J. R., and E. V. McDonald (2006), Holocene environmental change and vegetation contraction in the Sonoran Desert, *Quaternary Res.*, *65*, 204-215.
- McAuliffe, J. R., E. P. Hamerlynck, and M. C. Eppes (2007), Landscape dynamics fostering the development and persistence of long-lived creosotebush (*Larrea tridentata*) clones in the Mojave Desert, *J. Arid Environ.*, *69*, 96-126.
- McDonald, E. V., L. D. McFadden, and S. G. Wells (2003), Regional response of alluvial fans to the Pleistocene-Holocene climatic transition, Mojave Desert, California, in *Paleoenvironments and Paleohydrology of the Mojave and southern Great Basin Deserts*, edited by Y. Enzel, S. G. Wells and N. Lancaster, pp. 189-205, Geological Society of America Special Paper 368., Boulder, CO.
- McDonald, E. V., F. B. Pierson, G. N. Flerchinger, and L. D. McFadden (1996), Application of a soil-water balance model to evaluate the influence of Holocene climate change on calcic soils, Mojave Desert, California, USA, *Geoderma*, *74*, 167-192.

- McFadden, L. D., S. G. Wells, and M. J. Jercinovich (1987), Influences of eolian and pedogenic processes on the origin and evolution of desert pavements, *Geology*, *15*, 504-508.
- McFadden, L. D., E. V. McDonald, S. G. Wells, K. Anderson, J. Quade, and S. L. Forman (1998), The vesicular layer and carbonate collars of desert soils and pavements: formation, age and relation to climate change, *Geomorphology*, *24*, 101-145.
- Meadows, D. G., M. H. Young, and E. V. McDonald (2005), A laboratory method for determining the unsaturated hydraulic properties of soil peds, *Soil Sci. Soc. Am. J.*, *69*, 807-815.
- Meadows, D. G., M. H. Young, and E. V. McDonald (2006), Estimating the fine soil fraction of desert pavements using ground penetrating radar, *Vadose Zone J.*, *5*, 720-730.
- Meadows, D. G., M. H. Young, and E. V. McDonald (2008), Influence of relative surface age on hydraulic properties and infiltration on soils associated with desert pavements, *Catena*, *72*, 169-178.
- Moran, M. S., et al. (2010), Hydrologic response to precipitation pulses under and between shrubs in the Chihuahuan Desert, Arizona, *Water Resour. Res.*, *46*, W10509, doi 10.1029/2009WR008842.
- Nimmo, J. R. (1997), Modeling structural influences on soil water retention, *Soil Sci. Soc. Am. J.*, *61*, 712-719.
- Nimmo, J. R., K. M. Schmidt, K. S. Perkins, and J. D. Stock (2009a), Rapid Measurement of Field-Saturated Hydraulic Conductivity for Areal Characterization, *Vadose Zone J.*, *8*, 142-149, 10.2136/vzj2007.0159.
- Nimmo, J. R., K. S. Perkins, K. M. Schmidt, D. M. Miller, J. D. Stock, and K. Singha (2009b), Hydrologic characterization of desert soils with varying degrees of pedogenesis: 1. Field experiments evaluating plant-relevant soil water behavior, *Vadose Zone J.*, *8*, 480-495, 10.2136/vzj2008.0052.
- Noy-Meir, I. (1973), Desert ecosystems: Environment and producers, *Annu. Rev. Ecol. Syst.*, *4*, 25-51.
- Quade, J. (2001), Desert pavements and associated rock varnish in the Mojave Desert: How old can they be?, *Geology*, *29*, 855-858.
- Ravi, S., P. D'Odorico, and G. S. Okin (2007), Hydrologic and aeolian controls on vegetation patterns in arid landscapes, *Geophys. Res. Lett.*, *34*, L24S23, doi:10.1029/2007GL031023.
- Redmond, K. T. (2009), Historical climate variability in the Mojave Desert, in *The Mojave Desert: Ecosystem Processes and Sustainability*, edited by R. H. Webb, L. F. Fenstermaker, J. S. Heaton, D. L. Hughson, E. V. McDonald and D. M. Miller, pp. 11-30, University of Nevada Press, Reno, NV.
- Reheis, M. C., and R. Kihl (1995), Dust Deposition In Southern Nevada And California, 1984-1989 - Relations To Climate, Source Area, And Source Lithology, *J. Geophys. Res - Atmos.*, *100*, 8893-8918.
- Rodriguez-Iturbe, I., P. D'Odorico, A. Porporato, and L. Ridolfi (1999), On the spatial and temporal links between vegetation, climate, and soil moisture, *Water Resour. Res.*, *35*, 3709-3722.
- Scanlon, B. R., D. G. Levitt, R. C. Reedy, K. E. Keese, and M. J. Sully (2005), Ecological controls on water-cycle response to climate variability in deserts, *Proc. Natl. Acad. Sci. USA*, *102*, 6033-6038.

- Schlesinger, W. H., J. A. Raikes, A. E. Hartley, and A. E. Cross (1996), On the spatial pattern of soil nutrients in desert ecosystems, *Ecology*, 77, 364-374.
- Seyfried, M. S., and B. P. Wilcox (1995), Scale and the Nature of Spatial Variability - Field Examples Having Implications for Hydrologic Modeling, *Water Resour. Res.*, 31, 173-184.
- Shafer, D. S., M. H. Young, S. F. Zitzer, T. G. Caldwell, and E. V. McDonald (2007), Impacts of interrelated biotic and abiotic processes during the past 125 000 years of landscape evolution in the Northern Mojave Desert, Nevada, USA, *J. Arid Environ.*, 69, 633-657.
- Shiozawa, S., and G. S. Campbell (1991), On the calculation of mean particle diameter and standard-deviation from sand, silt, and clay fractions, *Soil Sci.*, 152, 427-431.
- Stevenson, B. A., E. V. McDonald, and T. G. Caldwell (2009), Root patterns for *Larrea tridentata* in relation to soil morphology in Mojave Desert soils of different ages, in *The Mojave Desert: Ecosystem Processes and Sustainability*, edited by R. H. Webb, L. F. Fenstermaker, J. S. Heaton, D. L. Hughson, E. V. McDonald and D. M. Miller, pp. 312-338, University of Nevada Press, Reno, NV.
- Turk, J. K., and R. C. Graham (2011), Distribution and Properties of Vesicular Horizons in the Western United States, *Soil Sci. Soc. Am. J.*, 75, 1449-1461, 10.2136/sssaj2010.0445.
- Schoeneberger, P.J., D.A. Wysocki, E.C. Benham, and W.D. Broderson (2002), Field Book for Describing and Sampling Soils, Version 2.0, Natural Resources Conservation Service, National Soil Survey Center, Lincoln, NE.
- Wooding, R. A. (1968), Steady infiltration from a large shallow circular pond, *Water Resour. Res.*, 4, 1259-1273.
- Yaalon, D. H., and E. Ganor (1973), The influence of dust on soils in the Quaternary, *Soil Sci.*, 116, 146-155.
- Yin, J. (2008), Spatiotemporal variation in soil moisture and hydraulic properties and their impacts on rainfall-runoff and infiltration processes, 132 pp, University of Nevada, Las Vegas, Las Vegas.
- Young, M. H., T. G. Caldwell, D. G. Meadows, and L. F. Fenstermaker (2009), Variability of soil physical and hydraulic properties at the Mojave Global Change Facility, Nevada: Implications for water budget and evapotranspiration *J. Arid Environ.*, 73, 733-744.
- Young, M. H., E. V. McDonald, T. G. Caldwell, S. G. Benner, and D. G. Meadows (2004), Hydraulic properties of a desert soil chronosequence in the Mojave Desert, USA, *Vadose Zone J.*, 3, 956-963.

4 INVERSE MODELING OF NEAR-SURFACE VADOSE ZONE PROPERTIES IN DESERT SOILS USING MULTIOBJECTIVE PARAMETER OPTIMIZATION

Caldwell, Todd G.^{1*}, Thomas Wöhling², Michael H. Young³, Douglas P. Boyle⁴, and Eric V. McDonald¹

¹Desert Research Institute, Division of Earth and Ecosystem Sciences, Reno, Nevada, USA.

²Water and Earth Science Systems Research Centre, Department of Geosciences, University of Tübingen, Tübingen, Germany.

³Bureau of Economic Geology, University of Texas at Austin, Austin, TX, USA.

⁴Department of Geography, University of Nevada, Reno, USA.

For submission to the Vadose Zone Journal

December 2011

* Corresponding author, E-mail: todd.caldwell@dri.edu; Tel.: +1 (775) 673-7368

ABSTRACT

The near-surface soil moisture dynamics of arid vadose zones are critical to the partitioning of precipitation between infiltration, runoff and evapotranspiration. Modeling soil moisture on coarse textured alluvial soils under high evaporative demand and infrequent rainfall challenges both characterization and numerical methods. For this study, three young alluvial soils in the central Mojave Desert were inversely modeled using HYDRUS and the AMALGAM algorithm. Observations of soil water content (θ) and matric head (ψ) were used to formulate our multiobjective framework, simultaneously minimizing both residuals. Sensitivity analysis found the dry-end parameters most sensitive but often conflicting between the two criteria while soil temperature was effectively modeled but insensitive. A dynamic range of ψ (1-400 m) was coupled to a relatively small range of θ that seldom exceeded $0.10 \text{ m}^3 \text{ m}^{-3}$ limiting our ability to resolve wet-end parameters. Pareto-analysis determined the model structure inadequacies between fitting both criteria and also revealed bifurcated into populations favoring either θ or ψ error minimization. Direct parameterization from infiltrometer data, and indirect pedotransfer functions had good agreement with θ but ψ remained moist due to the inability of coarse textures to move moisture to the surface.

Index terms: heat dissipation sensor, permeameter, Ft. Irwin, National Training Center

4.1 Introduction

Deserts are a heterogeneous mix of soil, sediment, and rock with interspersed, shallow rooted but highly adapted vegetation. Low mean annual precipitation and high evaporative demand result in arid soils being net sinks for both dust and solutes [McFadden *et al.*, 1987]. Young alluvial soils lack development and tend to be gravel-rich and sandy; while older soils maintain distinct horizonation, petrocalcic and argillic layers [McDonald *et al.*, 2003; Stevenson *et al.*, 2009]. Studies have shown that the age and physical character of soils common to Mojave Desert bajadas exert a strong control on soil water flux [McDonald *et al.*, 1996; Young *et al.*, 2004; Nimmo *et al.*, 2009; Caldwell *et al.*, in review]. Moreover, the growth and establishment of desert plants is largely limited by the availability of soil moisture [Noy-Meir, 1973].

Numerical modeling has proven to be a valuable tool to evaluate deep arid vadose zone processes such as recharge and paleoflux [Scanlon and Milly, 1994; Andraski, 1997; Yin *et al.*, 2008]. Most near surface modeling has focused primarily on more stochastic models of ecohydrology [Eagleson, 1978; Rodriguez-Iturbe *et al.*, 1999; Porporato *et al.*, 2002]. Parameterization of any model requires either direct measurements of soil hydraulic properties or indirect inference of these properties from more readily available data. The former is often cost prohibitive and requires significant field and laboratory work due to the heterogeneous nature of soils [Nielsen *et al.*, 1973; Hendrickx *et al.*, 1990] and the scale dependence of the measurements [Vogel and Roth, 2003]. The latter uses more generalized data to infer properties, often through pedotransfer functions (PTF) [Rawls *et al.*, 1982; Tietje and Tapkenhinrichs, 1993; Wosten *et al.*, 2001] generally

based on soil texture, bulk density, and some level of soil structure when available [Meadows *et al.*, 2006]. Verifying or bench-marking any numerical simulation, regardless of its parameterization, relies on the interpretation of both effective model parameters and the respective ‘fit’ to observed data [Kirchner, 2006].

Parameter optimization (or inverse modeling) allows model parameters to be adjusted iteratively to achieve an optimum fit to observational data, using a specified search algorithm and a numerical goodness-of-fit criterion defined by an objective function. Optimizing multiple parameters (or multiple criteria), n , results in a $n-1$ dimensional parameter (and objective) surface. Navigating these complex surfaces with gradient-based approach or a single algorithm can prove ineffective [Wolpert and Macready, 1997]. Global optimization algorithms use multiple concurrent starting points and multiple parameter complexes that explore entire defined parameter and objective spaces. Such algorithms may include the formulation of either a complex single objective [Duan *et al.*, 1992] or a multiple objective function [Vrugt and Robinson, 2007; Vrugt *et al.*, 2009]. Hybrid genetic algorithms, such as used in this study, combine local and global heuristic searches to consistently update and shuffle populations between different algorithms specific to the applied optimization problem and response surface. The non-dominated Pareto solutions further allow the modeler to examine this tradeoff between multiple objective measures, and assess deficiencies in both model structure and data information.

Inverse modeling of vadose properties has been successfully applied to numerous, well-controlled laboratory and field-scale studies [see review by Vrugt *et al.* (2008)] often using gradient-based techniques. Studies have applied inverse modeling under

transient atmospheric boundary conditions at the field scale to obtain effective hydraulic parameters [*Dane and Hruska, 1983; Jacques et al., 2002; Mertens et al., 2006; Kampf and Burges, 2007*] using a single or quasi-multiple objective function; fewer have used multiobjective optimization [*Wöhling et al., 2008; Wöhling and Vrugt, 2011*] and fewer yet have applied optimization techniques to arid soil systems [*Scott et al., 2000; Mirus et al., 2009*] where water content dynamics are small while soil-water potentials can vary over many orders of magnitude [*Andraski, 1997*].

Arid soil systems undergoing active restoration in the Mojave Desert have had limited success, in part because enhanced soil microclimate conditions dissipated very quickly following irrigation [*Caldwell et al., 2009*]. The essential objective of any arid lands revegetation programs is to establish optimum germination and growing conditions for vegetation, especially with regard to the timing and abundance of available water. Modeling has been used to support arid land restoration [*McDonald, 2002*] but without comparison to observed data.

The goal of this study is to use multiobjective parameter optimization and observations of soil-water content (θ), soil-water potential (ψ), and soil temperature (T) on three coarse-textured (sand, loamy sand and sandy loam) bare alluvial soils in the Mojave Desert undergoing active restoration [*Caldwell et al., 2009*] and to better assess the required level of model parameterization for land management applications. Using the HYDRUS-1D model [*Simunek et al., 2009*], we define the sensitivity of hydraulic parameters in arid soil systems, determine the effective parameters through multiobjective inverse modeling, and assess model performance using simpler direct and indirect hydraulic characterization schemes. Additionally, we investigate parameter quality and

vertical heterogeneity through Pareto analyses. Results of this study can be used to aid our understanding of the complexity of modeling arid systems for water resource and ecosystem management and ultimately guide land managers to effective restoration activities on arid alluvial soils.

4.2 Materials and Methods

4.2.1 Site Description and Field Characterization

Three sites, Langford Impact Zone (*LIZ*), John Wayne Hill (*JWH*) and Bicycle Lake (*BLK*), covering a range of coarse-grained soil textures, were selected for field characterization, monitoring, and model simulation. The sites are located at the National Training Center, Ft. Irwin, CA in the central Mojave Desert with an annual precipitation of 99 mm and an average air temperature of 18°C. This study was part of a larger effort to evaluate restoration of arid lands from seed using sprinkler irrigation to stimulate germination. It consisted of two trials; Trial 1 at the *LIZ* and *JWH* sites and Trial 2 at *BLK*. The seedbed microclimate under the various surface treatments was presented in *Caldwell et al.* [2009] and the seeding trials data were presented in *Ostler and Hanson* [2003]. All sites were disturbed by vehicles involved in military training. Little natural vegetation was remaining. Both trials consisted of a variety of surface treatments; for simplicity, only the irrigated bare soil plot at each site is presented. Both sites in Trial 1, initiated in the spring of 2001, were seeded and irrigated with 2-4 cm of water and monitored through June 2002. Trial 2 (*BLK*) was seeded in April 2003, irrigated in May and again in September 2003, and monitored through June 2004. Trial 2 used a more robust monitoring system and more replicated field characterization. Seed germination

was very low and no vegetation was established during either trial. For our purposes, the irrigation provided moisture dynamics on a bare soil that otherwise would have been predominantly dry over the course of the study, providing very little information on soil moisture dynamics.

Trenches were excavated to 80-100 cm depth and soil samples were collected from each horizon for laboratory analysis. Soil morphology was described according to the standard methods and nomenclature of the *Soil Survey Staff* [2003]. Representative bulk soil samples were collected from each horizon and analyzed in the laboratory for particle-size distribution [Gee and Or, 2002], electrical conductivity [Rhoades, 1996], and total bulk density (BD_T) [Grossman and Reinsch, 2002].

4.2.2 Observational Data from Microclimate Stations

Soil microclimate monitoring stations were installed at each excavated soil trench following sample collection. Sensors were installed horizontally approximately 25 cm into the vertical trench face. Each subplot was monitored for volumetric soil moisture (θ , $\text{m}^3 \text{m}^{-3}$), soil matric potential (ψ_t , kPa) and soil temperature (T , degrees C) using data acquisition systems (CR10X, Campbell Scientific, Inc., Logan UT). Volumetric soil moisture was measured using low-frequency water content reflectometers (model CS-615, Campbell Scientific, Inc.). Soil matric potential and T were monitored using heat dissipation sensors (*HDS*) (model CS-229, Campbell Scientific, Inc.), which measure thermal conductivity within a ceramic plug. Both sensors were collocated at four depths (3-, 10-, 25- and 55- cm) in each of four subplots for Trial 1 and 2. The greatest depth was 45-cm in Trial 2.

Laboratory calibration of the reflectometers showed that the factory coefficients for high conductivity soil were sufficient for the three soils tested with minor adjustments to the intercept. All HDS were laboratory calibrated [Reece, 1996] with soil over a calibrated range of $0.02 < \psi_t < 1.50$ MPa. The *in situ* matric potential values were converted to absolute values of matric head $|\psi|$; the equivalent to HYDRUS model output by

$$\psi = \frac{-\psi_t}{\rho_w g} \quad [1]$$

where ψ is 0 m at saturation and increasingly positive at greater suction, ρ_w is the temperature (measured at each depth) corrected density of water (kg m^{-3}), and g is the gravitational constant (m s^{-2}).

4.2.3 Meteorological Data and Potential Evapotranspiration

Reference evapotranspiration (ET_o), the upper boundary condition in the model, was calculated using data from the California Irrigation Management Information System (CIMIS) (www.cimis.water.ca.gov/). The data are quality controlled [Meek and Hatfield, 1994] and were additionally validated for clear sky irradiance using Allen [2008b]. Data from Station 134, Barstow NE located roughly 45 km south from 2001-2004 was used for all meteorological calculations including both ET_o and the energy balance. For the 4 year study period, <0.1% of the hourly data were missing which was gap filled by linear interpolation. Corrected data were used to calculate the ASCE grass reference ET_o [ASCE-EWRI, 2005] using REF-ET, V3.1 [Allen, 2008a]. The calculated ET_o was used for the maximum upper boundary flux condition in HYDRUS (described below). The additional meteorological data (air T , relative humidity, incoming short-wave radiation,

and wind speed) were used for energy balance calculations in HYDRUS to determine temperature flux at the upper and lower boundaries.

4.2.4 Direct Measurements of Hydraulic Properties

We present a combination of direct and indirect estimation of effective hydraulic properties for use in forward modeling. The closed-form model of soil-water retention and unsaturated flow of van Genuchten [1980] and the theoretical pore-size distribution model of Mualem [1976] were used throughout this study. Water retention has the form

$$\theta_e(\psi) = \frac{\theta(\psi) - \theta_r}{\theta_s - \theta_r} = \frac{1}{(1 + |\alpha\psi|^n)^m} \quad \psi < 0 \quad [2]$$

and the unsaturated hydraulic conductivity function is defined as

$$K(\theta) = K_s \theta_e^l \left[1 - \left(1 - \theta_e^{1/m} \right)^m \right]^2 \quad \psi < 0 \quad [3]$$

where θ_e is the effective volumetric water content, θ_s is the saturated water content, θ_r is the residual water content, n is an empirical measure of pore-size distribution, $m = 1 - 1/n$, α is related to the inverse of air-entry pressure (cm^{-1}), K_s is the saturated hydraulic conductivity (cm d^{-1}), and l related to both pore tortuosity and connectivity. The value of l is commonly assumed to be 0.5, retaining physical meaning or considered an empirical coefficient to maximize fit to data [Schaap and Leij, 2000].

Soil hydraulic properties were directly measured using replicated tension disc infiltrometers [Perroux and White, 1988] at each site. Tension infiltration was conducted at 4 incremental soil water heads ($h = -12, -5, -2$ and -0.5 cm). Cumulative outflow was monitored using a differential pressure transducer [Casey and Derby, 2002] at 15-second time intervals. Hydraulic properties were obtained through both an analytical solution

[Logsdon and Jaynes, 1993; Caldwell *et al.*, 2008] and numerical inversion of the cumulative outflow data ($\text{cm}^{-3} \text{s}^{-1}$) using the axisymmetric, finite-element code HYDRUS-2D and the initial and final measured water contents [Simunek *et al.*, 1998; Young *et al.*, 2004]. For Trial 1, a single multiple tension infiltration test was conducted along with four additional tests at -0.5 cm at the bare soil plot. Trial 2 had three replicated, incremental pressure infiltrometer tests at each of four experimental plots.

We also combined *in situ* observations of soil water retention from sensors with infiltrometer outflow data. Observed data derived at hourly time steps were log transformed, sorted, and binned according to soil-water potential. The values obtained during the infiltrometer tests for θ_s and $K(h)$ for each tension and the reduced sensor data were fit to equation [2] and [3] simultaneously using the RETC code [Van Genuchten *et al.*, 1990].

4.2.5 Indirect Estimates of Hydraulic Properties

Pedotransfer functions (*PTF*) estimate hydraulic properties from relatively simple-to-obtain measurements, such as soil texture and bulk density (Arya and Paris, 1981; Arya *et al.*, 1999) and have been used for a variety of field scenarios dealing with infiltration and water movement [Rawls *et al.*, 1989; Parasuraman *et al.*, 2006; Young *et al.*, 2009]. The Rosetta Model (Version 2.0) [Schaap *et al.*, 2001] was used in this study with soil class (*i.e.*, silt loam, loamy sand, hereafter known as I_1) and a more robust data set that contains detailed particle size distributions and bulk density (hereafter known as I_2). Measured total bulk density (BD_T) was corrected for gravel fraction (g_r), yielding fine-earth (FE) bulk density (BD_{FE}), using the method of Andraski [1991]:

$$v_g = BD_T \left(\frac{g_r}{\rho_g} \right) \quad [4]$$

where ρ_g is the particle density of the gravel, assumed to be 2.65 g cm^{-3} . The BD_{FE} is corrected by:

$$BD_{FE} = BD_T \left(\frac{1-g_r}{1-v_g} \right) \quad [5]$$

where v_g is the volume ratio of gravel. The fine-earth textural components and the BD_{FE} are input into Rosetta to obtain hydraulic properties of the matrix [Young *et al.*, 2009].

The resulting *PTF* estimates of soil properties were scaled by the gravel content according to the model of Brakensiek *et al.* [1986]:

$$\theta_s \text{ (or } \theta_r) = \theta_{sb} \text{ (or } \theta_{rb}) (1-g_r) \quad [6]$$

$$K_s = K_{sb}(1-g_r) \quad [7]$$

where θ_s and θ_r ($\text{m}^3 \text{ m}^{-3}$) are the scaled saturated and residual water contents, respectively; subscript *b* indicates estimates taken directly from Rosetta; K_s is the scaled saturated hydraulic conductivity (cm d^{-1}). This method (*I*₃) and a general summary are presented in Table 4-1.

4.3 Inverse Modeling and Multiobjective Parameter Optimization

4.3.1 Regional Sensitivity Analysis

Regional sensitivity analysis (*RSA*) was performed to better assess parameter bounds and sensitivities, numerical convergence issues, and normalization of the multiobjective performance criteria. The multiple criteria obtained from the *RSA* provide critical information on the sensitivity of each parameter on model performance [Freer *et al.*, 1996; Mertens *et al.*, 2005]. A uniform random sample of the parameter space (Table

4-2) was used in forward simulations of a single layer (0 – 100 cm) soil under the representative boundary conditions at each site. A set of 20,000 Monte Carlo simulations was used to assess the performance and convergence criteria of the model. By ranking parameter suites according to each performance criterion, an assessment of the influential (sensitive) parameters can be determined from the *posterior* distribution of good versus poor performing models (e.g., *Spear and Hornberger, 1980*) and unnecessary or unrealistic parameter space can be removed before implementing the global search optimization.

4.3.2 Multiobjective Framework and Performance Criteria

A multiobjective framework avoids subjectivity and information loss in minimization of a singular scalar criterion by the simultaneous minimization of multiple functions. The key characteristic of the multiobjective problem is that the optimization does not consider a single criterion because the performance of the other criteria will suffer. The multiobjective problem can be stated as such [*Madsen, 2000*]

$$\min\{F_1(\phi), F_2(\phi), \dots, F_i(\phi)\} \text{ and } \phi \in \Phi \quad [12]$$

where the objective measures (F_1 through F_i) are scalars of residuals, each containing a vector of model parameters (ϕ) within the feasible space (Φ). The Pareto-optimum solutions are determined sequentially as the subpopulation (s) of ϕ containing the minimal values of F_j whereby no other solution provides lower values across the i -dimensional objective space. The Pareto set of solutions represent the non-dominated parameter sets within the entire feasible parameter space [*Gupta et al., 1998*]. The Pareto-extreme values represent ϕ with the minimal value found for each F . The final population

of parameters effectively minimizes each criterion and represents a incommensurable tradeoff (i.e., Pareto solutions); as such, each parameter set represents an equally ‘valid’ solution with concession between criteria.

A measure of model performance or error is needed to assess parameter sensitivities in the *RSA* and for minimization in inverse modeling (next section). Observations of both θ and ψ were used in the multiobjective framework. The performance criteria used here are the root-mean square error (*RMSE*):

$$RMSE = \left[\frac{1}{N} \sum_{i=1}^N (S_i - O_i)^2 \right]^{1/2} \quad [13]$$

and the mean bias error (*MBE*)

$$MBE = \frac{1}{N} \sum_{i=1}^N (S_i - O_i) \quad [14]$$

where S_i and O_i are the simulated and observed values at i hourly time step, and N is the total number of observations. To allow greater sensitivity to the infrequent and lower absolute values of ψ during wetting events, this data was log-transformed before calculating its *RMSE* herein represented by $\log(RMSE_\psi)$. The *RMSE* for θ and ψ minimized in the inverse modeling contained concatenated data from all four sensors at 3-, 10- and 25-, 45 or 55cm depths. The *RMSE* and *MBE* for θ , ψ , and soil T for each resulting Pareto solution following the inverse modeling was calculated at each observation node.

4.3.3 Parameter Optimization Algorithm

The global, multiobjective parameter optimization algorithm used in this study, AMALGAM (A Multi-ALgorithm, Genetically Adaptive Multi-objective) [Vrugt and

Robinson, 2007], combines two concepts: simultaneous multi-method search, and self-adaptive offspring creation. The multi-method uses four search strategies simultaneously including the Nondominated Sorting Genetic Algorithm, Particle Swarm Optimization, Adaptive Metropolis Search, and Differential Evolution, and adaptively updates the weights of these individual algorithms based on their reproductive success.

The AMALGAM algorithm was used to optimize three multiobjective problems of increasing vertical heterogeneity (Table 4-1). These problems are defined as such: a single material from 0-100cm (L_1) with soil properties, a two-material soil with a horizon break at 10-cm (L_2), and three-material soil with an additional horizon as noted in the soil characterization (L_3). Performance criteria were scaled to better visualize the Pareto front distribution and obtain the Pareto compromise between the various Pareto solutions. The scaling of each objective function is given by

$$g(RMSE_i) = \frac{RMSE_i}{\sigma_i} + A_i, i = 1, 2 \quad [15]$$

where σ_i is the standard deviation of all successful Monte Carlo simulations performed during the *RSA* for each *i*th and A_i is a normalization constant between each:

$$A_i = \max \left[\min \left(\frac{RMSE_j}{\sigma_j} \right), j = 1, 2 \right] - \min \left(\frac{RMSE_i}{\sigma_i} \right) \quad [16]$$

This normalization results allows the Euclidean distances for each Pareto solution to be obtained; the smallest Euclidean distance is ultimately the Pareto compromise solution. Optimizations and *RSA* were conducted in a 64-bit, parallel MATLAB (vR2011b) environment that builds the input file for each iteration, executes the model in parallel, analyzes the output, and determines the next step. We found a stable Pareto-front

occurring after 10,000-20,000 simulations; however, we continued the optimizations to 20,000, 40,000, and 60,000 iterations for the L_1 , L_2 , and L_3 scenarios, respectively.

4.4 Results – Field Characterization

4.4.1 Soil Characterization

Mean soil particle size distribution for *LIZ*, *JWH* and *BLK* varied from sand (90% sand) to loamy sand (86% sand) to sandy loam (80% sand), respectively (Table 4-3). The upper 9 to 33 cm of all three sites was disturbed by military activities. These horizons were denoted by Ap (p for plowed or disturbed) genetic horizon designations. The disturbed soil structure was either single grain or massive to platy. Genetic horizons underlying Ap horizons ranged from poorly developed Ck horizons, to either Bw or weakly developed Bt horizons. Distinct horizon breaks were noted for the *LIZ* soil at 33 cm and *BLK* soil at 28 cm. No distinct textural break was observed or measured at *JWH*.

Mean gravel content ranged from 13.7 to 41.5% with the higher values generally found at *BLK* (Table 4-3). Bulk density ranged from 1.57 to 1.81 g cm⁻³, indicating these gravely soils were not extremely compacted, despite being disturbed and devoid of vegetation. Bulk electrical conductivities indicated salinity increases with depth, ranging from 0.35 to 0.75 dS m⁻¹ in the surface horizons ranging from 1.44 to 3.61 dS m⁻¹ in lower horizons. These lower depths required an adjustment in the calibration intercepts of the reflectometer probes. These 3 sites are very typical of poorly-developed, geomorphically young (Holocene) alluvial soils common to the National Training Center, Ft. Irwin, CA [*Caldwell et al.*, 2006; *Stevenson et al.*, 2009].

4.4.2 Direct Measurements of Hydraulic Properties

Direct measurements of hydraulic properties at ground surface and 10-cm depth were obtained through numerical inversion of tension infiltrometer data and analytical solutions. Gravel content at *BLK* was evident in the lower θ_s ($0.25 \text{ m}^3 \text{ m}^{-3}$) than the surfaces at both *LIZ* and *JWH* (Table 4-4). The mean saturated hydraulic conductivity ($K_s \pm$ one standard deviation) was highest on the surface at the sand-textured *LIZ* site ($439 \pm 147 \text{ cm d}^{-1}$), and lowest on the sandy loam soil at *BLK* ($92.5 \pm 49.8 \text{ cm d}^{-1}$) with the loamy sand soil at *JWH* appearing similar to *LIZ*. The 95% confidence intervals (*CI*) presented will be used later for parameter constrains during the inverse modeling.

In situ measurements of θ and ψ illustrate the complications arising for near-surface, arid soil systems (Figure 4-1). The very dynamic range of ψ (1-400 m) was coupled to a relatively small range of θ that seldom exceeds $0.10 \text{ m}^3 \text{ m}^{-3}$. Matric head (ψ) data above 200 m, measured using the *HDS*, were likely unreliable as they no longer responded to decreasing θ . As such, we restricted the *HDS* sensor data to <180 m in both the $RMSE_\psi$ and MBE_ψ calculations. The final water content data following the infiltrometer tests were used to constrain the retention curve at $\psi = -0.005\text{m}$. However, no data were observed between these two end points, making determination of inflection at air entry (α) uncertain, with original values ranging from -50 to +50 m. We added $K(h)$ data from the analytical solution to the fitting routine in RETC and significantly reduced the parameter uncertainty while maintaining an R^2 close to unity. The obtained parameters correspond to measured, coarse textures with relatively higher values of n and

α , and low values for θ_r . These direct parameterization methods and the indirect methods will be used in forward numerical simulations in section 4.5.3.

4.5 Results – Numerical Modeling

4.5.1 Parameter Sensitivities in the Near-surface, Arid Vadose Zone

Regional sensitivity analysis (*RSA*) is a useful step in any modeling procedure and involves the deviation from uniformity of the *posterior* distribution of parameters for each ranked criterion. In our multiobjective framework, these criteria were RMSE between observed and simulated soil water content ($RMSE_\theta$) and matric head ($RMSE_\psi$) across four soil depths. For brevity, only the results from *JWH*, the mid-textured soil are presented, but the other sites showed similar behavior (Figure 4-2). Two parameters were insensitive to both criteria, K_s and θ_s , which was evident by the correspondence between the ranked CDF (Figures 4-2a-d). The remaining parameters showed varying degrees of sensitivity depending on the criteria. For example, θ_r was the most sensitive parameter for $RMSE_\theta$ (Figure 4-2e) while simultaneously insensitive to $RMSE_\psi$ (Figure 4-2f). Inverse air-entry, α , displayed the opposite trend being very sensitive to $RMSE_\psi$. The remaining parameters, n and l , show a *posterior* CDF that differed from unity indicating sensitive parameters; however, the resulting CDFs were in conflict between the two criteria. The shape parameter, n , has a higher *posterior* value for $RMSE_\theta$ (Figure 4-2i) and a lower value for $RMSE_\psi$ (Figure 4-2i). The tortuosity parameter, here constrained from -1 to 1 and without physical significance, shows similar behavior.

Ranking each parameter according to its p -level from a two-sample Kolmogorov-Smirnov test, the sensitivities from high to low are θ_r , n , l , K_s , θ_s and α for the water content data ($RMSE_\theta$) and n , α , l , K_s , θ_s , and θ_r for matric head data ($RMSE_\psi$). The results showed that model sensitivity was data-dependent and that the favorable parameters for one criterion may not effectively minimize another parameter. This deficiency was likely related to inadequate model structure (scale, boundary conditions and the formulation of Richards' equation) or systematic errors in the observed data. However, the overall objective is to minimize both measures, because matric head and soil moisture control near-surface vadose zone processes, necessitating the need for a multiobjective optimization.

4.5.2 Multiobjective Parameter Optimization

In this section, we focus on the global optimization of these three sites and an increasing degree of vertical heterogeneity. The *RSA* analysis in the previous section found several conflicting parameters in the *posterior* CDF of the single-material system, indicating a need for compensation between criteria to find acceptable set of parameters. Given this compensation, it is unlikely that a single unique parameter set exists that can satisfy both criteria of moisture and head across all four depths. Soil characterization noted significant horizonation at both *LIZ* and *BLK* but not *JWH*. Three inverse modeling scenarios were conducted to evaluate the effect of increasing vertical heterogeneity on the multiple-criteria used for minimization (hereafter referred to as L_1 through L_3). The two-dimensional, normalized objective space (i.e., Pareto front) for *BLK* illustrated the compromise associated with increasing soil horizons. The Pareto-optimum solutions

(solid black circles) converged toward the origin with each increasing level of heterogeneity, indicating better model performance but also an increase in the number of model parameters (Figure 4-3). The shape of the Pareto front, as estimated by the Pareto-optimal solutions, was very sharp at L_1 (Figure 4-3a) and L_2 (Figure 4-3b) but became increasingly curvilinear with L_3 (Figure 4-3c). Thus, there was little tradeoff between criteria in L_1 (Figure 4-3a); however, the range of Pareto solution along the $g(RMSE_\theta)$ axis indicates that many solutions near the lower extreme of $g(RMSE_\psi)$ produced a very wide range of resulting $g(RMSE_\theta)$. Furthermore, none of these solutions can be excluded because each is non-dominated. The inflection was less sharp for L_2 but the range of non-dominated solutions was much lower. These situations manifested themselves more clearly in the time series data.

Matric head data were matched moderately well by the simplest L_1 scenario at *BLK* (Figure 4-4) with a minima log-transformed *RMSE* of 0.81 log(m) (Table 4-5). The Pareto-extreme for θ was significantly higher at 1.45 log(m). The overall spread of the Pareto solutions generally followed the dynamics of the ψ data over a wide range of values, but fails to fully encompass it. The θ time series showed more variability with most solutions related to lower values of $g(RMSE_\psi)$, and the majority overestimating θ considerably (Figure 4-5) with a $RMSE_\theta$ of $0.104 \text{ m}^3 \text{ m}^{-3}$ and a similar MBE_θ of $0.102 \text{ m}^3 \text{ m}^{-3}$. The other Pareto-extreme for θ was considerably better with a $RMSE_\theta$ of $0.009 \text{ m}^3 \text{ m}^{-3}$ and a MBE_θ of $-0.002 \text{ m}^3 \text{ m}^{-3}$. However, the compromise solution, in blue, retained a low *RMSE* for both θ and ψ of $0.011 \text{ m}^3 \text{ m}^{-3}$ and 0.91 log(m), respectively. As mentioned earlier, the L_2 scenario showed much less variability in Pareto-space (Figure 4-3b) which

became evident in the corresponding time series data (Figure 4-6). The observed data were well bounded by Pareto solutions for all depths. Statistically, the fit for the $RMSE_{\theta}$ was the same and only slightly improved for $RMSE_{\psi}$ (Table 4-5).

In contrast, results at *LIZ* (the sandy soil) indicated a wide distribution of Pareto-solutions along the $g(RMSE_{\psi})$ resulting in wide distribution of ψ in the time series data (not shown) and the final statistics (Table 4-5). The minimum $RMSE_{\theta}$ of $0.009 \text{ m}^3 \text{ m}^{-3}$ was achieved in the L_1 scenario; additional soil horizons only affected ψ . This was observed in the Pareto-extreme values with ψ decreasing the RMSE from 423 m (L_1) down to 42.5 m (L_3) and MBE from -34 m (L_1) down to -14.1 m (L_3). Note, the corresponding $RMSE_{\theta}$ is much higher indicating that good fit to one criterion was detrimental to another.

Model deficiencies and errors in the defined boundary conditions or observational data make it unlikely that a single parameter set will simultaneously minimize both objectives. The Pareto set of solutions was defined at 100 values in the AMALGAM algorithm [Vrugt and Robinson, 2007]. The resulting suite of parameters provides some indication of minimal uncertainty, although more rigorous methods are available [Wöhling and Vrugt, 2011]. The CDF of these parameters for the L_3 scenario at *JWH*, the loamy sand lacking distinct horizonation, shows that these parameters vary significantly with the three layers for the more sensitive parameters such as θ_r (Figure 4-7a) and n (Figure 4-7d). Additionally, the shape parameter, n , is bifurcated with a population around 1.5 and 2.5. Other, less sensitive parameters (e.g., K_s) span the entire range of parameter space with bifurcation at both extremes for layers 1 and 2 (Figure 4-7e).

Similarly, α covers a moderate and realistic range for horizons L_1 and L_2 (Figure 4-7c). Retention data near saturation was lacking, and as the infiltration front attenuates with depth, this lack of data information α unrealistically low (0.005 m^{-1}) in Layer 3, for a coarse textured soil. Thus, a region of parameter space exists that results in unrealistic parameter combinations that effectively produce a non-dominant Pareto solution but which were outside the realm of physically based parameters.

Two insensitive parameters, K_s and θ_s , were directly measured using tension infiltrometers. Field estimates of K_s are extremely variable and it is generally logarithmically distributed while θ_s is more normally distributed [Nielsen *et al.*, 1973]. We used the field-determined, *a priori* parameter distributions of both parameters presented in Table 4-4 to constrain the 2-layer optimizations. The parameter space normalized over the uncertainty bounds for the global L_2 scenario at *BLK* showed the wide distribution of θ_s and K_s in the surface layer (Figure 4-8a). Layer 2 was particularly well-defined under the global optimization with the exception of θ_r and θ_s . Constraining θ_s and K_s to their respective 95% confidence intervals reduces parameter uncertainty except for l^2 (Figure 4-8b) and results in a moderate decrease in optimization criteria of the compromise solution for $RMSE_\theta$ at all sites (Table 4-6). However, the compromise $RMSE_\psi$ decreased from 61.8 to 53.8 m at *LIZ*, and 59.5 to 0.42m at *BLK*, while *JWH* showed a moderate increase and little effect on MBE_θ and MBE_ψ .

Finally, soil temperature was not optimized under any scenario and was found to be insensitive to any parameterization (Table 4-5). Regardless of the Pareto-extreme value or site, the $RMSE_T$ and MBE_T were largely constant. Consider the most obvious

example: the homogeneous scenario (L_1) at *LIZ*. The Pareto-extremes, as noted above, significantly biased the other criterion, yet had no effect on soil T . Additionally, these near-surface soils had maximum temperature in excess of 50°C and diurnal changes of >25°C, yet using microclimate data from 45 km away robustly determined soil temperatures to depths to 0.5 m.

4.5.3 Direct and Indirect Methods of Parameterization

As outlined in Table 4-1, we used two direct and three indirect methods to parameterize the HYDRUS model for forward simulations. Direct characterization using infiltrometer data both at the surface and 0.1m yielded good θ -RMSE values to simulations of 0.009, 0.016 and 0.018 $\text{m}^3 \text{m}^{-3}$ at *LIZ*, *JWH*, and *BLK*, respectively, at 3-cm depth with very similar results at 10-cm depth. The individual RMSE values increased with depth and as shown in the whole-profile $RMSE_\theta$ and MBE_θ in Table 4-7 and Figure 4-9. In comparison, the ψ -RMSE was much worse and underestimated absolute heads (Figure 4-10). The tension infiltrometer provided detailed $K(h)$ data and estimates of the water retention characteristics through inversion of outflow data near-saturation. We believed that coupling these data to *in situ* data of water retention and optimized in RETC would significantly improve this characterization method. Despite excellent fits to the combined data set ($R^2 > 0.98$), the resulting forward simulations were quite poor, overestimating θ from as little as 0.024 $\text{m}^3 \text{m}^{-3}$ at *LIZ* to as much as 0.043 $\text{m}^3 \text{m}^{-3}$ at *JWH*. The matric head data ultimately showed lower values as well (e.g., Figure 4-10) but were an order of magnitude closer to the observed data.

The indirect methods also produced good results for θ , albeit poorer than those results obtained using AMALGAM. The coarsest textured soil at *LIZ* was numerically unstable using the textural classification of sand (I_1). The addition of particle size and bulk density (I_2) produced poor fits for both θ ($RMSE = 0.061 \text{ m}^3 \text{ m}^{-3}$) and ψ ($RMSE = 106 \text{ m}$). Again, we note that soil *T* was unaffected (Table 4-7). Results for the loamy sand (*JWH*) and sandy loam (*BLK*) soils were better, even using the I_1 (texture only) method. The correction for coarse gravel content (I_3) reduced the $RMSE_\theta$ over both the I_1 and I_2 methods at *LIZ* and *JWH*, but increased $RMSE_\theta$ at *BLK*, the most gravel-rich soil. The matric head data were still underestimated by all indirect methods, though the results were somewhat less biased than the direct methods (Figure 4-10). The gravel correction had little impact on results, likely because soils are so far from saturation where gravel volume affects flow. Gribb et al. [2009] found that excluding gravel volume over-corrected $\theta(\psi)$ in the dry end of the retention curve, and generally did not improve model performance.

4.6 Discussion and Conclusions

These results present a unique coupling of soil moisture, matric head and temperature data in the near-surface inverse modeling of an arid vadose zone. Many previous studies have found parameters associated with near-saturated conditions to be particularly sensitive in numerical modeling. For example, Mertens et al. [2005] found K_s and θ_s to be the most sensitive parameters, and n the least sensitive, when studied on a sandy loam soil in Belgium. In fact, θ_r is commonly set arbitrarily to zero because it is seldom attainable under field conditions [Schaap and Bouten, 1996]. Our results found

θ , n , and l sensitive to water content data ($RMSE_{\theta}$) and n , α , and l sensitive to matric head data ($RMSE_{\psi}$).

Soil temperature was found to be an insensitive state variable, but robustly determined under any scenario and using non-local meteorological data. Inverse modeling produced results equally accurate with respect to θ , with all RMSE values generally at or below $0.01 \text{ m}^3 \text{ m}^{-3}$, regardless of the degree of vertical heterogeneity. The largest discrepancies were found in ψ , which was generally very high and exceeded the calibration range of the HDS ($>150 \text{ m}$). These results are somewhat surprising considering that the observed range of ψ was much wider than θ and a more dynamic variable generally provides more information for the objective function [Vrugt *et al.*, 2003]. Minimizing the log-transformed RMSE through inverse modeling decreased model sensitivity to the higher values. However, simply using the RMSE for ψ resulted in parameter values that restricted water movement into the profile, because RMSE was skewed to reduced residuals at the very dry end. The log-transform minimized this effect and resulted in smoother Pareto fronts.

Ultimately, the optimizations compensated for the underestimation of ψ by forcing the α and n parameters to uncharacteristically low values for such coarse textures (Figure 4-8). This compensation keeps the hydraulic capacity sufficiently high at lower water contents to maintain conductivity towards to the surface and remove soil moisture. Otherwise, hydraulic conductivity is quickly reduced beyond air-entry and moisture stagnates as observed with the indirect *PTF* data (Figure 4-10). Optimizations were also attempted using the more robust energy balance surface condition as well as vapor

transport; however, this only resulted minimally more water lost (~5%) which still failed to increase the ψ to dry values beyond 200 m at depth. Ultimately we suspect a structural error in the model; which will be grounds for further research.

Additionally, the ψ data from the *HDS* shows a peculiar inflection during dry-down periods (e.g. Figure 4-4c). This data should mirror θ with a sharp peak a convex drying front; however, concavity is more often observed. We believe that this hysteretic behavior was related to the properties of the porous ceramic which may become hydraulically disconnected from the surrounding soil leaving moisture in the plug which was removed more slowly by vapor transport. This effect became more obvious as on the coarser textured soils. These concerns also cast doubts on the *HDS* ability to wet quickly enough to reach equilibrium with the soil before the infiltration front dissipates. Better soil moisture monitoring will only improve our ability to refine our models and future efforts will focus on monitoring ψ across the extreme range found in non-irrigated lands.

Lastly, arid systems typically span a narrow range of θ affecting our ability to resolve the wet-end hydraulic characteristics. The near-saturated measurements from infiltrometers were used directly, but the results were not very promising when applied to simulated ψ . In general, all our modeling techniques worked well for θ but not necessarily for ψ , which was compensated by increasing hydraulic capacity. Our Pareto-results showed that we could also obtain a substantial spread of θ compared to a confined time series of ψ (Figure 4-5). Thus, without some means to evaluate both state variables, inverse modeling solely to one may be suspect under any climatic region. The conjunctive use of both ψ and θ in the multiobjective framework avoids these pitfalls.

Our inverse modeling ultimately produced the best results for ψ over either direct or indirect methods. However, as shown in Figure 4-1, we lack sufficient moisture dynamics to effectively determine wet-end parameters (e.g., θ_s and α) in a global optimization. The use of parameter constraints modestly decreased overall model performance but provided more physically realistic parameters which may decrease the overall model certainty. Without more extreme atmospheric conditions, we can only speculate how the modeled moisture dynamics may respond beyond our calibration data.

4.7 Tables

Table 4-1. Summary of direct, indirect, and inverse methods used to obtain effective hydraulic parameters

<i>Method</i>	<i>ID</i>	<i>Description</i>
<i>Direct</i>	D_1	Tension infiltrometer (TI) data at surface and 10-cm
	D_2	Combination of reduced <i>in situ</i> retention data and $K(h)$ data in RETC
<i>Indirect</i>	I_1	Textural classification (Rosetta)
	I_2	Sand, silt, clay, and bulk density (Rosetta)
	I_3	Adjusted for coarse fragment (>2 mm) content (Rosetta)
<i>Inverse</i>	L_1	Single layer, 0-1 m
	L_2	Two-layers, 0-0.1 m, and 0.1-1 m
	L_3	Three-layers, 0-0.1 m, 0.1-horizon, and horizon -1 m

Table 4-2. Parameter uncertainty bounds for hydraulic parameters in equations [2] and [3] used in both the regional sensitivity analysis and the global optimization algorithm

Parameter	Units	Bounds		Description
		Lower	Upper	
θ_r	$\text{m}^3 \text{m}^{-3}$	0	0.04	Residual water content
θ_s	$\text{m}^3 \text{m}^{-3}$	0.15	0.50	Saturated water content
α	m^{-1}	0.5	15	Inverse air-entry potential
n	-	1.1	3	Shape parameter
K_s	cm d^{-1}	10	1000	Saturated conductivity
l	-	-1	1	Pore-connectivity

Table 4-3. Mean soil texture characterization for each horizon averaged from 4-5 soil trenches.

Site	Horizon	Depth [cm]	Texture ¹	Sand ² [%]	Silt ² [%]	Clay ² [%]	Gravel ³ [%]	BD _T ⁴ [g cm ⁻³]	EC ⁵ [dS m ⁻¹]
LIZ	Ap/C	0 - 33	S	90.3	4.9	4.8	14.6	1.72	0.35
	Btk1	33 - 48	LS	75.5	7.9	16.6	18.9	1.76	1.85
	Btk2	48 - 75+	LS	78.9	8.8	12.3	24.9	1.74	3.61
JWH	Ap	0 - 10	LS	85.6	9.3	5.2	16.1	1.81	0.51
	Ck	10 - 53	LS	86.7	6.9	6.4	17.1	1.71	0.39
	Bwk	53 - 75+	LS	88.0	5.2	6.9	13.7	1.75	1.78
BLK	Ap	0 - 9	SL	80.3	14.5	5.2	41.5	1.72	0.75
	Ck	9 - 28	LS	84.8	9.7	5.5	41.3	1.71	0.74
	Bwk	28 - 65	SL	73.9	18.9	7.3	22.6	1.57	1.44

¹S, Sand; LS, loamy sand; SL, sandy loam

²Sand, silt and clay weight percentages based on fine-earth (<2mm) fraction of the total soil

³Gravel is weight percent > 2mm

⁴BD_T, total soil bulk density

⁵EC, electrical conductivity

Table 4-4. Mean hydraulic properties from tension infiltrometer tests and their respective confidence intervals (CI) at 95%. These intervals also represent the *a priori* constrained parameter space for θ_s and K_s .

Site	Depth [m]	N	θ_s [m ³ m ⁻³]	95% CI		K_s [cm d ⁻¹]	95% CI	
				Lower	Upper		Lower	Upper
LIZ	0.0	4	0.303	0.271	0.336	439	295	583
	0.1	1	0.333	0.300	0.366	283	139	427
JWH	0.0	4	0.353	0.320	0.386	411	295	527
	0.1	1	0.331	0.298	0.364	255	140	371
BLK	0.0	6	0.252	0.229	0.275	92.5	43.7	141
	0.1	2	0.234	0.201	0.267	223	174	271

Table 4-5. Root mean square error ($RMSE$) and mean bias error (MBE) between simulated and observed values of θ , ψ , and soil temperature (T) for the Pareto-extreme solutions for θ ($ParEx_\theta$), for ψ ($ParEx_\psi$) and the compromise solution for three degrees of increasing vertical heterogeneity (L_{1-3}). The AMALGAM code optimized $RMSE_\theta$ and $log(RMSE_\psi)$ and the minimal values are presented in bold.

<i>Site</i>	<i>Scenario</i>		$RMSE_\theta$	MBE_θ	$Log(RMSE_\psi)$	$Log(MBE_\psi)$	$RMSE_\psi$	MBE_ψ	$RMSE_T$	MBE_T
			[$m^3 m^{-3}$]	[$m^3 m^{-3}$]	log [m]	log [m]	[m]	[m]	[C]	[C]
LIZ	L₁	ParEx _θ	0.009	0.000	2.49	2.18	432.3	385.9	3.10	1.43
		ParEx _ψ	0.014	0.003	1.11	-0.05	69.3	-33.7	3.03	1.39
		Comp.	0.013	0.001	1.13	0.04	68.0	-30.1	3.01	1.38
	L₂	ParEx _θ	0.009	0.000	1.80	-1.38	80.3	-60.2	2.94	1.27
		ParEx _ψ	0.012	-0.003	0.96	-0.06	56.8	-27.7	2.99	1.26
		Comp.	0.011	0.000	0.98	-0.11	61.8	-33.1	3.09	1.42
	L₃	ParEx _θ	0.009	-0.001	1.04	-0.27	70.3	-44.6	3.05	1.39
		ParEx _ψ	0.015	-0.003	0.85	0.07	42.5	-14.1	2.94	1.20
		Comp.	0.010	0.000	0.94	-0.14	58.0	-34.1	2.93	1.21
JWH	L₁	ParEx _θ	0.010	0.000	2.44	-2.16	83.7	-65.4	2.18	0.48
		ParEx _ψ	0.013	-0.007	1.07	0.03	52.1	-17.5	2.00	0.30
		Comp.	0.013	-0.007	1.07	0.03	52.1	-17.5	2.00	0.30
	L₂	ParEx _θ	0.009	0.000	2.42	-2.13	83.7	-65.2	2.10	0.38
		ParEx _ψ	0.012	-0.005	0.96	-0.01	52.8	-18.5	2.00	0.31
		Comp.	0.011	-0.002	0.96	-0.04	53.8	-21.0	2.01	0.32
	L₃	ParEx _θ	0.009	0.000	1.98	-1.18	72.2	-41.1	2.09	0.40
		ParEx _ψ	0.013	-0.006	0.91	-0.03	53.1	-18.6	2.15	0.34
		Comp.	0.010	0.000	0.92	-0.09	56.9	-20.2	2.05	0.35
BLK	L₁	ParEx _θ	0.009	0.000	1.45	1.02	105.2	67.6	1.92	0.69
		ParEx _ψ	0.104	0.102	0.81	-0.06	54.3	-23.8	1.86	0.71
		Comp.	0.011	-0.002	0.91	-0.08	60.7	-26.0	1.92	0.70
	L₂	ParEx _θ	0.009	0.000	1.09	0.19	76.7	-1.0	1.92	0.69
		ParEx _ψ	0.033	0.015	0.79	-0.06	54.8	-24.2	1.89	0.72
		Comp.	0.010	0.000	0.90	0.00	59.5	-20.6	1.91	0.69
	L₃	ParEx _θ	0.007	0.001	0.98	-0.18	63.5	-31.5	2.00	0.69
		ParEx _ψ	0.049	0.019	0.72	-0.03	46.0	-16.2	1.89	0.71
		Comp.	0.008	0.000	0.92	0.00	55.9	-22.9	2.00	0.69

Table 4-6. Root mean square error (*RMSE*) and mean bias error (*MBE*) between simulated and observed values of θ , and ψ for the Pareto compromise solution using constrained parameter space and the two-layer (L_{2c}) scenario

<i>Site</i>	<i>Scenario</i>	<i>RMSE</i> $_{\theta}$ [m ³ m ⁻³]	<i>MBE</i> $_{\theta}$ [m ³ m ⁻³]	<i>Log</i> (<i>RMSE</i> $_{\psi}$) log [m]	<i>Log</i> (<i>MBE</i> $_{\psi}$) log [m]	<i>RMSE</i> $_{\psi}$ [m]	<i>MBE</i> $_{\psi}$ [m]
<i>LIZ</i>	L_{2c}	0.013	-0.001	1.00	0.05	53.8	-19.5
<i>JWH</i>	L_{2c}	0.011	0.000	1.09	0.03	54.8	-21.1
<i>BLK</i>	L_{2c}	0.010	0.000	0.82	-0.03	42.0	-16.6

Table 4-7. Root mean square error (*RMSE*) and mean bias error (*MBE*) between direct and indirect parameterization of simulated and observed values of θ and ψ .

<i>Site</i>	<i>Method</i>	<i>RMSE</i> $_{\theta}$	<i>MBE</i> $_{\theta}$	<i>L</i> (<i>RMSE</i> $_{\psi}$)	<i>L</i> (<i>MBE</i> $_{\psi}$)	<i>RMSE</i> $_{\psi}$	<i>MBE</i> $_{\psi}$	<i>RMSE</i> $_T$	<i>MBE</i> $_T$
<i>LIZ</i>	D_1	0.015	0.000	4.76	-3.90	150.1	-66.2	2.98	1.34
	D_2	0.034	0.024	2.73	-1.84	152.5	-43.6	3.03	1.40
	I_1	Failed simulation							
	I_2	0.061	0.052	1.68	-1.24	105.7	-79.1	3.00	1.36
	I_3	0.041	0.034	1.91	-1.51	110.8	-85.6	2.99	1.35
<i>JWH</i>	D_1	0.014	0.000	4.93	-4.73	87.6	-70.0	2.22	0.48
	D_2	0.047	0.043	3.26	-3.06	86.0	-68.4	2.23	0.51
	I_1	0.020	0.017	1.78	-1.33	78.3	-58.4	2.25	0.50
	I_2	0.011	0.002	2.05	-1.67	80.8	-61.7	2.15	0.45
	I_3	0.011	-0.002	2.10	-1.72	81.1	-62.1	2.13	0.43
<i>BLK</i>	D_1	0.018	-0.012	4.60	-4.44	98.6	-77.5	1.95	0.68
	D_2	0.038	0.035	2.99	-2.80	96.3	-75.0	1.92	0.69
	I_1	0.016	0.006	1.50	-1.16	83.5	-60.6	1.85	0.68
	I_2	0.016	-0.007	1.88	-1.57	88.3	-65.8	1.89	0.67
	I_3	0.023	-0.016	1.85	-1.50	87.9	-65.0	1.92	0.66

4.8 Figures

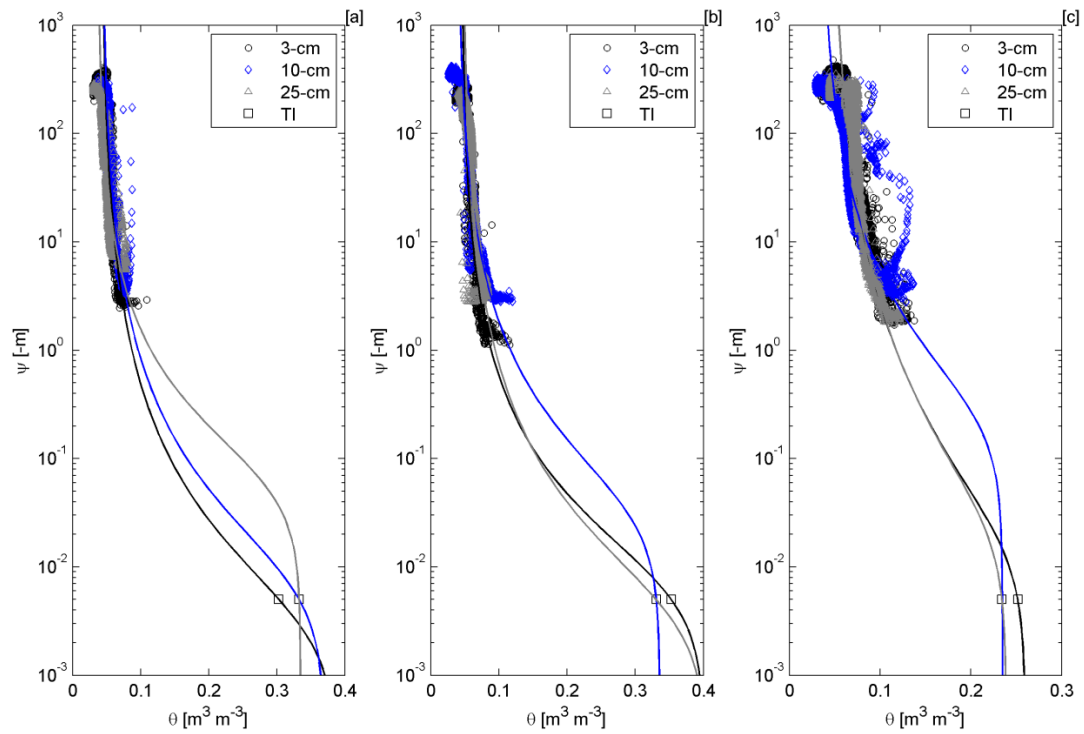


Figure 4-1. Observed water retention data from the 3-, 10-, and 25-cm *in situ* soil sensors at [a] LIZ, [b] JWH, and [c] BLK field sites. The corresponding solid lines represent the data fitted to Eq. [3]. The near-saturated water content was constrained using field-measured θ ($\psi = 0.005\text{m}$) following each tension infiltrometer (TI) test.

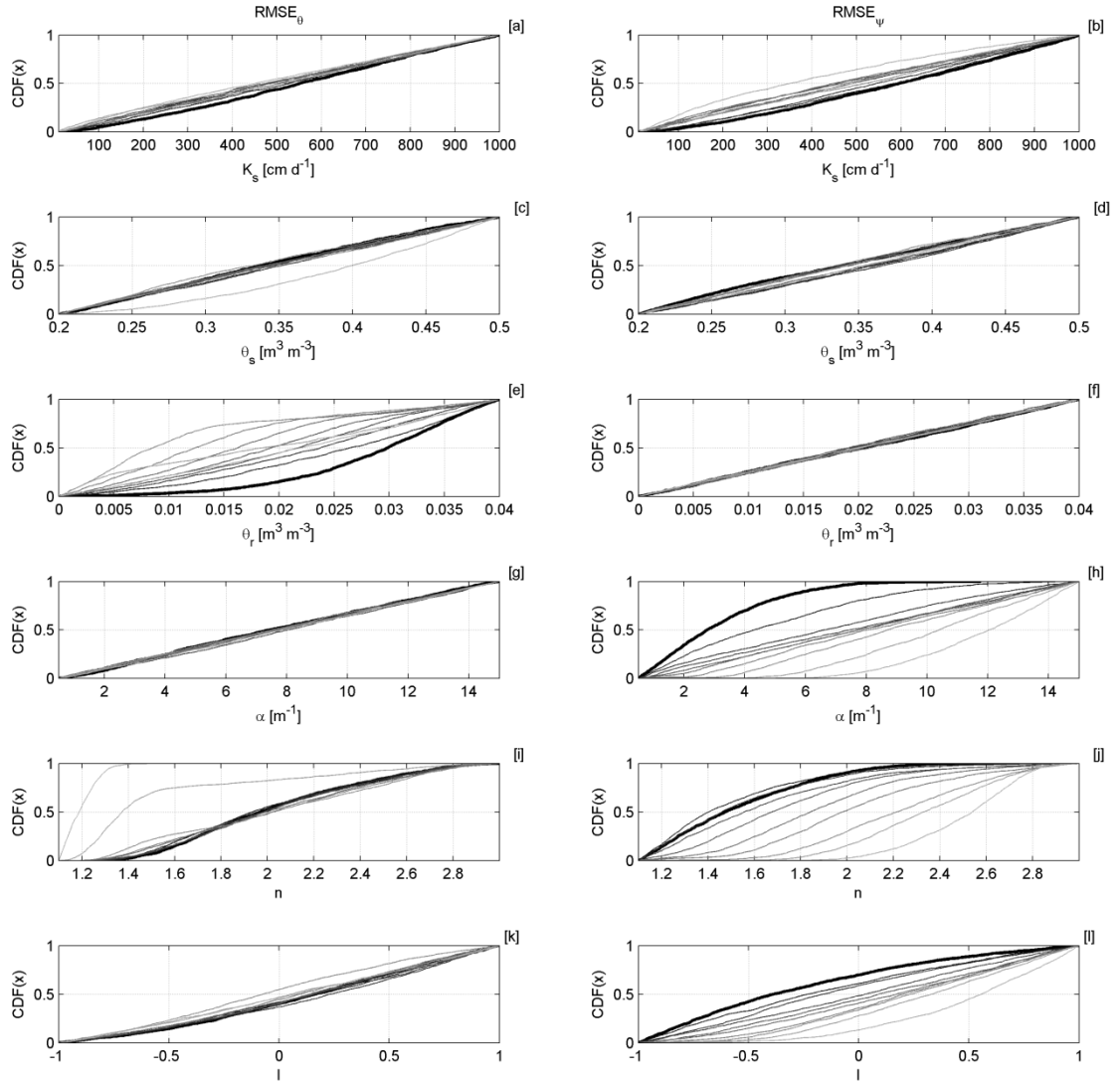


Figure 4-2. The cumulative distribution function (CDF) of ranked parameters for a single-layer (0-100cm) regional sensitivity analysis at *JWH*. Each line represents 10% of the population grading from the ‘best’ (thick black line) to ‘worst’ (light gray) model performance for each criterion. Each column represents the criterion performance $RMSE_0$ (left) and $RMSE_\psi$ (right) for each hydraulic parameter.

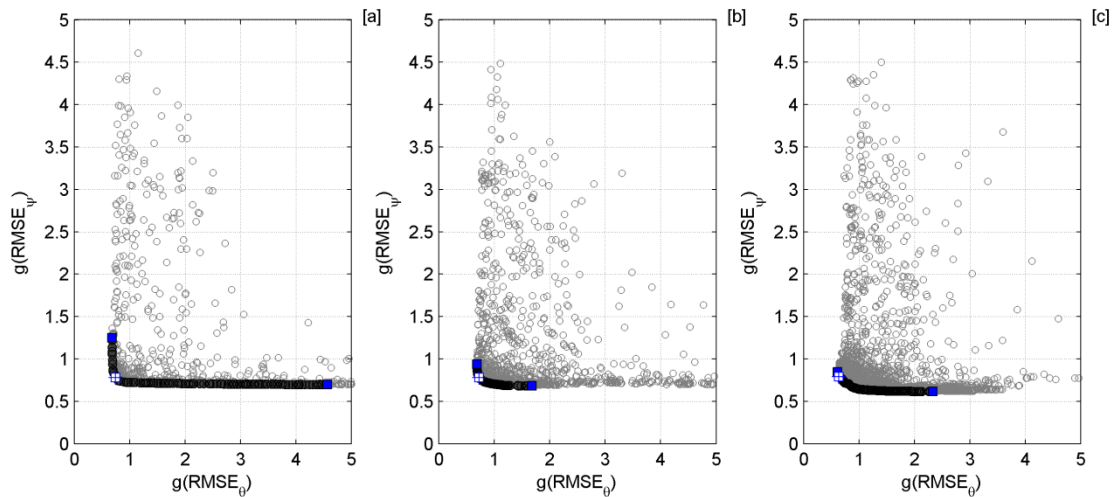


Figure 4-3. Non-dominated, Pareto-optimal solutions (dark circles) and previous dominated solutions (gray circles) for the global optimization runs with [a] one-layer, L_1 ; [b] two-layer, L_2 , and [c] three-layer, L_3 soil profile. The Pareto extremes are denoted by blue squares and the compromise solution with a white cross. The normalized Pareto objective space represents the tradeoff between $g(\text{RMSE}_\theta)$ and $g(\text{RMSE}_\psi)$.

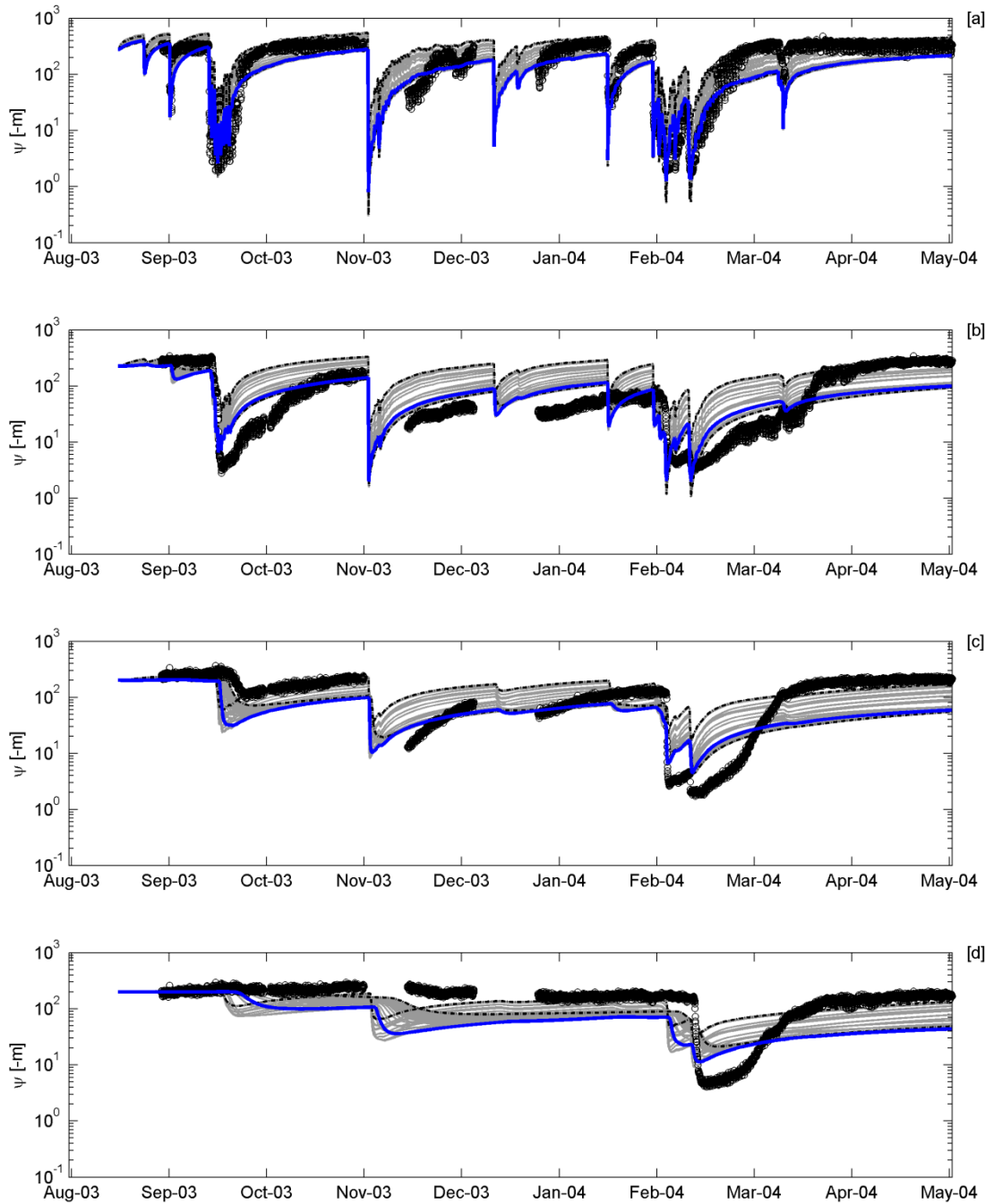


Figure 4-4. Observed (circles) and simulated absolute heads (ψ) at [a] 0.03, [b] 0.10, [c] 0.25 and [d] 0.45 m depths for the AMALGAM single-layer, L_1 , optimization at *BLK*. Gray lines are all Pareto-optimal values, the hashed lines are Pareto-extremes, and the compromise solution is in blue.

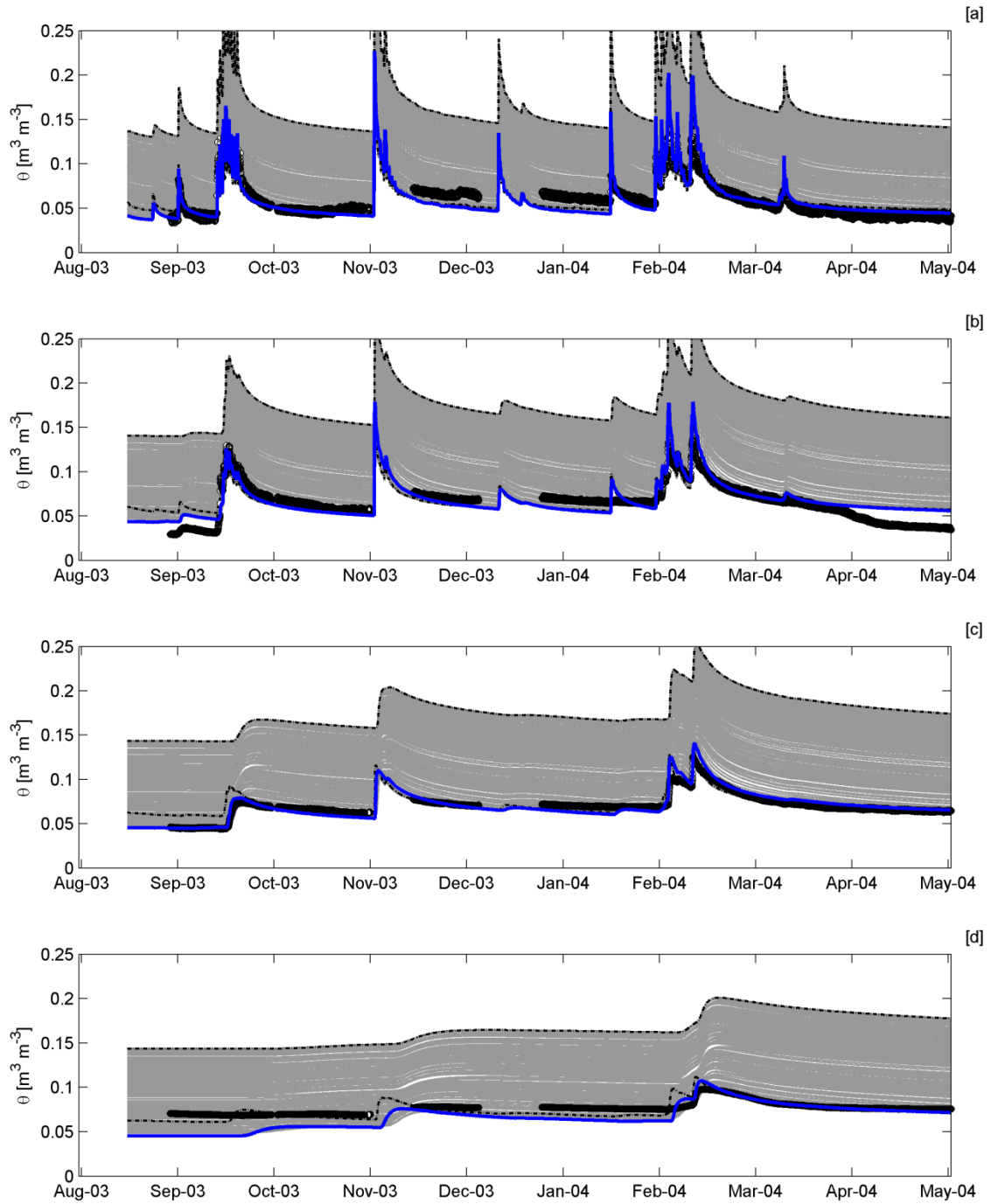


Figure 4-5. Observed (circles) and simulated water contents (θ) at [a] 0.03, [b] 0.10, [c] 0.25 and [d] 0.45 m depths for the AMALGAM single-layer, L_1 , optimization at *BLK*. Gray lines are all Pareto-optimal values, the hashed lines are Pareto-extremes, and the compromise solution is in blue.

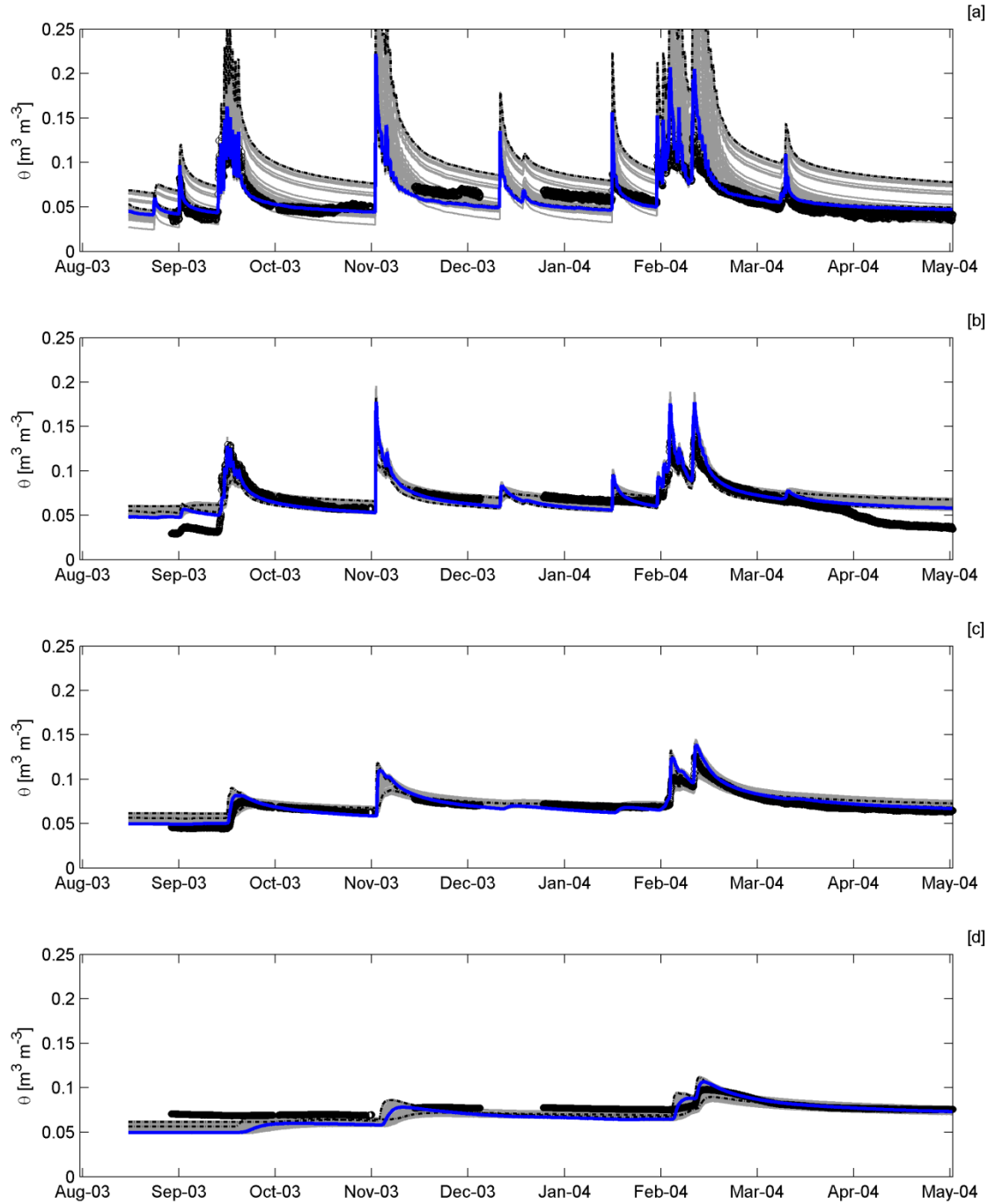


Figure 4-6. Observed (circles) and simulated water contents (θ) at [a] 0.03, [b] 0.10, [c] 0.25 and [d] 0.45 m depths for the AMALGAM double-layer, L_2 , optimization at *BLK*. Gray lines are all Pareto-optimal values, the hashed lines are Pareto-extremes, and the compromise solution is in blue.

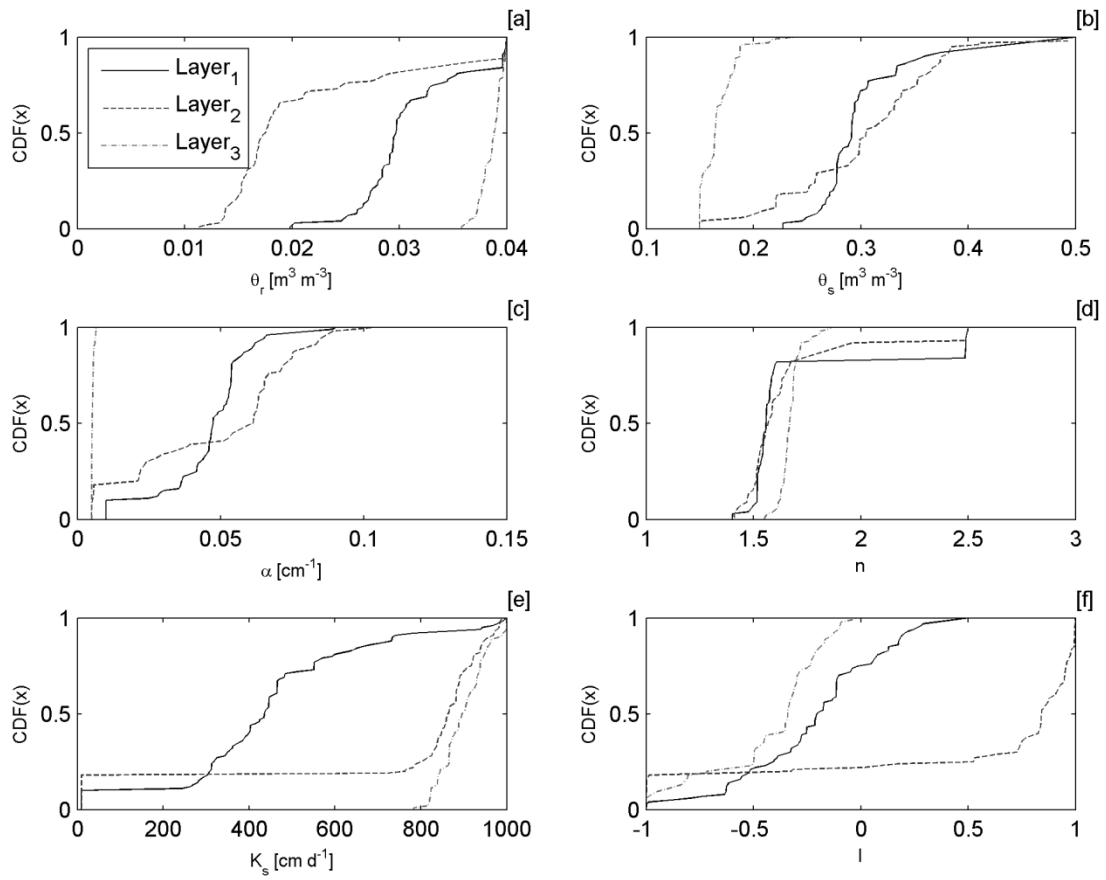


Figure 4-7. Cumulative distribution functions (CDF) of Pareto-optimal solutions for layers 1-3 from the L_3 scenario at JWH.

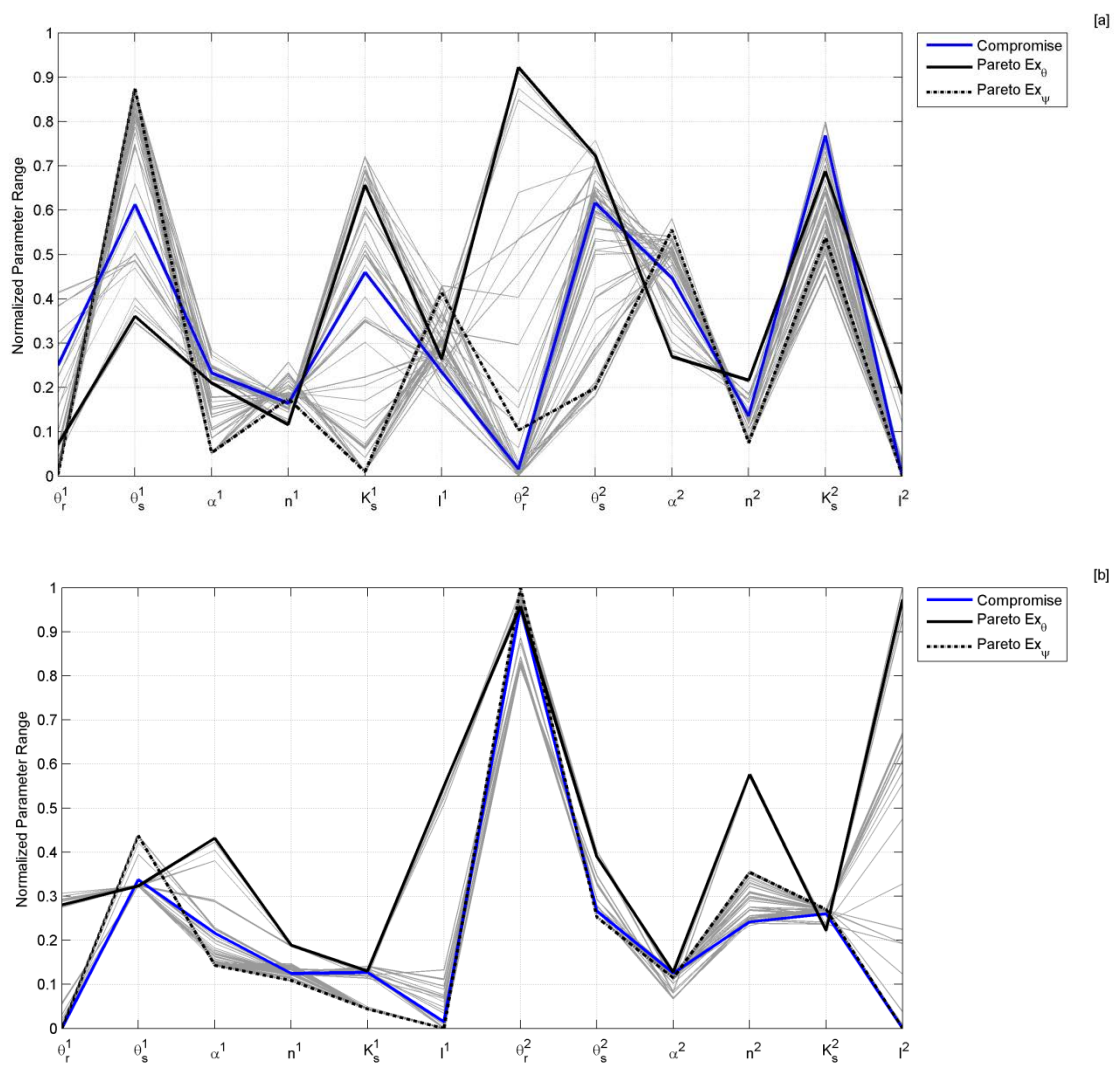


Figure 4-8. Normalized Pareto optimal parameters for the [a] global and [b] constrained two-layer, L_2 scenario at BLK . Each gray line represents one Pareto-optimal solution. The black lines are Pareto-extremes and compromise solution is the solid blue line. The superscripts indicate the respective soil layer.

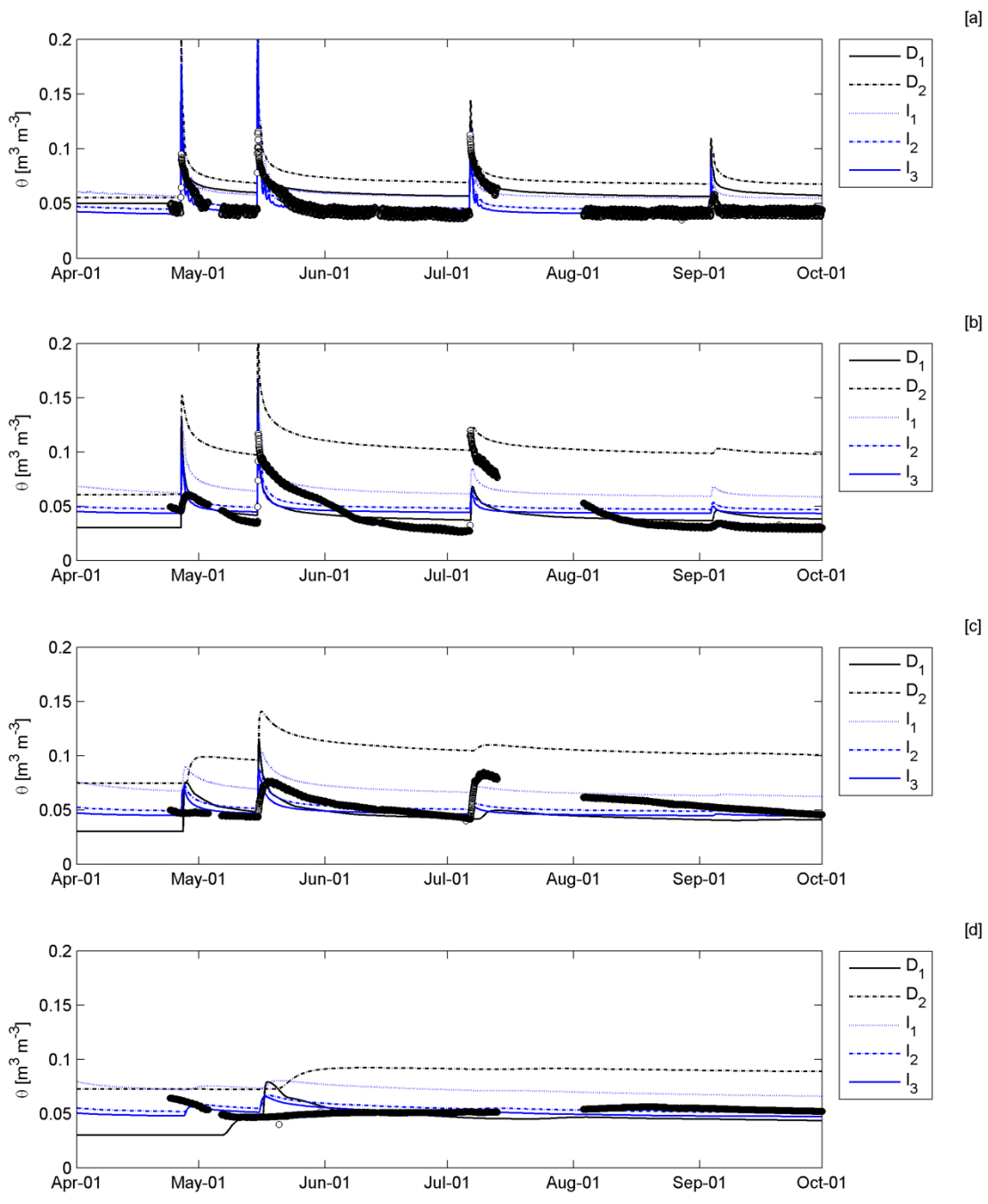


Figure 4-9. Time series plot of soil moisture (θ) at *JWH* parameterized using direct measurements from tension infiltrometers (D_1), *in situ* water retention combined with infiltrometer $K(h)$ data in RETC (D_2), and three PTF results as outlined in Table 4-1.

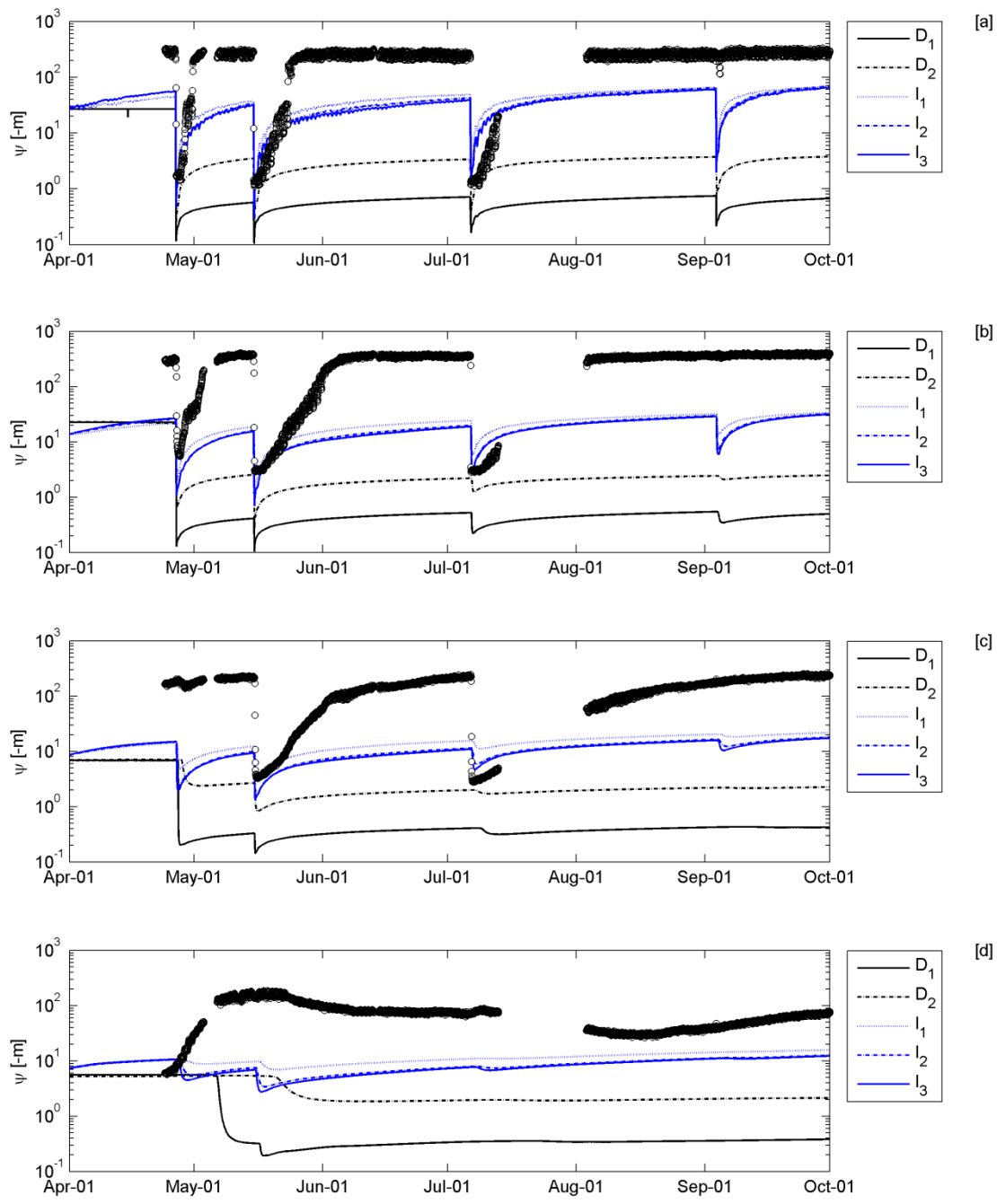


Figure 4-10. Time series plot of potential (ψ) at *JWH* parameterized using direct measurements from tension infiltrometers (D_1), *in situ* water retention combined with infiltrometer $K(h)$ data in RETC (D_2), and three PTF results outline in Table 4-1.

4.9 Acknowledgments

The authors express their gratitude to J. Vrugt (UC Irvine) for the AMALGAM algorithm, J. Šimůnek (UC Riverside) for his quick responses to any HYDRUS issues, and finally to B. Lyles (DRI), Jason Ritter (CSI), Jim Bilski (CSI) for their assistance with data acquisition. We gratefully acknowledge support from ITAM (Charis Subcontract No. GS-012FG-A) and the Army Research Office (W911NF-08-1-0453).

4.10 References

- Allen, R. G. (2008a), REF-ET: Reference evapotranspiration calculation software, V3.1, University of Idaho, Kimberly, ID, available at <http://www.kimberly.uidaho.edu/ref-et/>
- Allen, R. G. (2008b), Quality assessment of weather data and micrometeorological flux: Impacts on evapotranspiration calculation, *J. Agric. Meteorol.*, *64*, 191-204.
- Andraski, B. J. (1991), Balloon and core sampling for determining bulk density of alluvial desert soil, *Soil Sci. Soc. Am. J.*, *55*, 1188-1190.
- Andraski, B. J. (1997), Soil-water movement under natural-site and waste-site conditions: A multiple-year field study in the Mojave Desert, Nevada, *Water Resour. Res.*, *33*, 1901-1916.
- ASCE-EWRI (2005), The ASCE Standardized Reference Evapotranspiration Equation. ,ASCE-EWRI Standarization of Reference Evapotranspiration Task Committee Report 58 pp.
- Brakensiek, D. L., W. J. Rawls, and G. R. Stephenson (1986), A note on determining soil properties for soils containing rock fragments, *J. Range Manage.*, *39*, 408-409.
- Caldwell, T. G., E. V. McDonald, and M. H. Young (2006), Soil disturbance and hydrologic response at the National Training Center, Ft. Irwin, California, *J. Arid Environ.*, *67*, 456-472.
- Caldwell, T. G., E. V. McDonald, and M. H. Young (2009), The seedbed microclimate and the active revegetation of disturbed lands in the Mojave Desert, *J. Arid Environ.*, *73*, 563-573.
- Caldwell, T. G., M. H. Young, J. Zhu, and E. V. McDonald (2008), Spatial structure of hydraulic properties from canopy to interspace in the Mojave Desert, *Geophys. Res. Lett.*, *35*, L19406, doi, 10.1029/2008GL035095.
- Caldwell, T. G., M. H. Young, E. V. McDonald, and J. Zhu (In submission), Biotic and abiotic controls on soil heterogeneity in arid shrublands, *Water Resour. Res.*

- Casey, F. X. M., and N. E. Derby (2002), Improved design for an automated tension infiltrometer, *Soil Sci. Soc. Am. J.*, 66, 64-67.
- Chung, S. O., and R. Horton (1987), Soil Heat and Water-Flow with a Partial Surface Mulch, *Water Resour. Res.*, 23, 2175-2186.
- Dane, J. H., and S. Hruska (1983), In situ determination of soil hydraulic properties during drainage, *Soil Sci. Soc. Am. J.*, 47, 619-624.
- Duan, Q. Y., S. Sorooshian, and V. Gupta (1992), Effective and efficient global optimization for conceptual rainfall-runoff models, *Water Resour. Res.*, 28, 1015-1031.
- Eagleson, P. S. (1978), Climate, soil, and vegetation, 3, A simplified model of soil moisture movement in the liquid phase, *Water Resour. Res.*, 14, 722-730.
- Gee, G. W., and D. Or (2002), Particle-size analysis, in *Methods of Soil Analysis, Part 4. Physical Methods*, edited by J. H. Dane and G. C. Topp, pp. 255-293, Soil Science Society of America Book Series, Madison.
- Gribb, M. M., I. Forkutsa, A. Hansen, D. G. Chandler, and J. P. McNamara (2009), The Effect of Various Soil Hydraulic Property Estimates on Soil Moisture Simulations, *Vadose Zone J.*, 8, 321-331, 10.2136/vzj2008.0088.
- Grossman, R. B., and T. G. Reinsch (2002), Bulk density and linear extensibility, in *Methods of Soil Analysis, Part 4: Physical Methods*, edited by J. H. Dane and G. C. Topp, pp. 201-253, Soil Science Society of America, Madison.
- Gupta, H. V., S. Sorooshian, and P. O. Yapo (1998), Toward improved calibration of hydrologic models: Multiple and noncommensurable measures of information, *Water Resour. Res.*, 34, 751-763.
- Hendrickx, J. M. H., P. J. Wierenga, and M. S. Nash (1990), Variability of soil-water tension and soil-water content, *Agricultural Water Management*, 18, 135-148.
- Jacques, D., J. Simunek, A. Timmerman, and J. Feyen (2002), Calibration of Richards' and convection-dispersion equations to field-scale water flow and solute transport under rainfall conditions, *J. Hydrol.*, 259, 15-31.
- Kampf, S. K., and S. J. Burges (2007), Parameter estimation for a physics-based distributed hydrologic model using measured outflow fluxes and internal moisture states, *Water Resour. Res.*, 43, W12414, doi:10.1029/2006WR005605.
- Kirchner, J. W. (2006), Getting the right answers for the right reasons: Linking measurements, analyses, and models to advance the science of hydrology, *Water Resour. Res.*, 42, W03S04, doi:10.1029/2005WR004362..
- Logsdon, S. D., and D. B. Jaynes (1993), Methodology for determining hydraulic conductivity with tension infiltrometers, *Soil Sci. Soc. Am. J.*, 57, 1426-1431.
- Madsen, H. (2000), Automatic calibration of a conceptual rainfall-runoff model using multiple objectives, *J. Hydrol.*, 235, 276-288.

- McDonald, E. V. (2002), Numerical simulations of soil water balance in support of revegetation of damaged military lands in arid regions, *Arid Land Res. Manag.*, 16, 277-290.
- McDonald, E. V., L. D. McFadden, and S. G. Wells (2003), Regional response of alluvial fans to the Pleistocene-Holocene climatic transition, Mojave Desert, California, in *Paleoenvironments and Paleohydrology of the Mojave and southern Great Basin Deserts*, edited by Y. Enzel, S. G. Wells and N. Lancaster, pp. 189-205, Geological Society of America Special Paper 368., Boulder, CO.
- McDonald, E. V., F. B. Pierson, G. N. Flerchinger, and L. D. McFadden (1996), Application of a soil-water balance model to evaluate the influence of Holocene climate change on calcic soils, Mojave Desert, California, USA, *Geoderma*, 74, 167-192.
- McFadden, L. D., S. G. Wells, and M. J. Jercinovich (1987), Influences of eolian and pedogenic processes on the origin and evolution of desert pavements, *Geology*, 15, 504-508.
- Meadows, D. G., M. H. Young, and E. V. McDonald (2006), Estimating the fine soil fraction of desert pavements using ground penetrating radar, *Vadose Zone J.*, 5, 720-730.
- Meek, D. W., and J. L. Hatfield (1994), Data quality checking for single station meteorological databases, *Agric. For. Meteorol.*, 69, 85-109.
- Mertens, J., R. Stenger, and G. F. Barkle (2006), Multiobjective inverse modeling for soil parameter estimation and model verification, *Vadose Zone J.*, 5, 917-933.
- Mertens, J., H. Madsen, M. Kristensen, D. Jacques, and J. Feyen (2005), Sensitivity of soil parameters in unsaturated zone modelling and the relation between effective, laboratory and in situ estimates, *Hydrol. Process.*, 19, 1611-1633.
- Mirus, B. B., K. S. Perkins, J. R. Nimmo, and K. Singha (2009), Hydrologic Characterization of Desert Soils with Varying Degrees of Pedogenesis: 2. Inverse Modeling for Effective Properties, *Vadose Zone J.*, 8, 496-509, 10.2136/vzj2008.0051.
- Mualem, Y. (1976), A new model for predicting the hydraulic conductivity of unsaturated porous media, *Water Resour. Res.*, 12, 513-522.
- Nielsen, D. R., J. W. Biggar, and K. T. Erh (1973), Spatial variability of field-measured soil-water properties, *Hilgardia*, 47, 215-260.
- Nimmo, J. R., K. S. Perkins, K. M. Schmidt, D. M. Miller, J. D. Stock, and K. Singha (2009), Hydrologic characterization of desert soils with varying degrees of pedogenesis: 1. Field experiments evaluating plant-relevant soil water behavior, *Vadose Zone J.*, 8, 480-495, 10.2136/vzj2008.0052.
- Noy-Meir, I. (1973), Desert ecosystems: Environment and producers, *Annu. Rev. Ecol. Syst.*, 4, 25-51.
- Ostler, W.K., and D.J. Hansen (2003), Diagnostic Tools and Reclamation Technologies for Mitigating Impacts of DoD/DOE Activities in Arid Areas. Final Report: SERDP Project No. CS-1131, 55 pp, U.S. Department of Energy.
- Parasuraman, K., A. Elshorbagy, and B. C. Si (2006), Estimating saturated hydraulic conductivity in spatially variable fields using neural network ensembles, *Soil Sci. Soc. Am. J.*, 70, 1851-1859.

- Perroux, K. M., and I. White (1988), Designs for disk permeameters, *Soil Sci. Soc. Am. J.*, 52, 1205-1215.
- Porporato, A., P. D'Odorico, F. Laio, L. Ridolfi, and I. Rodriguez-Iturbe (2002), Ecohydrology of water-controlled ecosystems, *Adv. Water Resour.*, 25, 1335-1348.
- Rawls, W. J., D. L. Brakensiek, and K. E. Saxton (1982), Estimation of soil water properties, *Trans. ASAE*, 25, 1316-1320.
- Rawls, W. J., D. L. Brakensiek, and M. R. Savabi (1989), Infiltration Parameters for Rangeland Soils, *J. Range Manage.*, 42, 139-142.
- Reece, C. F. (1996), Evaluation of a line heat dissipation sensor for measuring soil matric potential, *Soil Sci. Soc. Am. J.*, 60, 1022-1028.
- Rhoades, J. D. (1996), Salinity: electrical conductivity and total dissolved solids, in *Methods of Soil Analysis, Part 3: Chemical Methods*, edited by D. L. Sparks, pp. 417-435, Soil Science Society of America and American Society of Agronomy, Madison, WI.
- Rodriguez-Iturbe, I., A. Porporato, L. Ridolfi, V. Isham, and D. R. Cox (1999), Probabilistic modelling of water balance at a point: the role of climate, soil and vegetation, *Proc. R. Soc. London*, 455, 3789-3805.
- Saito, H., J. Simunek, and B. P. Mohanty (2006), Numerical analysis of coupled water, vapor, and heat transport in the vadose zone, *Vadose Zone J.*, 5, 784-800.
- Scanlon, B. R., and P. C. D. Milly (1994), Water and Heat Fluxes in Desert Soils .2. Numerical Simulations, *Water Resour. Res.*, 30, 721-733.
- Schaap, M. G., and W. Bouten (1996), Modeling water retention curves of sandy soils using neural networks, *Water Resour. Res.*, 32, 3033-3040.
- Schaap, M. G., and F. J. Leij (2000), Improved prediction of unsaturated hydraulic conductivity with the Mualem-van Genuchten model, *Soil Sci. Soc. Am. J.*, 64, 843-851.
- Schaap, M. G., F. J. Leij, and M. T. van Genuchten (2001), ROSETTA: a computer program for estimating soil hydraulic parameters with hierarchical pedotransfer functions, *J. Hydrol.*, 251, 163-176.
- Scott, R. L., W. J. Shuttleworth, T. O. Keefer, and A. W. Warrick (2000), Modeling multiyear observations of soil moisture recharge in the semiarid American Southwest, *Water Resour. Res.*, 36, 2233-2247.
- Simunek, J., R. Angulo-Jaramillo, M. G. Schaap, J. P. Vandervaere, and M. T. van Genuchten (1998), Using an inverse method to estimate the hydraulic properties of crusted soils from tension-disc infiltrometer data, *Geoderma*, 86, 61-81.
- Simunek, J., M. Sejna, H. Saito, M. Sakai, and M. T. Van Genuchten (2009), The HYDRUS-1D software package for simulating the one-dimensional movement of water, heat, and multiple solutes in variably-saturated media, user's manual, version 4.08, Department of Environmental Sciences, University of California, Riverside, Riverside, CA.
- Stevenson, B. A., E. V. McDonald, and T. G. Caldwell (2009), Root patterns for *Larrea tridentata* in relation to soil morphology in Mojave Desert soils of different ages, in *The Mojave Desert: Ecosystem*

- Processes and Sustainability*, edited by R. H. Webb, L. F. Fenstermaker, J. S. Heaton, D. L. Hughson, E. V. McDonald and D. M. Miller, pp. 312-338, University of Nevada Press, Reno, NV.
- Tietje, O., and M. Tapkenhinrichs (1993), Evaluation of pedo-transfer functions, *Soil Sci. Soc. Am. J.*, *57*, 1088-1095.
- van Genuchten, M. T. (1980), A Closed-Form Equation for Predicting the Hydraulic Conductivity of Unsaturated Soils, *Soil Sci. Soc. Am. J.*, *44*, 892-898.
- Van Genuchten, M. T., F. J. Leij, and M. Senja (1990), The RETC Code for Quantifying Functions of Unsaturated Soils, Version 1.0. *Rep. EPA Report 600/2-91/065*, 85 pp, U.S. Salinity Laboratory, USDA, ARS, Riverside, CA.
- Vogel, H. J., and K. Roth (2003), Moving through scales of flow and transport in soil, *J. Hydrol.*, *272*, 95-106.
- Vrugt, J. A., and B. A. Robinson (2007), Improved evolutionary optimization from genetically adaptive multimethod search, *Proc. Natl. Acad. Sci. USA*, *104*, 708-711, 10.1073/pnas.0610471104.
- Vrugt, J. A., B. A. Robinson, and J. M. Hyman (2009), Self-Adaptive Multimethod Search for Global Optimization in Real-Parameter Spaces, *IEEE Trans. Evol. Comp.*, *13*, 243-259, 10.1109/tevc.2008.924428.
- Vrugt, J. A., W. Bouten, H. V. Gupta, and J. W. Hopmans (2003), Toward Improved Identifiability of Soil Hydraulic Parameters: On the Selection of a Suitable Parametric Model, *Vadose Zone J.*, *2*, 98-113.
- Vrugt, J. A., P. H. Stauffer, T. Wöhling, B. A. Robinson, and V. V. Vesselinov (2008), Inverse modeling of subsurface flow and transport properties: A review with new developments, *Vadose Zone J.*, *7*, 843-864, 10.2136/vzj2007.0078.
- Wöhling, T., and J. A. Vrugt (2011), Multiresponse multilayer vadose zone model calibration using Markov chain Monte Carlo simulation and field water retention data, *Water Resour. Res.*, *47*, 10.1029/2010wr009265.
- Wöhling, T., J. A. Vrugt, and G. F. Barkle (2008), Comparison of three multiobjective optimization algorithms for inverse modeling of vadose zone hydraulic properties, *Soil Sci. Soc. Am. J.*, *72*, 305-319.
- Wosten, J. H. M., Y. A. Pachepsky, and W. J. Rawls (2001), Pedotransfer functions: bridging the gap between available basic soil data and missing soil hydraulic characteristics, *J. Hydrol.*, *251*, 123-150.
- Yin, J., M. H. Young, and Z. B. Yu (2008), Effects of paleoclimate and time-varying canopy structures on paleowater fluxes, *J. Geophys. Res - Atmos.*, *113*, D06103, doi:06110.01029/02007D009010.
- Young, M. H., T. G. Caldwell, D. G. Meadows, and L. F. Fenstermaker (2009), Variability of soil physical and hydraulic properties at the Mojave Global Change Facility, Nevada: Implications for water budget and evapotranspiration *J. Arid Environ.*, *73*, 733-744.
- Young, M. H., E. V. McDonald, T. G. Caldwell, S. G. Benner, and D. G. Meadows (2004), Hydraulic properties of a desert soil chronosequence in the Mojave Desert, USA, *Vadose Zone J.*, *3*, 956-963.

5 GLOBAL CONCLUSIONS AND RECOMMENDATIONS

The coevolution of soil development and biologic processes drive arid system hydrologic processes in both space and time. The three lines of research presented in this dissertation highlight the intricacies of desert soils, which at first may appear highly heterogeneous but without an underlying structure. We answered three fundamental questions regarding arid soil processes related to (1) soil variability at the sub-meter level, (2), bio-abiotic processes controlling this heterogeneity, and (3) numerical simulations and multiobjective parameter optimization techniques. Gradients in physical and hydraulic properties exist because of the fundamentally different processes beneath canopies and the associated mound, even though the relative age of the shrub can vary greatly.

We first used discrete measurements of fine-scale soil heterogeneity and dimensionless correlation to address the role of biotic processes affecting soil physical properties. Additionally, we determined the extent of positive biotic feedbacks in arid shrublands. We found that on young, weakly structured soils with high overall conductivity, this biofeedback may act to retain moisture and not simply increase saturated conductivity. These results confirmed that canopy and interspace microsites were statistically different and independent of vegetation type. The canopy $K(\psi)$ was significantly lower than interspace $K(\psi)$ by approximately two-fold. The differences became amplified as ψ decreased, resulting from the significantly larger α underneath vegetation. Results of this study indicate that spatial structure exists at the meter scale and is highly correlated and scalable to shrub size.

The dichotomy between canopy and interspace K_s is primarily a result of the abiotic processes that influence interspace pedogenesis. Desert landforms consist of heterogeneous alluvial deposits of interspersed soils of varying ages. For our second study, we used the chronosequence concept to assess how this relationship evolves temporally over Quaternary time scales. In this geomorphic context, we found a divergence between canopy and interspace microsites, requiring significant time to develop a restrictive Av horizon at interspace locations. Bioturbation works to reset the pedogenic clock underneath shrubs and disrupt the formation of desert pavement. For example, data from microsites on the youngest surface were similar for nearly all properties while the greatest dichotomy of properties between microsites was seen on the oldest Qf3 surface. For all geomorphic surfaces, we found significantly ($p < 0.001$) lower values of density, soil structure grade (Sg), particle size standard deviation (σ), and silt and clay content and higher ($p < 0.001$) sand, organic matter, log-transformed K_s and α underneath canopies. The resulting unsaturated conductivities converge at both microsites at modest tensions of -6 to -4 cm.

Spatially, we found a gradient in hydraulic and physical soil properties that extended 1.3 to 1.4 times the canopy radius. At proximal locations ($R_{norm} < 1.5$) on all geomorphic surfaces, density ($p < 0.01$), σ ($p < 0.001$), gravel ($p < 0.001$), and clay ($p < 0.05$) increase away from the shrub-center, while sand ($p < 0.001$), organic matter ($p < 0.01$) and α ($p < 0.05$) decrease. No significant distal correlations were observed. Hydraulic properties were weakly correlated in space but 75% of the variance could be attributed to sand content, soil structure grade, mean-particle diameter, and organic matter – none of which can be definitively biotic or abiotic. Within the geomorphic context presented

here, the positive biotic feedback is most pronounced on interspace surfaces where the hydraulic conductivity is lower and the soil more developed. We propose that the current positive biotic feedback hypothesis is not simply higher infiltration capacity underneath shrubs, but more hydraulically favorable.

The final study used advanced algorithms to determine the effective properties of the shallow vadose zone in arid lands. Three poorly developed, young alluvial soils were inversely modeled in HYDRUS using the AMALGAM algorithm to obtain effective vadose zone parameters in the central Mojave Desert. Observations of water content (θ) and absolute head (ψ) were used to formulate our multiobjective framework independently optimized both residuals. In addition, we compared results to direct and indirect parameterization methods using infiltrometers and pedotransfer functions. Although dynamic ranges of ψ were observed, θ remained near the dry end, limiting our ability to resolve parameters associated with the wet end of the moisture release curve. We found sensitivity of wet-end hydraulic parameters (K_s and θ_s) to be low in arid soil systems. Additionally, we found θ_r , n , and l to be sensitive to water content ($RMSE_\theta$) and n , α , and l to be sensitive to matric head ($RMSE_\psi$).

Pareto-analysis identified model structure inadequacies between fitting both criteria and also revealed significant variation between Pareto optimal solutions that bifurcated into populations that favored θ or ψ error minimization. Increasing vertical heterogeneity in the simulated soil profile improved model performance but at the expense of parameter identifyability at greater depths. Under the multiobjective framework, we found soil temperature to be virtually insensitive to any parameterization;

θ could be successfully simulated using a multitude of parameter combinations; however, ψ was underestimated (too moist) regardless. A region of parameter space exists that results in unrealistic parameter combinations that effectively produce a non-dominant Pareto solution, but which were outside the realm of physically based parameters. Although the Pareto-compromise effectively minimizes both θ and ψ , the resulting parameter sets differed more than would be expected from the coarse textures of the field soils. Direct and indirect methods of parameterization also matched observed θ (and soil temperature), but not ψ . The very dynamic range of ψ (1-400 m) was coupled to a relatively small range of θ that seldom exceeded $0.10 \text{ m}^3 \text{ m}^{-3}$, perhaps not providing sufficient data or information for robust inverse modeling procedures. Optimizations were also attempted using the more robust energy balance surface condition as well as vapor transport; however, this only resulted minimally more water lost (~5%), still failing to approach measured ψ in deeper soils. Ultimately we suspect a structural error in the model, which will be pursued for further research. Lastly, arid systems typically span a narrow range of θ , affecting our ability to resolve the wet-end hydraulic characteristics. Near-saturated measurements from infiltrometers were used directly, but the results were not very promising when applied to simulated ψ .

In summary, we presented two methods of characterizing soils that focused on the wet-end and dry-end of the soil water characteristic curve. The infiltrometers are confined to near-saturated pressures, while our *in situ* measurements seldom showed water contents greater than residual levels. Joining these two characterization methods requires further research. For example, the inversion of infiltrometer data provides a full

hydraulic characterization but the uncertainty beyond the wet-end measurement range makes us tentative to apply them across the full range of possible soil conditions – as shown by the forward modeling of infiltrometer data in Chapter 4.

The obvious next step in this research theme is to apply both the binary and gradient soil hydraulics (Chapters 2 and 3) to a field-scale numerical simulation with lessons-learned from Chapter 4. Field-scale vegetation patterns can be easily obtained from aerial imagery and the spatial distribution of hydraulic parameters for K_s can be derived for both binary and gradient based methods. A study like this would help to answer the question: to what extent does micro-scale variability affect larger-scale water balance? Additional water retention parameters would be needed, for instance, through numerical inversion of the infiltrometer data, and some spatial statistics to robustly scale the results.

All the above methods required a combination of field and numerical work. The unique coupling of soil moisture and matric potential to determine the Pareto compromise solution between these two independent measures resulted in a more balanced, physically valid parameter suite – if these parameters even have any physical meaning. As such, researchers must also find a compromise in their work – no modeler should exclude field work and vice versa. Simply obtaining the best fit without regard to physical meaning of the resultant parameters could be misleading.

Future research must address these limitations as soil physics and vadose zone hydrology leave the agricultural fields and enters more dynamic and challenging environments. As modeling and optimization techniques move forward, our validation data and its scaling have made little advancement. The model structural issues we found

cannot be resolved without better data and with greater informational content. The aperiodic nature of arid systems challenges our ability to resolve these issues, and without long-term monitoring, we may never have the luck needed to observe extreme moisture events that push our models to the wet end. Finally, without this informational content and with quasi-physically based models, our ability to move beyond our calibration range and forecast future or past climates will always be uncertain.